

## **UC Merced**

### **UC Merced Electronic Theses and Dissertations**

#### **Title**

Sensing Classical Motion with Quantum Mechanical Precision

#### **Permalink**

<https://escholarship.org/uc/item/1wr090d9>

#### **Author**

Casara, Joshua Giovanni Anthony

#### **Publication Date**

2018

Peer reviewed|Thesis/dissertation

UNIVERSITY OF CALIFORNIA, MERCED

**Sensing Classical Motion with Quantum Mechanical Precision**

A dissertation submitted in partial satisfaction  
of the requirements for the degree of  
Doctor of Philosophy

in

Physics

by

Joshua Giovanni Anthony Casara

Committee in Charge:

Professor Jay Sharping, Chair

Professor Michael Scheibner, Advisor

Professor Anne Kelley

2018

Copyright

Joshua G. A. Casara, 2018

All rights reserved

The dissertation of Joshua G. A. Casara, titled Sensing Classical Motion with Quantum Mechanical Precision, is approved, and it is acceptable in quality and form for publication on microfilm and electronically:

Chair	_____	Date _____
	Professor Jay Sharping	
	_____	Date _____
	Professor Michael Scheibner	
	_____	Date _____
	Professor Anne Kelley	

University of California, Merced

2018

# Table of Contents

<b>List of Abbreviations</b>	<b>vi</b>
<b>List of Tables</b>	<b>viii</b>
<b>List of Figures</b>	<b>ix</b>
<b>Acknowledgements</b>	<b>xvii</b>
<b>Curriculum Vitae</b>	<b>xviii</b>
<b>Abstract</b>	<b>xxv</b>
<b>1 Introduction</b>	<b>1</b>
<b>2 Theoretical Background</b>	<b>4</b>
2.1 The Schrödinger Equation . . . . .	4
2.2 Electronic Band Structure . . . . .	5
2.3 The Effective Mass Approximation . . . . .	7
2.4 Effect of Angular Momentum on the Band Structure . . . . .	8
2.5 Nature of Quantum Dots . . . . .	9
2.6 Photoluminescence . . . . .	15
2.7 Phonons and Polarons . . . . .	20
<b>3 Material System</b>	<b>29</b>
3.1 Self-Assembled InAs Quantum Dots . . . . .	29
3.2 Field-Effect Structures . . . . .	30
3.3 Patterned Structures . . . . .	33
<b>4 Experimental Techniques and Procedures</b>	<b>36</b>
4.1 Photoluminescence Spectroscopy . . . . .	38
4.2 Mechanically Inducing Static Strain in QDs . . . . .	42
4.3 Optically Inducing Dynamic Strain in QDs . . . . .	44
4.4 Fabry-Perot Interferometer and Resolution Enhancement . . . . .	47
4.5 Time-Correlated Single Photon Counting . . . . .	50

<b>5</b>	<b>High Resolution Phonon-Assisted Quasi-Resonance Fluorescence Spectroscopy</b>	<b>53</b>
5.1	Laser Resolved . . . . .	54
5.2	Temperature Resolved . . . . .	56
5.3	Bias Resolved . . . . .	57
<b>6</b>	<b>Statically Strained PL</b>	<b>58</b>
6.1	Sample Heterostructure . . . . .	58
6.2	Force Calibration . . . . .	59
6.3	Strain Measurements . . . . .	61
<b>7</b>	<b>Dynamically Strained PL</b>	<b>65</b>
7.1	Sample Heterostructure . . . . .	65
7.2	Displacement Calibration . . . . .	66
7.3	Single Phonon Coupling Strength . . . . .	69
7.4	Strain Measurements . . . . .	69
<b>8</b>	<b>Conclusion</b>	<b>75</b>
<b>A</b>	<b>Derivation of the Euler-Bernoulli Beam Theory</b>	<b>76</b>
<b>B</b>	<b>Derivation of Atomic Force Microscope Equations</b>	<b>87</b>
<b>C</b>	<b>Derivation of Spectrometer Equations</b>	<b>95</b>
<b>D</b>	<b>Derivation of Fabry-Perot Equations</b>	<b>101</b>
	<b>References</b>	<b>106</b>

# List of Abbreviations

- AES Anisotropic Exchange Splitting, page 54
- AFM Atomic Force Microscopy, page 42
- AOM Acousto-Optic Modulator, page 46
- APD Avalanche Photodiode, page 46
- CCD Charge Coupled Device, page 36
- CW Continuous Wave, page 38
- DBR Distributed Bragg Reflector, page 29
- EBD Electron Beam Deposition, page 44
- FP Fabry-Perot, page 47
- GaAs Gallium Arsenide, page 15
- Ge Germanium, page 15
- InAs Indium Arsenide, page 15
- LN Liquid Nitrogen, page 36
- LO Longitudinal Optical, page 28
- MBE Molecular Beam Epitaxy, page 29
- OBDM Optical Beam Deflection Method, page 62
- PhC Photonic Crystal, page 29
- PL Photoluminescence, page 2
- PLE Photoluminescence Excitation, page 41
- PSD Position Sensitive Detector, page 43
- QD Quantum Dot, page 1

QDM Quantum Dot Molecule, page 11  
SEM Scanning Electron Microscope, page 35  
SK Stranski-Krastanov, page 29  
SPAD Single Photon Avalanche Diode, page 48  
TCSPC Time Correlated Single Photon Counting, page 50  
Ti-Saph Titanium Sapphire, page 36



# List of Tables

2.1	Table of parameters used to calculate the Stark shifts for the direct neutral exciton $X^0$ and the indirect neutral exciton $iX^0$ . The values shown match observed values obtained from InAs QDs grown in a GaAs matrix and embedded in an n-I Schottky diode. . . . .	12
2.2	Table of parameters used to calculate band gap energies as a function of temperature for GaAs, Ge, and InAs [38, 39, 40]. . . . .	15

# List of Figures

2.1	Energy band structure and electron occupancy of different types of crystalline material at absolute zero temperature. For the different crystalline materials, the valence band, conduction band, and fundamental band gap are indicated. . . . .	6
2.2	Schematic representations of the band structure for gallium arsenide. The upper energy band (blue) is the conduction band, while the lower energy bands are the valence bands. The valence band itself is split into three bands: the heavy-hole band (orange), the light-hole band (green), and the split-off band (red). . . . .	7
2.3	Schematic representations of exciton formation in QDs. (a) This representation treats the valence band as an ensemble of electrons in the ground state and shows the absorption of a photon promotes an electron to the conduction band leaving behind a hole. (b) This representation treats the valence band as empty in the ground state and shows the absorption of a photon creating an electron-hole pair. . . . .	10
2.4	Schematic representation of exciton formation in QDMs. The QDMs crystal ground state $ CGS\rangle$ can absorb a photon and create one of two types of neutral excitons, a direct exciton $ X^0\rangle$ or an indirect exciton $ iX^0\rangle$ . . . . .	11
2.5	Energy as a function of applied electric field for the direct and indirect exciton. The indirect exciton has a steeper slope due to its larger electrical dipole moment. . . . .	13
2.6	Energy as a function of applied electric field for the bonding $X_-$ and antibonding $X_+$ modes of the new molecular basis of the neutral exciton. In particular, take note of the avoided crossing at the resonance of the two states. For this graph a tunnel coupling of $t = 2$ meV was used. . . . .	14
2.7	Bandgap energy as a function of temperature for GaAs, Ge, and InAs materials. Values from Table 2.2 were used to generate these plots. . . . .	15

2.8	Schematic diagram detailing the various transitions that occur during the PL process of a QD. Absorption of a photon (blue) of energy $\hbar\omega_0$ excites an electron from the valence band into the conduction band, leaving behind a hole. The electron and hole, together known as an exciton, undergo non-radiative relaxation through the emission of phonons (black), putting the charges into the lowest energy configuration. Emission of a photon (red) of energy $\hbar\omega_1 < \hbar\omega_0$ occurs when the electron returns to the valence band and recombines with the hole. For neutral excitons in InAs QDs grown in GaAs, typical radiative relaxation times are around 800ps [41]. . . . .	16
2.9	Simple schematic depicting the four different spin states of a neutral exciton in a QD and the total sum of $m_j$ for each state. . . . .	18
2.10	Diagram showing the parameters used to derive the normal phonon modes of a one-dimensional diatomic chain of atoms. . . . .	22
2.11	Phonon dispersion curve for a one-dimensional diatomic chain of atoms. The acoustic branch has a linear response to the wavevector at the long wavelength limit, while the optical branch is approximately dispersionless. . . . .	24
2.12	Optical and acoustic phonon modes represented by a linear chain of atoms in a diatomic compound. Although only the longitudinal modes are shown here, there are two transverse phonon modes for both the optical and acoustic phonons. . . . .	25
2.13	The presence of an electron (black) disturbs the nearby atoms causing positive atoms (blue) to shift towards, and negative atoms (red) to shift away from, the electron. The phonon cloud (black ring) and the electron make up the polaron. . . . .	28
3.1	Schematic of the SK self-assembled growth method of InAs QDs. (a) The process starts with the deposition of GaAs onto a substrate. (b) Due to strain, the subsequent deposition of InAs plateaus at a thickness of 1.7 monolayers, creating a wetting layer upon which InAs droplets form. (c) The additional deposition of GaAs encapsulates the QDs. The process for fabricating QDMs is to repeat this technique. The build up of lattice strain causes subsequent layers of InAs to preferentially pool into droplets above the initial seed layer of QDs. The process can be repeated a number of times to form multi-dot systems. (d) The schematic of the MBE machine shows how elemental metals contained in individual furnaces can be exposed to the growth chamber by mechanical valves. . . . .	30
3.2	(Top) Band edge diagram and (Bottom) electrical circuit of a pn junction based diode under the application of (a) reverse bias, (b) zero bias, and (c) forward bias conditions. . . . .	32
3.3	Sample layer structure diagram. The aluminum aperture mask provides a $1\ \mu\text{m}$ diameter window through which PL can be collected. This serves the purpose of reducing the amount of PL from nearby QDMs reaching the detector [55]. . . . .	33

3.4	Sample layer structure diagram. The sacrificial AlGaAs layer is etched away to form a 180 nm thin free floating surface. This becomes the template upon which further patterns, such as photonic crystal cavities, waveguides, tuning forks, and micro-bridges, will be etched. The QDs are in the intrinsic region of an n-i-n-i-p diode structure [13]. . . . .	33
3.5	Scanning electron microscope image of a photonic crystal cavity structure. The black circles at the corners are drain holes used to remove the sacrificial layer beneath the photonic crystal cavity pattern to create a suspended membrane that is used to couple mechanical motion to the QDs [13]. . . . .	34
3.6	Scanning electron microscope image of an optical waveguide with two adjacent PhC cavity structures. On the left and right side of the structure are optical input and output couplers, allowing for a higher efficiency coupling of light. The dark trenches at the top and bottom edge are used to remove the sacrificial layer beneath the photonic crystal cavity pattern to create a suspended membrane that is used to couple mechanical motion to the QDs [13]. . . . .	34
3.7	Schematic of a distributed Bragg reflector. This structure is used to enhance the coupling of light out of the QDs. The index of refraction of the materials are represented by $n_i$ and the thickness of the layers are represented by $d_i$ . For constructive interference, the layer thickness must be proportional to the wavelength of light according to $d_i = \lambda/4n_i$ . . . . .	35
3.8	Scanning electron microscope image of a tuning fork (top) and a bridge (bottom) mechanical resonator [13]. . . . .	35
4.1	Combined experimental setup for laser spectroscopy, atomic force microscopy for static strain measurements, and optically induced mechanical resonance measurements. The setup has the option of focusing the PL into stage 1, 2, or 3 via the addition of flip mounts on the wedge mirrors. The dashed box is also represented in Fig. 4.13 . . . . .	37
4.2	PL spectra of an InAs QDM at different excitation powers. . . . .	39
4.3	Electric field dispersed PL spectrum, also known as a bias map. Plotting the data in this way allows one to clearly discern the indirect transitions from the direct transitions. Patterns emerge from the data that are much more obvious to the eye than in the single spectrum case. The red dashed line indicates the bias at which the power series was taken in Fig. 4.2 . . . . .	40
4.4	Schematic depicting the processes of (a) non-resonant PL spectroscopy and (b) PLE spectroscopy, as discussed in the main text. . . . .	40
4.5	<b>(Top)</b> Electric field dispersed excited state absorption spectrum, also known as a PLE map, of the neutral exciton in an InAs QD. The PLE map shows the excited state absorption spectrum of the neutral exciton. <b>(Bottom)</b> Electric field dispersed PL spectrum of the neutral exciton. . . . .	41
4.6	16-pin dual in-line package chip carrier for QD samples. . . . .	42

4.7	( <b>Left</b> ) Closeup image of a QDM sample in a 16-pin chip header, attached to the nano-positioning stages, mounted inside of the cryostation, and situated underneath the AFM probe holder. ( <b>Right</b> ) Stack of three nano-positioning stages for translation in $x$ , $y$ , and $z$ dimensions. The gold ribbons connecting the top plate to the base plate provide thermal conductivity between the sample and the cold finger of the cryostation. . . . .	43
4.8	Microscopy image of the AFM probe situated just above the sample surface. The inset of the figure shows the tip of the AFM probe aligned with the center of a membrane. . . . .	44
4.9	SEM image of a micro tuning fork with superimposed beam spots. The drive laser (green) is focused onto the base of the tuning fork while the signal laser (red) is focused on one of the tines at the free end of the tuning fork. The white scale bar represents $2 \mu\text{m}$ . . . . .	45
4.10	Schematic of the AOM used to amplitude modulate the drive laser. . . . .	45
4.11	Mechanical resonance spectrum of a microcantilever. For the purposes of the following experiments, only the fundamental mode is used. . . . .	46
4.12	PL map showing the linewidth broadening of the QD emission at the mechanical resonance of the microcantilever. . . . .	47
4.13	Schematic of the Fabry-Perot laser locking technique. The purpose of this technique is to control the thermal drift of the FP over time so that high resolution PL spectra can be obtained with little-to-no drift noise. The dashed box is a section of the PL platform depicted in Fig. 4.1. . . . .	49
4.14	Comparison of the signals captured by a typical spectroscopy experiment (black) and a FP resolution enhanced spectroscopy experiment (red). . . . .	50
4.15	Measurement schematic for the TCSPC technique. A laser pulse generates an exciton in a QD which quickly recombines and emits a photon. The photon is tagged by the electronics in the TCSPC module. The detection rate should be 20 to 100 times less than the excitation rate and should therefore include cycles that contain no emitted photons. The situation of a zero decay cycle is depicted as the second laser pulse in the three pulse train. . . . .	51
4.16	Schematic showing eight excitation and emission cycles of a TCSPC experiment. The original waveform is plotted at the top and the individual cycles collect the random events of photon emission. At the bottom is the final histogram of recorded photon collection times relative to the laser pulse. . . . .	52
5.1	Resolution comparison of three different PL techniques [65]. . . . .	55
5.2	Bias map of the anisotropic exchange splitting collected by high resolution phonon-assisted quasi-resonance fluorescence spectroscopy [65]. . . . .	55

5.3	<p><b>(Top)</b> Bias map acquired by triple additive electric field dispersed PL spectroscopy under non-resonant excitation. Emission from the neutral exciton (<math>X^0</math>), indirect exciton (<math>iX^0</math>), and the positive trion (<math>X^{+1}</math>) are identified. The vertical red dashed line at <math>-1.75</math> V represents the bias applied to the sample for the phonon-assisted technique, and the horizontal red dashed line is the energy at which the laser was held constant. <b>(Bottom)</b> High resolution phonon-assisted quasi-resonance fluorescence spectroscopy at the -1 phonon satellite of the neutral exciton. The transition energy of the exciton was tuned through a fixed laser energy of 1301.9 meV (952.4 nm) by stepping the temperature. The -1 LO phonon satellites appear around 36 meV below the zero phonon lines [65]. . . . .</p>	56
5.4	<p><b>(a)</b> Maximum PL intensities of the ground state neutral exciton. The quasi-resonant laser excitation energy is shown as a horizontal red line. <b>(b)</b> The tail of the acoustic phonon resonance as the exciton is swept through the laser energy. The benefits of a triple spectrometer in subtractive mode can clearly be seen as some stray laser light is shown less than 1 meV above the phonon tails. <b>(c)</b> Averaged PL from <b>(b)</b> showing the high resolution of this technique. The e-h exchange splitting can clearly be seen and the lifetime-limited linewidths can be easily extracted from fits of the data [65]. . . . .</p>	57
6.1	<p>Layer structure diagram displaying the absence of the sacrificial <math>\text{Al}_{0.7}\text{Ga}_{0.3}\text{As}</math> layer underneath the resonators as well as the n-i-n-i-p diode layer that makes up the resonators. The red line is the QD layer. . . . .</p>	59
6.2	<p><b>(a)</b> Interference signal caused by the change in reflectivity of a laser beam due to the decreasing distance between the two surfaces. The black curve represents a fit to Eq. (6.1) and is used to extract the piezoelectric constant <math>C_{piezo}</math>. <b>(b)</b> OBDM performed on a solid section of the sample. This curve is fit to Eq. (6.4) and is used to convert the normalized QPD response to a displacement of the AFM probe. The data from this graph is used to calibrate Fig. 6.4(b). . . . .</p>	60
6.3	<p><b>(a)</b> Microscope image of the AFM probe situated above the membrane. The excitation laser is positioned to excite QDs near the center of the membrane. <b>(b)</b> Schematic representation of the instrument. A closed-cycle helium cryostat contains the sample on three nanopositioners. An AFM probe is mounted above the sample. The orange laser is used to perform PL on the QDs embedded in the membranes while the red laser is used to perform the OBDM for measuring displacements. <b>(c)</b> Schematic of the effect strain has on the PL of the neutral exciton. <b>(d)</b> Photograph of the OBDM apparatus. <b>(e)</b> Photograph of the entire PL platform situated above the cryostation. . . . .</p>	61

6.4	<p><b>(a)</b> Electric field dispersed PL spectra of QDs embedded in a 180 nm thin membrane under in-plane tensile strain. From left to right, the panels represent a QD in a thin membrane experiencing increasing amounts of transverse force as indicated by the values above each false color map. The solid green bar at the bottom of the leftmost panel represents a 0.25 V scale for the horizontal axis of each map. The red dashed vertical lines represent the bias at which the PL energies were recorded. <b>(b)</b> OBDM measurements of the AFM probe displacement (blue) and the associated membrane displacement (green). <b>(c)</b> Quadratic fit to the PL energy shift as a function of applied force. The inset shows the position of the AFM probe above the membrane. . . . .</p>	63
7.1	<p>Layer structure diagram displaying the absence of the sacrificial <math>\text{Al}_{0.7}\text{Ga}_{0.3}\text{As}</math> layer underneath the resonators as well as the n-i-n-i-p diode layer that makes up the resonators. The red line is the QD layer. . . . .</p>	66
7.2	<p><b>(a)</b> Schematic of the GaAs cantilever with multiple reflections of the signal laser from the different surfaces. <b>(b)</b> Fabry-Perot model of reflectivity at 941.3 nm as a function of the gap between the cantilever and the substrate. The black curve shows the reflectivity when using the index of refraction for GaAs and the red curve uses an effective index of refraction. <b>(c)</b> Experimental reflectivity data showing the detected signal amplitude as a function of time for a series of drive laser powers. <b>(d)</b> Fabry-Perot model of the reflectivity as a function of time for a series of gap oscillation amplitudes [26]. . . . .</p>	67
7.3	<p>Mechanical response amplitude as a function of drive laser wavelength for a microcantilever. Note the peak in the response curve on resonance with the wetting layer for the InAs QDs at <math>\lambda = 870</math> nm. . . . .</p>	68
7.4	<p><b>(a)</b> SEM image of a cantilever shown with the estimated position of the QD studied on the left accompanied by a colormap on the right displaying the axial strain at the QD layer calculated using a finite element method. The colorbar has a scale of <math>10^{-4}</math> fractional change in length. <b>(b)</b> Mechanical resonance spectrum of a tuning fork structure measured by a spectrum analyzer. <b>(c)</b> Closeup of the fundamental mode of a tuning fork structure. The red curve is a Lorentzian fit to the data and the fit parameters indicate a quality factor of <math>Q \sim 3000</math>. <b>(d)</b> PL emission of a QD in a tuning fork as the frequency of the drive laser is swept through the mechanical resonance [26]. . . . .</p>	70
7.5	<p><b>(a)</b> SEM image of a PhC membrane structure with a waveguide, two cavities, and output couplers patterned into the surface. For this pattern, the sacrificial layer was removed through drain lines. <b>(b)</b> SEM image of a PhC membrane containing a single cavity. For this pattern, the sacrificial layer was removed through drain holes. <b>(c)</b> Strain induced PL shift as a function of the position of QDs along a membrane. The images on the right show colormaps of the displacement of the first three modes [13]. . . . .</p>	71

7.6	( <b>Left</b> ) Simple energy diagram of the spin states of a negative trion $X^{-1}$ under a magnetic field and the possible transitions. ( <b>Right</b> ) High resolution PL spectrum of the negative trion under a magnetic field. The possible transitions have been labeled and correspond to those on the left [13]. . . . .	72
7.7	( <b>a</b> ) TCSPC measurement of the individual spin states of the negative trion under 6T magnetic field and as a function of the oscillation period of the fundamental mode of the mechanical resonator [13]. ( <b>b</b> ) Electron and hole spin splittings as a function of the oscillation period of the mechanical resonator [13]. The solid red line indicates a sinusoidal fit to the hole data. ( <b>c</b> ) Ratio of the change in hole Zeeman splitting to the change in optical transition energy as a function of the hole Zeeman splitting for 9 different QDs. Red circles indicate that only one set of lines could be measured, either inner or outer. For these cases, $\Delta E_e$ is assumed to be negligible to find $\Delta E_h$ . Open (closed) circles indicate the hole and optical transition shifts are out of phase (in phase). The average drive power varies from 20-40 $\mu\text{W}$ for different QDs, and the PL laser power is 5 $\mu\text{W}$ [26]. . . . .	74
A.1	Schematic of a simple beam in (a) unbent and (b) bent positions. The beam has length $L$ , width $w$ , and thickness $t$ . The bending moments $M$ cause the beam axis to make a circular arc with center $C$ . . . . .	76
A.2	Schematic of the (a) rigid-body translation and the (b,c) two rigid-body rotations of the axial displacement field. . . . .	77
A.3	Relationship between the slope of the beam and the cross-sectional rotation. . . . .	78
A.4	Schematic of an unbent beam of length $L$ with concentrated transverse load $F$ and coordinate system orientation indicated. The left end of the beam is clamped while the right end is free to move. . . . .	79
A.5	Shear load, $V_k(y)$ , and bending moment, $M_i(y)$ , diagram for an infinitesimal segment of the cantilevered beam. $F\delta(y - L)dy$ is a concentrated load treated as a distributed force. The delta function ensures that the load only takes effect at $y = L$ . . . . .	81
A.6	Schematic of the first four vibrational modes of a clamped cantilever. . . . .	85
B.1	Schematic of the beam deflection method. The distances shown are necessary to calculate the sensitivity of the measurement. . . . .	88
B.2	Calibration curve for the sensitivity $S_{sensor}$ of the position detector. ( <b>Inset</b> ) The boxed region of the main figure is blown up. In the non-contact regime an interference pattern is observed which is used to calibrate the piezoelectric constant of the nanopositioners. . . . .	90



B.3	(a) Schematic showing the optical path of the laser beam as it reflects off the two surfaces. The laser beam reflected from the cantilever is initially centered on the detector when the sample is far from contact. (b) As the sample approaches, the change in the path length difference $\sqrt{2}d$ causes a shift in the interference pattern at the detector. It is important to note that the oscillations in Fig. B.2 are a result of the shifting of this interference pattern as a function of $z_{sample}$ .	91
B.4	The voltage difference between local maxima of the interference pattern is proportional to the wavelength of light $\lambda$ and inversely proportional to the piezoelectric constant $C_{piezo} = (36 \pm 1) \text{ nm/V}$ .	92
B.5	With the horizontal axis now in units of distance, the position-sensitive detector can be calibrated to units of distance as well. This measurement is made against a sample with negligible elasticity, e.g. a silicon wafer, so that the position of the sample is equal to the position of the tip $z_{sample} = z_{tip}$ .	93
B.6	Fully calibrated setup showing a plot of $z_{tip}(z_{sample})$ .	94
C.1	Schematic showing the interference of parallel waves upon transmission through a diffraction grating.	95
C.2	Schematic of a blazed diffraction grating for use in a spectrometer system.	96
C.3	Geometry of a spectrometer system of focal length $f$ , incident angle $\alpha$ , diffracted angle $\beta_c$ of the center wavelength, inclusion angle $\gamma$ , and grating angle $\psi$ .	96
C.4	Geometry of the spectrometer system used to calculate the pixel location of the $n$ th diffracted beam.	97
C.5	Triple spectrometer in the subtractive configuration. Note that the first two stages are used as a high quality bandpass filter, with the dispersion canceling out before entering the third stage.	98
C.6	Triple spectrometer in the additive configuration. The dispersion of the spectrometer in this configuration is roughly reduced by a factor of three.	99
C.7	Schematic showing the width of the image of the entrance slit at the CCD camera. The image is for a spectrometer whose grating is equidistant from the entrance and exit ports.	100
D.1	A FP consists of a pair of highly reflective mirrors spaced micrometers to centimeters apart. The interference pattern shown on the screen is a result of the sum of multiple reflections off the pair of mirrors.	101
D.2	Transmission intensity of a FP as a function of phase. The different colors represent varying values of the coefficient of finesse due to mirrors of different reflectivities.	104

# Acknowledgements

I would like to thank my family for always supporting me and providing an environment in which I could grow. Thank you to my soul mate, and future wife, Brittany Lee Amelia Conn for her love and devotion. I could not have done this without the sacrifices you have made for me! Thank you to my advisor, Prof. Michael Scheibner, for all of the guidance and wisdom you have provided throughout the years. Thank you to my committee members, Prof. Jay Sharping and Prof. Anne Kelley, for your insight and for forcing me to think outside of the box. Thank you to my research collaborators at the Naval Research Laboratory (NRL), Dr. Sam Carter, Dr. Allan Bracker, Dr. Daniel Gammon, Dr. Brennan Pursley, and Dr. Joel Grim. My time spent at the NRL was very short, but provided me with an abundance of experience and great memories. I would like to thank Andrew Jacobs for being a great friend, lab partner, and confidant. I would like to thank my undergraduate advisor, Prof. Rose Zhang, for being a fantastic mentor and shaper of young minds. If it weren't for you, I would not have pursued a degree in Physics. I would like to thank my sixth grade teacher, Chip Flemmer, for noticing that I was bored with the mathematics of the sixth grade, and advancing me to the material for the seventh grade. I honestly trace back my love for mathematics to your class. Lastly, I would like to thank everybody at the University of California, Merced, that has been kind and supportive throughout the years, including my colleagues in the Quantum Matter Group, the faculty and staff in the School of Natural Science and the School of Engineering, and the Graduate Division staff.

Joshua Casara  
Merced CA  
(209) 996-9460  
jcasara@ucmerced.edu

---

## RESEARCH OBJECTIVE

- To further my knowledge and understanding of solid state physics through experimental research on quantum dots.

## EDUCATION

- PhD in Physics, University of California at Merced, Merced, CA. 2018
- B.S. in Physics, California State University Stanislaus, Turlock, CA. 2012
- B.S. in Chemistry, California State University Stanislaus, Turlock, CA. 2012

## RESEARCH EXPERIENCE

### Graduate Student Researcher

January 2014 – Present

Prof. Michael Scheibner, UC Merced

“Quantum Dot Molecules”

- Modern technology is founded on the intimate understanding of how to utilize and control electrons. Next to electrons, nature uses phonons, quantized vibrations of an elastic structure, to carry energy, momentum, and even information through materials. Phonons permeate the crystalline components of modern technology, yet, in terms of technological utilization, phonons are far from being on par with electrons. This research is aimed at understanding the interactions between phonons, photons, and the charge carriers in semiconductors (holes or electrons).

### Visiting Student Researcher

June 2016 – August 2016

Dr. Samuel Carter, Naval Research Laboratory

“Quantum Dot Molecules”

- Optical characterization of the properties of a quantum dot embedded in a micromechanical resonator. The system allows us to probe the coupling between the mechanical motion and the quantum mechanical state of the quantum dot.

### Graduate Student Researcher

June 2012 – December 2013

Prof. Eric Brown, UC Merced

“Turbulent Magnetic Dynamo”

- Albert Einstein once ranked the mystery of the origins of Earth's magnetic field as one of the top three unsolved problems in physics. The goal of this research is to make a bench top magnetic dynamo that has a wider range of accessible parameter space than current dynamo experiments. We propose to do this by using novel materials to independently control the magnetic permeability and the viscosity of the material to have a finer control over the experimental parameters.

**Research Assistant**

Spring 2009 – Spring 2012

Prof. Nhu Y Stessman, CSU Stanislaus  
“Synthesis of Suberedamine A”

- Assisted Prof. Stessman with the synthesis of the natural product Suberedamine A. This product is found in marine sponges and is known to help prevent cancer. This research has furthered my understanding of organic synthesis, chemical safety, and proper chemical hygiene. Various separation, purification, and identification techniques are used in the process of organic synthesis.

**Research Assistant**

Fall 2010 – Spring 2011

Prof. Lu Rose Zhang, CSU Stanislaus  
“BSCCO Superconductivity”

- This research entails growing, analyzing, and testing high temperature superconducting materials to better understand the science behind them. My team and I first tested the effects of doping BSCCO with lead, which was originally done to make the ceramic more malleable but proved to enhance the electric and magnetic properties of it as well. The goal of this research is to gain an understanding of how the concentration of lead affects the electrical properties of the superconductor.

**Research Assistant**

Fall 2008 – Fall 2009

Prof. Michael D. Drake, CSU Stanislaus  
“Conformational Analysis of 2,3-Butanediol”

- The aim of this research was to analyze the specific conformations that the molecule 2,3-butanediol would exhibit in different solvents. Using a Jeol 500 MHz NMR spectrometer we could acquire high-resolution  $^{13}\text{C}$  and  $^1\text{H}$  spectra that allowed us to model the molecule using the analysis software gNMR. With this program, we could generate values for the coupling constants which yield the conformational information of the molecule in each solvent. This basic research will help us understand the different factors that affect the folding of proteins.

**TEACHING EXPERIENCE****University of California, Merced****Teaching Assistant**

August 2012 – May 2017

- PHYS 08: Introductory Physics I for Physical Sciences and Engineering
- PHYS 18: Introductory Physics I for Biological Sciences
- PHYS 19: Introductory Physics II for Biological Sciences
- MATH 11: Calculus I
- MATH 12: Calculus II

## PUBLICATIONS

- *S. G. Carter, A. S. Bracker, G. W. Bryant, M. Kim, C. S. Kim, M. Zalalutdinov, M. K. Yakes, C. Czarnocki, **J. Casara**, M. Scheibner, and D. Gammon*, “Spin-mechanical coupling of an InAs quantum dot embedded in a mechanical resonator,” PRL, in review, (2018)
- *Kunlun Bai, **Joshua Casara**, Aparna Nair-Kannaganti, Aubrey Wahl, Florian Carle, and Eric Brown*, “Effective magnetic susceptibility of suspensions,” JAP, in review, (2018)
- *Liuyang Sun, Parveen Kumar, Junho Choi, Sebastian Roesch, Kha Tran, **Joshua Casara**, Eduardo Priego, Yu-Ming Chang, Galan Moody, Kevin Silverman, Virginia O. Lorenz, Michael Scheibner, and Xiaoqin Li*, “Transient Stokes Photon Interference Reveals Intrinsic Phonon Dephasing Dynamics in MoS<sub>2</sub>,” PRL, in review, (2017)
- *Samuel G. Carter, Allan S. Bracker, Mijin Kim, Chul Soo Kim, Maxim Zalalutdinov, Brennan C. Pursley, Sophia E. Economou, Cyprian Czarnocki, **Joshua Casara**, Michael Scheibner, and Dan Gammon*, “Quantum Sensing of Mechanical Motion with a Single InAs Quantum Dot,” GOMACTech 2017 Proceedings, in press (2017)
- *Andrew R. Jacobs, **Joshua Casara**, Cameron Jennings, Mark L. Kerfoot, Cyprian Czarnocki, Alexander O. Govorov, and Michael Scheibner*, “Phonon-induced slow light in a quantum dot molecule,” AIP Adv., in review, (2017)
- *Florian Carle, Kunlun Bai, **Joshua Casara**, Kyle Vanderlick, and Eric Brown*, “Development of Magnetic Liquid Metal Suspensions for Magnetohydrodynamics,” Phys. Rev. Fluids, in press (2017)
- *Cyprian Czarnocki, Mark L. Kerfoot, **Joshua Casara**, Andrew R. Jacobs, Cameron Jennings, and Michael Scheibner*, “High Resolution Phonon-Assisted Quasi-Resonance Fluorescence Spectroscopy,” J. Vis. Exp., in press (2016)

## CONFERENCES AND PRESENTATIONS

### American Physical Society March Meeting

March 5-9, 2018

Convention Center, Los Angeles, CA

#### Session B27: Optomechanics II

- *Carter, Samuel; Bracker, Allan; Yakes, Michael; Kin, Mijin; Kim, Chul Soo; Zalalutdinov, Maxim; Bryant, Garnett; Casara, Joshua; Czarnocki, Cyprian; Scheibner, Michael; Gammon, Dan; “Spin-mechanical coupling of an InAs quantum dot embedded in a mechanical resonator”*

#### Session S18: Quantum Dots and Nanocrystals: Structural and Optical Properties

- *Kumar, Parveen; Jennings, Cameron; Czarnocki, Cyprian; Casara, Joshua; Jacobs, Andrew; Bracker, Allan; Pursley, Brennan; Gammon, Daniel; Economou, Sophia; Carter, Samuel; Scheibner, Michael; “Linewidth Broadening of Coupled Quantum Dot Pairs”*
- *Jacobs, Andrew; Casara, Joshua; Jennings, Cameron; Kumar, Parveen; Scheibner, Michael; “Optophononic Polarization Rotation in Coupled Quantum Dots”*

### 2016 DTRA Basic Research Technical Review

July 18-22, 2016

Waterford at Springfield, Virginia

- *Casara, Joshua; Czarnocki, Cyprian; Jacobs, Andrew; Scheibner, Michael “Molecular Polaron Formation of Acoustic Phonons in QDMs”*

### 87<sup>th</sup> Annual Meeting of The Society of Rheology

October 11-15, 2015

Hyatt Regency Baltimore, Baltimore, Maryland

- *Carle, Florian; Bai, Kunlun; Casara, Joshua; Vanderlick, Kyle; Brown, Eric “Development of liquid metal suspensions with tunable viscosity and magnetic susceptibility for magnetohydrodynamics”*

### American Physical Society March Meeting

March 2-6, 2015

Henry B. Gonzalez Convention Center, San Antonio, TX

#### Focus Session D13: Optical Properties of Semiconductor Nanostructures

- *Casara, Joshua; Czarnocki, Cyprian; Gad, Youstina; Jacobs, Andrew; Jennings, Cameron; Kerfoot, Mark; Monteros, Alessandro; Peev, Thomas; Tin Yau Tse, Joshua; Scheibner, Michael; “Molecular Polaron Formation of Acoustic Phonons in Quantum Dot Molecules”*

## Focus Session L6: Phononic and Mechanical Phenomena in Nanostructures

- *Jacobs, Andrew; Casara, Joshua; Jennings, Cameron; Kerfoot, Mark; Scheibner, Michael*; “Slow Light Using Crystal Lattice Vibrations in Coupled Quantum Dots”

### **American Geophysical Union Meeting** San Francisco, CA

December 9-13, 2013

- *Casara, Joshua; Brown, Eric; Xu, Qin; Oudalov, Nikolai; Guo, Qiti; Jaeger, Heinrich M.*; “Novel Material Designed to Achieve Greater Tunability in Magnetic Dynamo Experiments”

### **25<sup>th</sup> Annual CSU Statewide Student Research Competition** CSU Fresno, Fresno, CA

May 6-7, 2011

- *Casara, Joshua; Lopez, Rodolfo Jr.; Franco, Gregorio Jr.; Lee, Steven; and Zhang, Lu Rose*; “The Effects of Lead Doping on  $(\text{BiPb})_2\text{Sr}_2\text{CaCu}_2\text{O}_8$  Superconductors.”

### **American Physical Society April Meeting** Hyatt Hotel, Anaheim, CA

April 30 – May 3, 2011

- *Casara, Joshua; Lopez, Rodolfo Jr.; Franco, Gregorio Jr.; Lee, Steven; and Zhang, Lu Rose*; “Investigation of Anisotropic Magnetic Properties in  $(\text{BiPb})_2\text{Sr}_2\text{CaCu}_2\text{O}_8$  Superconducting Crystals”

### **25<sup>th</sup> Annual CSU Stanislaus Student Research Competition** CSU Stanislaus, Turlock, CA

March 11, 2011

**Achieved the honor of second place.**

- *Casara, Joshua; Lopez, Rodolfo Jr.; Franco, Gregorio Jr.; Lee, Steven; and Zhang, Lu Rose*; “The Effects of Lead Doping on  $(\text{BiPb})_2\text{Sr}_2\text{CaCu}_2\text{O}_8$  Superconductors.”

## **VOLUNTEER EXPERIENCE AND CLUB AFFILIATIONS**

### **Member of the American Physical Society**

Spring 2011 - Present

### **President of the CSU Stanislaus chapter of the Society of Physics Students**

CSU Stanislaus

Fall 2011 – Spring 2012

- I chartered the Stanislaus chapter of SPS on campus as well as set up live physics demonstrations to recruit new members. I created multiple fundraising events to raise not only money, but also awareness of the club. The club participated in community events, such as visiting high schools, to put on physics demonstrations to promote scientific curiosity in the younger generation.

**Vice President of the American Chemical Society Student Affiliates Chapter**

CSU Stanislaus

Fall 2010 – Spring 2011

- I organized the monthly meetings and filled in for the president in their absence. The ACS club held fundraisers where we sold discounted chemistry goggles and ACS exam guides. We held exciting chemistry demonstrations at the college to encourage enthusiasm towards chemistry.

**Member of the Louis Stokes Alliance for Minority Participation Program**

CSU Stanislaus

Spring 2009 – Spring 2012

- The LSAMP Program helps under represented students in the science mathematics engineering and technology disciplines by providing funds for school related necessities like books, GRE fee's, and graduate school application costs.

**AWARDS AND HONORS**

**Presidents Dissertation Year Fellowship**

UC Merced, Merced, CA

AY 2017 – 2018

- Fellowship is awarded to qualified graduate students who show promise toward making good progress on research goals and toward their PhD. Grantee is awarded \$36,000 for annual tuition, travel, and salary.

**MACES Summer Graduate Student Research Fellowship Program**

UC Merced, Merced, CA

Summer 2017

- Fellowship is awarded to qualified graduate students who show promise toward making good progress on research goals and toward their PhD. Grantee is awarded \$8,500 for summer funding.

**Physics Summer 2014 Travel Award**

UC Merced, Merced, CA

Summer 2014

- Fellowship is awarded to qualified graduate students who show promise toward making good progress on research goals and toward their PhD. Grantee is awarded \$500 for summer funding towards travel costs.

**Graduate Student Summer Research Fellowship**

UC Merced, Merced, CA

Summer 2013

- Fellowship is awarded to qualified graduate students who show promise toward making good progress on research goals and toward their PhD. Grantee is awarded \$8,500 for summer funding towards research goals.

**Outstanding Student Achiever for the Physics (BS) Program**

Office of the Provost, CSU Stanislaus, Turlock, CA

Fall 2010 - Spring 2011

- Recipients represent the best and brightest among the CSU Stanislaus students, and each program selects only its most exceptional student for this award.



## CSU Stanislaus 25<sup>th</sup> Annual Student Research Competition

CSU Stanislaus, Turlock, CA

March 11, 2011

*Casara, Joshua; Lopez, Rodolfo Jr.; Franco, Gregorio Jr.; Lee, Steven; and Zhang, Lu Rose* “The Effects of Lead Doping on  $(\text{BiPb})_2\text{Sr}_2\text{CaCu}_2\text{O}_8$  Superconductors.”

- Our presentation won us the honor of second place at the CSU Stanislaus competition, which qualified us to continue to the CSU statewide competition at CSU Fresno.

## MENTORING

Applications in Modern Materials

Summer 2015

*Peter Meisenheimer*, University of Washington, Seattle, WA

- Introduced Peter to the optics lab and worked with him on fabricating an atomic force microscopy stage for our cryostation.
- Performed photoluminescence spectroscopy alongside Peter to better his understanding of experimental laboratory techniques.
- Peer reviewed both written documents and slide presentations on summer work.

*Bibhav Poudel*, Dougherty Valley High School, San Ramon, CA

- Discussed various topics in condensed matter physics specifically related to quantum dots, phonons, and optical spectroscopy.
- Introduced Bibhav to some of the laboratory equipment and demonstrated some of the laboratory techniques.
- Peer reviewed both written documents and slide presentations on summer work.

Tutoring Center

AY 2010 - 2012

CSU Stanislaus, Turlock, CA

- Facilitated tutoring sessions with individual students in physics, chemistry, biochemistry, and mathematics.
- Prepared material and guided exam workshops for large classrooms full of students studying for midterms in physics.

# Abstract

Sensing Classical Motion with Quantum Mechanical Precision

by

Joshua Giovanni Anthony Casara

Doctor of Philosophy in Physics

University of California, Merced

Professor Jay Sharping, Chair

The application of quantum mechanics provides the most precise measurements of physical phenomena ever devised. As an example, the atomic clock only loses one second of time per one hundred billion years. This is possible due to the extraordinarily long coherence times of the super cooled atoms involved in the measurement. It is this very precision that makes quantum mechanical techniques highly coveted in the field of metrology. The drawbacks to atomic clocks are their large size, expense, and lack of scalability. A more readily scalable architecture is required to mass produce sensors of this type; epitaxial semiconductor quantum dots provide such a scalable architecture. quantum dots are nanoscale semiconducting crystals that behave more like a single atom than like bulk material. Due to their atom-like nature, it becomes possible to controllably study quantum effects in a solid-state architecture, which allows for straightforward incorporation into conventional electronic devices. Quantum dots are a promising candidate for solid-state sensors due to their long charge and spin state coherence times. A recent study has shown that single particle charge and even spin states in quantum dots embedded in mechanical resonators couple to the mechanical motion of their local environment through strain. This realization allows for the measurement of classical motion via a quantum mechanical system. Until now, only spectral shifts have been quantified, leaving unknown the amplitudes of the mechanical motion inducing such shifts. In the Quantum Matter Group at UC Merced, we have developed a technique to quantify the strain-induced spectral shifts of the charge and spin states in quantum dots using nanoindentation atomic force microscopy in concert with photoluminescence spectroscopy. Our initial strain-shifted photoluminescence measurements indicate a spectral shift of 3 meV, readily resolved by standard spectroscopic techniques. Further experiments aim to quantify the displacement, force, and strain imposed on the quantum dots to obtain a better understanding of the system's sensitivity to such effects. In addition to the overall spectral shifts, other optical properties such as linewidth or fine structure can be monitored under the application of strain. The ability to spectrally shift charge and spin states in quantum dots using strain opens the door to novel techniques of sensing classical motion with quantum mechanical precision.

# Chapter 1

## Introduction

When the first quantum dots (QDs) were synthesized in the early 1990's, they were studied in large clusters or ensembles, yielding characteristic averages of the ensembles as a whole [1, 2]. Toward the end of the 1990's, advances in QD fabrication included incorporation into solid-state device structures; this led to optical studies of individual QD emitters [3, 4, 5]. These studies revealed that QDs have discrete fine structure similar to atomic spectra and can be made to behave like a resonantly driven two-level system [6, 7, 8]. The early part of the 21st century saw an increase in studies observing the effects of external fields (such as electric, magnetic and optical) on the properties of the QDs. For this reason, QDs have been coined "artificial atoms". Due to their atom-like properties and the advances made in semiconductor fabrication technologies, there has been a large push in applied research to make use of electronic and spin states in QDs as qubits and single-photon emitters in quantum information technologies [9, 10, 11]. The focus of this dissertation is to explore methods of coupling classical and quantum mechanical systems in ways that enable quantum-enhanced precision and resolution to the sensing of the classical motion [12].

In the past decade, single two-level emitters, such as QDs, have proven to be excellent quantum mechanical objects for coupling to classical systems [13, 14, 15, 16, 17]. As a result, QDs have been embedded in a number of different device structures to either enhance their properties or to utilize their properties for the purpose of sensing. Examples include embedding QDs in photonic crystal cavities [18], cantilever and bridge structures [13], nanometer-thin membranes [19, 20], distributed Bragg reflectors [21, 22], waveguides [23], and micropillars [22, 24, 25].

One of the major goals of this dissertation is to establish a set of tools for characterizing the effects these structures have on the properties of QDs. For example, QDs embedded in tuning fork or micro pillar structures can be driven at their mechanical resonance frequencies, causing the optical properties of the QD to oscillate in time. This enables direct control of the QD energy via driven mechanical motion. Taking this a step further, the quantum mechanical spin of the holes in these quantum dots can be manipulated via the mechanically induced motion in the tuning fork structure, opening the door for the use of QDs in spintronics [13, 26]. These interesting discoveries are made possible by experimental tools created in the lab.

The dissertation is setup in the following way:

Chapter 2 starts with the Schrödinger equation and how to use it to calculate the energy levels of the electronic band structure. The chapter continues with the effect of angular momentum on the valence band and the nature of QDs themselves. The excitation and emission of light through the photoluminescence (PL) effect is discussed before bringing attention to the effects of phonons and polarons on the optical properties of QDs. By the end of this chapter one should have a basic understanding of the fundamental physics governing the properties of QDs.

Chapter 3 begins with a description of the fabrication technique used to create self-assembled QDs and the field effect structures used to control their electronic properties. The chapter ends with a look at the different nanostructures patterned into the surface of the samples for the purpose of coupling the QDs to mechanical motion. This chapter will familiarize the reader with the materials being studied.

In chapter 4, experimental techniques are described, as are their purposes in probing various properties of the QDs. This chapter discusses the fundamentals of photoluminescence spectroscopy and how to utilize an AFM probe or an amplitude modulated laser to impart static or dynamic strain, respectively, on the mechanical structures within which the QDs are embedded. The end of the chapter describes the use of a Fabry-Perot cavity to increase the resolution of a photoluminescence experiment beyond that of the spectrometer. Lastly, the chapter touches upon the technique of time-correlated single photon counting, which can be used to gather information on the population dynamics of a system, as well as to synchronize PL measurements with mechanical modes of oscillation. After reading this chapter, one will be knowledgeable in the different experimental techniques used in this dissertation to probe the fundamental physics of semiconductor QDs.

In chapter 5, a technique for enhancing the resolution of a typical PL spectroscopy setup is described. The technique involves utilizing the effect of phonons on the QD charge states to perform resonant absorption measurements with an experimental apparatus that is typically used to measure emission. There are three different methods of performing the technique and each is described in its own section of the chapter. This chapter provides the reader with a step by step walkthrough on how to perform high resolution spectroscopy with a basic spectroscopic setup.

Chapter 6 describes the use of an atomic force microscope probe to impart static strain on QDs through nanoindentation of the encompassing mechanical resonators. A method for an in situ calibration procedure is described which utilizes the optical beam deflection method. Lastly, the chapter covers the main findings of the static strain measurements and how the quantitative results could be used to compare to other, less direct, methods of imparting strain. This chapter will impart upon the reader an understanding of the methodology used to apply mechanical force to a QD embedded in a thin membrane.

Chapter 7 discusses the experimental techniques used to modulate a mechanical resonator using an optically induced mechanical drive. A theoretical model for calculating the displacements caused by the optical driving is described. The chapter ends by discussing the use of the optical drive mechanism in dynamic strain measurements of the optical properties of QDs. This chapter will elucidate the methods and techniques used to optically induce mechanical strain on a QD embedded in a micromechanical resonator and the information gained from studying systems experiencing these effects.

Chapter 8 makes some concluding remarks and is followed by the appendix. The appendix contains derivations for the many mathematical models used throughout the dissertation, including derivations for the Euler-Bernoulli beam bending theory, atomic force microscope sensitivity and beam deflection method, the resolution of a spectrometer, and equations for the resolution enhancement afforded by a Fabry-Perot interferometer.

# Chapter 2

## Theoretical Background

This dissertation aims to detail the fundamental physics involved in the interactions between quantum mechanical systems and classical systems. To do so, QDs are embedded in numerous optical, electrical, mechanical structures, or a combination thereof. Embedding the QDs in these structures gives scientists the tools necessary to probe a quantum mechanical system at the single-particle level. Studying the interactions involved requires knowledge of condensed matter, semiconductors, optics, and structural mechanics. The following sections provide an overview of the underlying physics related to the interactions between a QD and its environment.

### 2.1 The Schrödinger Equation

In quantum mechanics, the time evolution of a system is given by the Schrödinger equation,

$$\hat{H}\Psi(\vec{r}, t) = i\hbar\frac{d}{dt}\Psi(\vec{r}, t), \quad (2.1)$$

where  $\hbar$  is the reduced Planck's constant,  $\hat{H}$  is the Hamiltonian operator and  $\Psi(\vec{r}, t)$  is the wavefunction, which contains all information about the system.

The Hamiltonian for a single particle of mass  $m$  with potential energy  $U(\vec{r}, t)$  is

$$\hat{H} = \frac{-\hbar^2}{2m}\nabla^2 + U(\vec{r}, t), \quad (2.2)$$

where  $\nabla^2$  is the Laplace operator. Combining equations (2.1) and (2.2) yields the time-dependent Schrödinger equation for a single particle,

$$\left[ \frac{-\hbar^2}{2m}\nabla^2 + U(\vec{r}, t) \right] \Psi(\vec{r}, t) = i\hbar\frac{d}{dt}\Psi(\vec{r}, t). \quad (2.3)$$

Equation (2.3) can be simplified further if we assume the potential  $U = U(\vec{r})$  is independent of time. This allows for the application of separation of variables. First, we let the wavefunction be a product of spatial and temporal functions  $\Psi(\vec{r}, t) = \psi(\vec{r})\phi(t)$ . Application of these assumptions yields:

$$\left[ \frac{-\hbar^2}{2m} \nabla^2 + U(\vec{r}) \right] \psi(\vec{r}) = E\psi(\vec{r}), \quad (2.4)$$

and

$$i\hbar \frac{d}{dt} \phi(t) = E\phi(t). \quad (2.5)$$

Equation (2.4) is the time-independent Schrödinger equation. With a known set of boundary conditions, the time-independent Schrödinger equation can be solved to yield the stationary eigenstates  $\psi(\vec{r})$  of the system and their corresponding energies  $E$ . Equation (2.5) can be easily solved to yield  $\phi(t) = e^{-iEt/\hbar}$ . This solution describes the time evolution of the stationary state  $\psi(\vec{r})$ .

## 2.2 Electronic Band Structure

While QDs are often called *artificial atoms*, this is somewhat of a misnomer. QDs are in fact nanoscale semiconductor crystals composed of hundreds or thousands of atoms; as a result, they exhibit many quantum behaviors that deviate from the case of a single atom. Atomic and molecular energy levels are typically discussed in the context of valence bond theory or molecular orbital theory; both theories make use of quantum mechanics to describe covalent bonding of atoms. For example, when two hydrogen atoms bond to form an  $H_2$  molecule, the wavefunctions of the electrons in the individual hydrogen atoms begin to overlap and can either be symmetric or antisymmetric. Consequently, the hydrogen molecule forms two molecular orbitals, the bonding (symmetric) and anti-bonding (antisymmetric) orbitals. The bonding orbital is lower in energy due to the symmetry of the overlapping wavefunctions corresponding to an increase in the probability of the electron residing between the hydrogen nuclei, while the anti-bonding orbital is higher in energy due to an antisymmetric overlapping of wavefunctions lowering the probability of the electron residing between the two hydrogen nuclei.

In a semiconductor crystal, a large ensemble of atoms coalesces into one very large molecule. For a crystal composed of  $N$  atoms, each atomic orbital must split into  $N$  molecular orbitals of distinct energies. Because matter at the macroscopic scale contains approximately  $10^{23}$  atoms, the number of available energy levels becomes enormous, and can be treated as a continuum of states. A continuum of energy states is usually referred to as a band, and a band gap is an energy range that is inaccessible to the electrons making up the crystal.

Calculating the energies of these bands would require solving the Schrödinger equation for every atom in the crystal, which would be unfeasible even with modern computational power. Instead, an assumption known as the *independent particle approximation* simplifies the problem by only considering the electrons in the outermost, valence shell of the atoms. Because of this, the inner shell electrons and the nuclei of the atoms are treated as stationary ions situated at the lattice sites of the crystal structure. The valence shell electrons are then treated as if they are trapped within the electrostatic potential of the nearest

lattice ion. If you consider the interaction of a single valence electron with the crystal, the Coulomb potential becomes a periodic function of the electrons distance to the nearest lattice ion  $U = U(\vec{r})$ , turning an  $N$ -body problem into  $N$  one-body problems. Because of the periodicity of the lattice, once an electron moves outside of the potential of one ion, it experiences the influence of the next. To calculate the stationary energy eigenvalues and eigenstates of a valence shell electron in a crystal, we must solve the time-independent Schrödinger equation for an independent particle in the vicinity of the periodic potential  $U(\vec{r} + a) = U(\vec{r})$ , where  $a$  is the lattice constant. For an electron of mass  $m_e$  the equation we must solve becomes:

$$\left[ \frac{-\hbar^2}{2m_e} \nabla^2 + U(\vec{r}) \right] \psi(\vec{r}) = E\psi(\vec{r}). \quad (2.6)$$

The solution to this equation yields the well known Bloch wavefunctions,

$$\psi_{n,\vec{k}}(\vec{r}) = e^{i\vec{k}\cdot\vec{r}} u_{n,\vec{k}}(\vec{r}), \quad (2.7)$$

and energies

$$E_{n,\vec{k}} = E_n(\vec{k}), \quad (2.8)$$

where  $\vec{r}$  is the position of the electron and  $\vec{k}$  is the wavevector. The Bloch wavefunction is the product of a plane wave with a periodic function. The exponential term is known as the envelope of the wavefunction and is a slowly oscillating sinusoid that modulates the rapidly varying part,  $u_{n,\vec{k}}(\vec{r})$ , which describes the behavior of the wavefunction near the atomic cores of the crystal lattice. The electron energy  $E_n(\vec{k})$  as a function of the wavevector  $\vec{k}$  defines the dispersion relation.

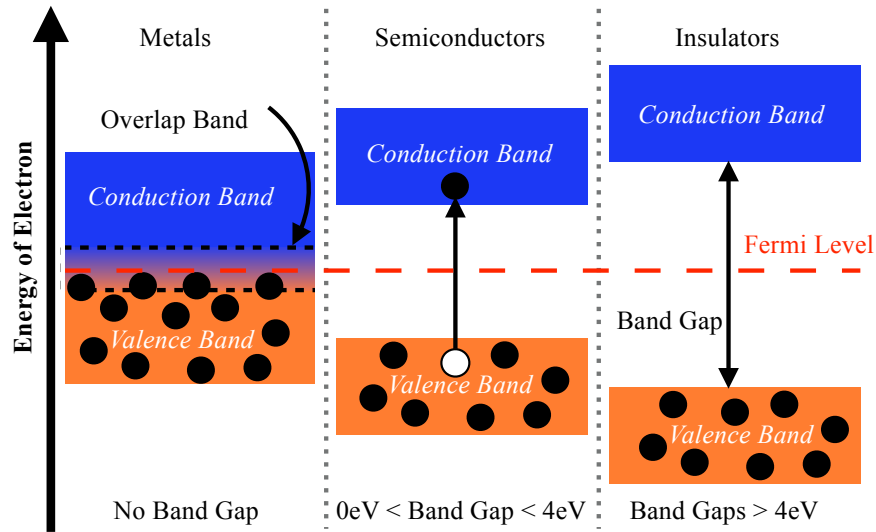


Figure 2.1: Energy band structure and electron occupancy of different types of crystalline material at absolute zero temperature. For the different crystalline materials, the valence band, conduction band, and fundamental band gap are indicated.



Some common examples of band gap energies are that of the semiconductors silicon and gallium arsenide, respectively, at 1.11eV and 1.43eV near room temperature ( $\sim 300\text{K}$ ), while diamond, a known insulator, has a band gap of 5.4eV near absolute zero ( $\sim 0\text{K}$ ) [27]. Figure 2.1 shows the electron occupancy of the valence and conduction bands at absolute zero for a metal, semiconductor, and insulator, as well as the band gap for semiconductors and insulators.

## 2.3 The Effective Mass Approximation

A common problem of interest for semiconductor physics is an electron provided enough energy to span the bandgap and enter the conduction band. The dispersion relation, Eq.

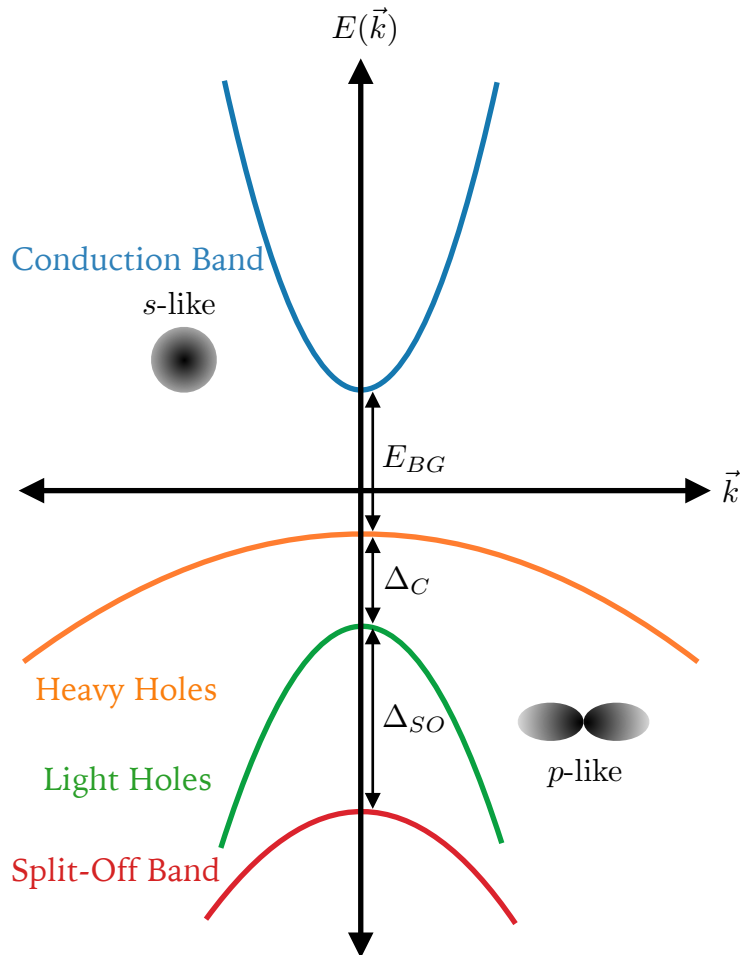


Figure 2.2: Schematic representations of the band structure for gallium arsenide. The upper energy band (blue) is the conduction band, while the lower energy bands are the valence bands. The valence band itself is split into three bands: the heavy-hole band (orange), the light-hole band (green), and the split-off band (red).

(2.8), describes the energy of an electron as it moves through an energy band. Near the conduction band minimum, the dispersion relation is approximately parabolic and the energy of the electron can be modeled as a free electron, whose energy is

$$E_{free}(\vec{k}) = \frac{\hbar^2}{2m_e} \vec{k}^2. \quad (2.9)$$

The curvature of this parabola, according to Eq. (2.9), can be expressed as an inverse mass  $1/m_e$ . However, an electron at the energy minimum of the conduction band has a different curvature than a free electron. As such, the effective mass approximation treats the behavior of the electron near the energy minimum of the conduction band in a crystal as a free electron with an effective mass whose dispersion relation can be written as:

$$E_c(\vec{k}) = \frac{\hbar^2}{2m_{e,eff}} \vec{k}^2. \quad (2.10)$$

The effective mass of an electron in a semiconducting crystal can differ greatly from that of the free-electron. For example, in GaAs and InAs the effective mass of the electron in the conduction band is  $0.067m_e$  and  $0.023m_e$ , respectively [28]. The effective mass is an important simplification for semiconductor physics because it is generally considered to be valid due to conduction band electrons preferentially occupying energy states near the conduction band minimum, also known as the *conduction band-edge*.

When an electron is excited from the valence band into the conduction band it leaves behind a hole. Similar to the conduction band electron, a hole near the energy maximum of the valence band, called the *valence band-edge*, is approximately parabolic. A missing electron in a sea of electrons carries a positive charge, and therefore a missing electron in the valence band can be thought of as a positive hole. It carries the same magnitude of charge as the electron, but it travels in the opposite direction in an electric field. Using the effective mass approximation, the energy of a hole at the valence band-edge of a direct bandgap semiconductor, such as GaAs and InAs, can be written as

$$E_v(\vec{k}) = -\frac{\hbar^2}{2m_{h,eff}} \vec{k}^2. \quad (2.11)$$

Equation (2.11) is similar to Eq. (2.10) except that it carries a negative sign and contains the effective mass for a hole. A hole is at its energy minimum when it is at the valence band maximum,  $\vec{k} = 0$ , and its energy gets larger as one moves downward along the valence band. The effective mass of a heavy hole in the valence band is significantly larger than an electron in the conduction band. For example, the heavy hole effective masses for GaAs and InAs are  $0.62m_e$  and  $0.60m_e$  respectively [28]. Figure 2.2 displays the dispersion relation for GaAs near  $\vec{k} = 0$

## 2.4 Effect of Angular Momentum on the Band Structure

The energy levels of a crystal arise from the linear combination of atomic orbitals, much like the molecular energy levels of a hydrogen molecule arise from the linear combination of the two constituent hydrogen atoms. For a hydrogen molecule, there are only two

atoms whose energy levels are combined resulting in a discrete energy level spectrum. For a bulk crystal, there are significantly more atoms involved such that the combination of the individual atomic orbitals results in a continuum of states yielding the energy bands. According to Kreibig et al., the crystal energy levels retain the same symmetries as their atomic constituents [29]. For semiconductors with a cubic crystal lattice, such as the zincblende structures of GaAs and InAs, the  $\vec{k} = 0$  states of the conduction band exhibit  $s$ -like orbitals. This leads to an angular momentum quantum number of  $l = 0$ . Correspondingly, the energy states of the valence band exhibit  $p$ -like orbitals, where the angular momentum quantum number is  $l = 1$ .

In atomic physics, the magnetic quantum number can take on a range of integer values equal to  $m_l = [-l, l]$ , including zero. For states exhibiting a  $p$ -like orbital shape, this results in magnetic quantum numbers of  $m_l = (-1, 0, +1)$ , which is triply degenerate when no magnetic field is present. Also similar to atomic physics, the spin-orbit interaction couples the intrinsic angular momentum (spin) of a quantum particle to its orbital angular momentum. This coupling creates a new quantum number, the total angular momentum quantum number  $j$ , which takes on the range of values in the range of  $|l - s| \leq j \leq |l + s|$ . As a consequence,  $\vec{S}$  and  $\vec{L}$  are no longer conserved properties on their own, only the total angular momentum  $\vec{J} = \vec{L} + \vec{S}$  is conserved.

Due to the spherical symmetry of the  $s$ -like orbital, there is no orbital angular momentum, and the spin-orbit interaction has no effect on the conduction band states  $j = s = 1/2$ , which remains doubly degenerate. The  $p$ -like orbitals, however, result in a spin-orbit interaction that splits the valence band into two states with total angular momenta of  $j = 3/2$ , which is quadruply degenerate, and  $j = 1/2$  which is doubly degenerate. At the  $\vec{k} = 0$  valence band-edge the spin-orbit interaction reduces the energy of the doubly degenerate state by the so-called *split-off energy* equal to  $\Delta_{SO}$ . For InAs, the split-off energy at cryogenic temperatures  $T < 4K$  is equal to  $\Delta_{SO} = 380meV$ , which is close in magnitude to the bandgap energy itself  $E_{BG} = 410meV$  [30, 31].

The remaining, quadruply degenerate, valence band states correspond to what are called the heavy-hole and light-hole bands. As the wavevector ventures away from zero the  $m_j = \pm 3/2$  and the  $m_j = \pm 1/2$  states begin to separate. The state that has the larger curvature is coined the *light hole* band and the state that has the smaller curvature is coined the *heavy hole* band. In QD systems, the dots are grown under strain and also exhibit confinement potentials due to their size. This breaks the degeneracy of the heavy and light hole bands by an amount  $\Delta_C$  [32]. The contents of this discussion are summarized in Fig. 2.2 [32, 33, 34].

## 2.5 Nature of Quantum Dots

QDs have acquired the nickname of “artificial atoms” due to their atom-like energy spectra. The smaller bandgap of the material comprising the QD relative to that of the surrounding material creates a potential well for nearby charges. Since the dots are nanometers long in all three dimensions, the number of available states for a trapped charge is very small resulting in a discretized energy spectrum. To understand the properties of QDs, some fundamentals

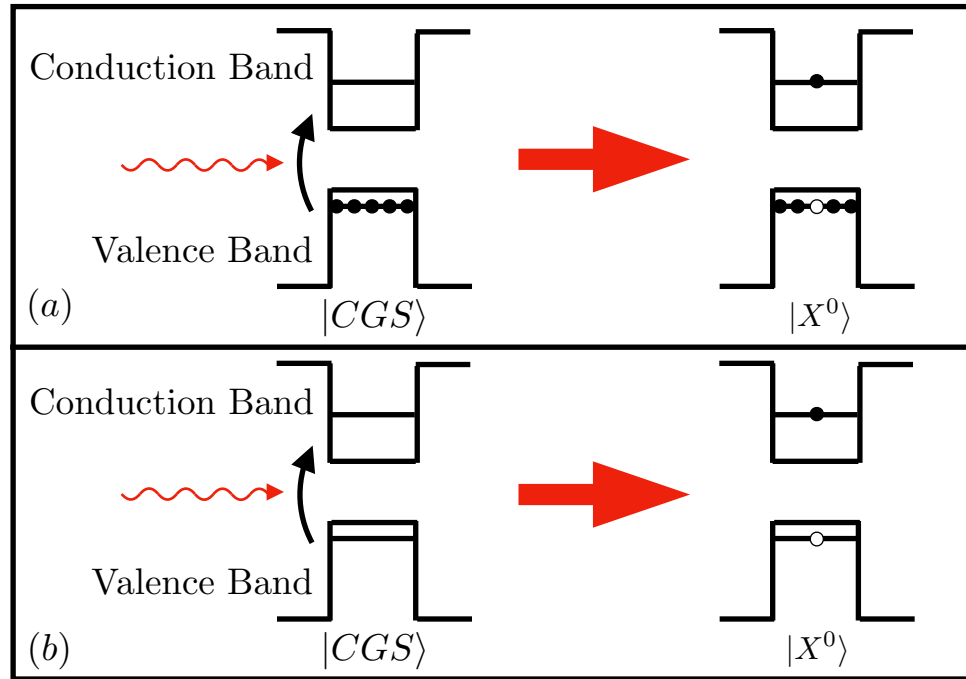


Figure 2.3: Schematic representations of exciton formation in QDs. (a) This representation treats the valence band as an ensemble of electrons in the ground state and shows the absorption of a photon promoting an electron to the conduction band leaving behind a hole. (b) This representation treats the valence band as empty in the ground state and shows the absorption of a photon creating an electron-hole pair.

of low dimensional solid-state physics must first be described.

### Exciton Formation

When a QD system is cooled to near absolute zero temperatures, it is in the so-called crystal ground state where all of the electrons reside at the valence band edge. If the constituent atoms of the QD absorb a photon of sufficient energy, then one of the valence band electrons is promoted to the conduction band. The excitation of this electron leaves behind a vacancy, or a hole, in the valence band. A commonly used mathematical abstraction that simplifies the conceptualization of this system is to imagine the hole as a particle with a positive charge (see Fig. 2.3). This removes the burden of considering the valence band as an ensemble of electrons with one missing, and also allows for the crystal ground state to be thought of as a state completely void of charges. Due to the quantum well-like nature of the QD, the charges are trapped in space. This is how excitons are formed in QDs. In a bulk semiconductor, the exciton is said to be hydrogenic, meaning that it is similar in form to a hydrogen atom, where the positive hole acts like the proton of the hydrogen atom and the electron experiences Coulombic attraction toward the hole. However, the binding energy between an electron and a hole in a bulk semiconductor is much smaller than that of a proton and an electron in hydrogen due to the screening effect of nearby electrons, known as the

dielectric potential, and also due to the smaller effective masses of the constituent particles. The particle size of an exciton is also much larger than that of a hydrogen atom and can be used as the criteria for determining whether or not a crystal is small enough to be classified as a QD. If the Bohr radius of the electron-hole pair is the same size, or larger than, the crystal in which it exists, then one has a QD.

A QD can absorb more than a single photon and may contain multiple excitons at one time. There exist charge states known as trions and biexcitons. A trion is an electronic state in a QD consisting of three charges. The positive trion is an exciton with an extra hole, and the negative trion is an exciton with an extra electron. A biexciton is an electronic state consisting of two holes in the valence band and two electrons in the conduction band, or more concisely two excitons.

### Quantum Dot Molecules

Quantum dot molecules (QDMs) are formed when two or more QDs are grown in close enough proximity for their wavefunctions to overlap, creating symmetric and anti-symmetric states analogous to natural molecules. For the purposes of this dissertation, only binary QDMs will be considered. Figure 2.4 shows a schematic of the neutral exciton formation in QDMs.

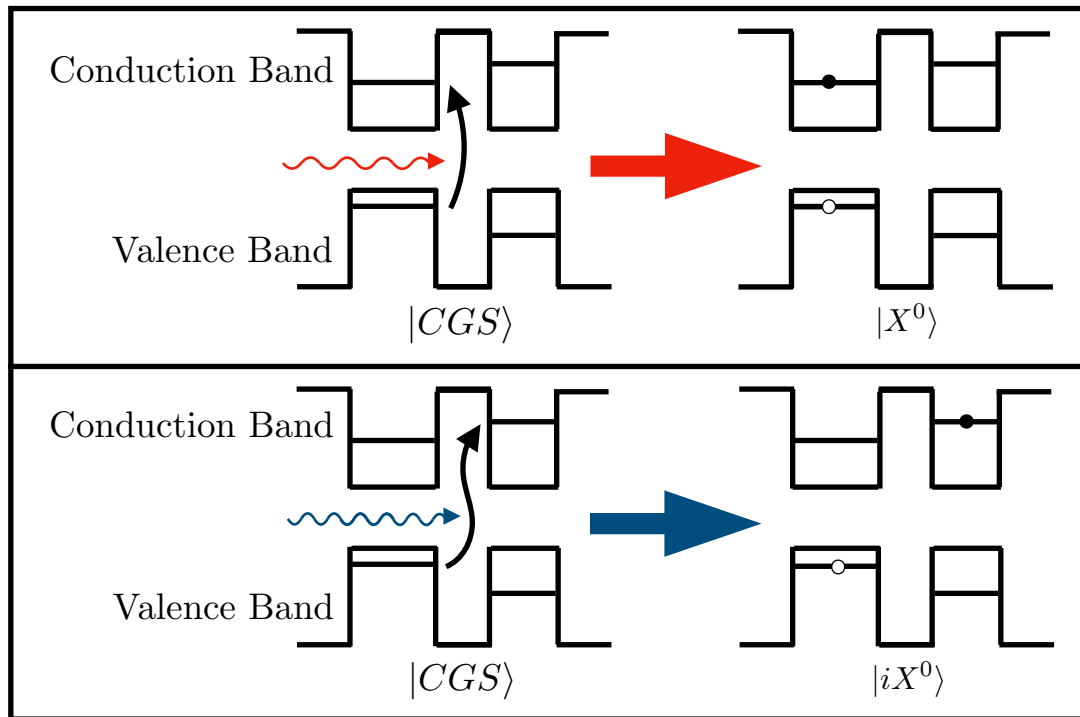


Figure 2.4: Schematic representation of exciton formation in QDMs. The QDMs crystal ground state  $|CGS\rangle$  can absorb a photon and create one of two types of neutral excitons, a direct exciton  $|X^0\rangle$  or an indirect exciton  $|iX^0\rangle$ .

### Stark Shifts in Quantum Dot Molecules

The valence and conduction band energy levels of a QDM can be manipulated via application of an electric field. The bending of the electronic band structure shifts the energy levels of the two dots relative to one another. This shift has a larger effect on the indirect excitons than on the direct excitons. This can be explained by considering the dipole moments of the charge states:

$$p_{State}(F) = qd(F) = q(d_{State,0} + \beta F). \quad (2.12)$$

Here,  $q$  is the charge of the dipole,  $d_{State,0}$  is the separation between charges at zero field for that state, and the product of the polarizability  $\beta$  and the electric field  $F$  is the field induced separation. The polarizability is proportional to the height of the individual dots [35], and due to the QDMs in this study consisting of dots of roughly equal heights, the polarizability for direct and indirect excitons is roughly equivalent. Therefore, only the separation between charges should differ between the two configurations. The direct exciton sees the electron and hole confined to the same QD, and due to the anisotropic shape of the QD there exists a small distance between charges and a correspondingly small dipole moment [36]. The indirect exciton, however, sees the electron and hole in separate QDs, yielding a relatively large dipole moment. The larger dipole moment of the indirect exciton is more strongly influenced by the electric field produced within the field-effect structure, and thus experiences a larger energy shift with applied bias. For this reason, charge states that are isolated to a single QD exhibit a quadratic response to electric field, while charge states that are spread across a QDM exhibit a linear response to the electric field. Fig. 2.5 shows a simplified plot of energy as a function of applied electric field for the direct and indirect states of a neutral exciton. The quadratic shift of the direct exciton is a result of the magnitude of the induced dipole moment surpassing that of the inherent dipole moment.

This graph was created by considering the direct and indirect excitons as independent energy states of the QDM system. The energies of the two states were calculated by assigning individual zero field energies  $E_{State,0}$  and dipole moments  $p_{State}$  to the following equation:

$$E_{State}(F) = E_{State,0} + p_{State}(F)F = E_{State,0} + qd_{State,0}F + q\beta F^2. \quad (2.13)$$

In this equation  $F$  is the electric field, and  $E_{State}(F)$  is the energy of the state as a function of the electric field  $F$ . The experimental values used to generate this plot are provided in Table 2.1. In all cases a charge of  $q = -e$  was used, where  $e = 1.6 \times 10^{-19}$  C is the elementary charge of an electron.

	$E_{State,0}$ (meV)	$d_{State,0}$ (nm)	$\beta$ ( $\frac{nm}{kV/cm}$ )
$X^0$	1300	0.5	0.01
$iX^0$	1310	5.0	0.01

Table 2.1: Table of parameters used to calculate the Stark shifts for the direct neutral exciton  $X^0$  and the indirect neutral exciton  $iX^0$ . The values shown match observed values obtained from InAs QDs grown in a GaAs matrix and embedded in an n-I Schottky diode.

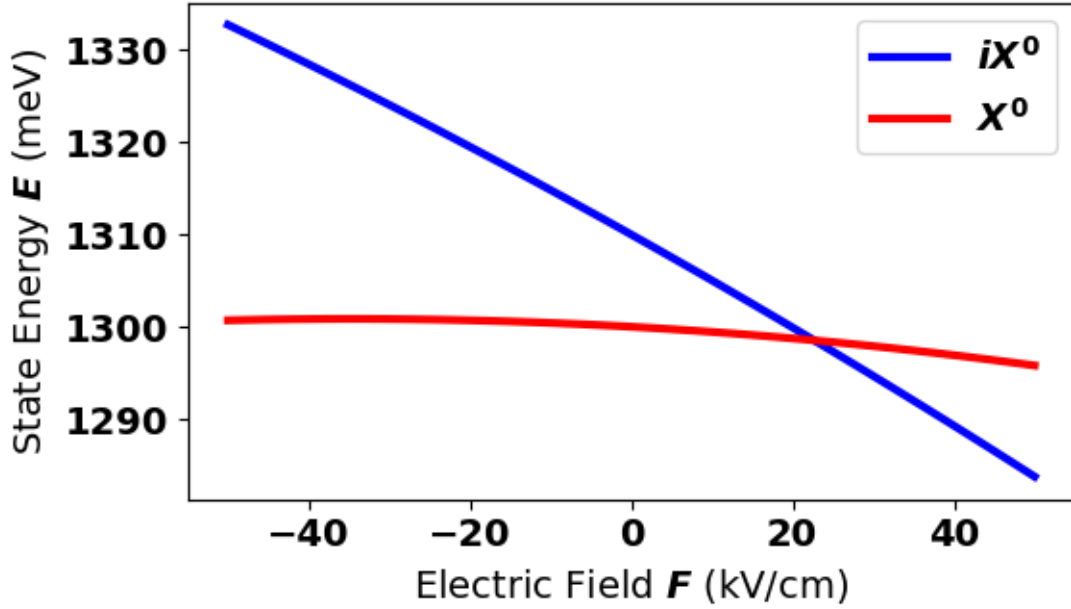


Figure 2.5: Energy as a function of applied electric field for the direct and indirect exciton. The indirect exciton has a steeper slope due to its larger electrical dipole moment.

### Tunneling in Quantum Dot Molecules

When the QDs making up a QDM are close enough for their wavefunctions to overlap, the independent energy states begin to mix, yielding symmetric and anti-symmetric states similar to those found in natural molecules. Mathematically, this mixing of states can be derived by treating the QDM as a two-level system. The Hamiltonian for such a configuration is then

$$\hat{H} = \begin{bmatrix} E_{X^0}(F) & t \\ t & E_{iX^0}(F) \end{bmatrix}. \quad (2.14)$$

The independent basis states of the direct and indirect exciton are

$$|X^0\rangle = \begin{bmatrix} 1 \\ 0 \end{bmatrix}, \text{ and } |iX^0\rangle = \begin{bmatrix} 0 \\ 1 \end{bmatrix}. \quad (2.15)$$

Diagonalizing the Hamiltonian reveals a set of eigenstates resembling a molecular basis consisting of bonding and anti-bonding modes:

$$\hat{H} = \begin{bmatrix} E_-(F) & 0 \\ 0 & E_+(F) \end{bmatrix}. \quad (2.16)$$

The new molecular eigenenergies are defined as,

$$E_{\pm}(F) = \frac{1}{2} \left[ (E_{X^0}(F) + E_{iX^0}(F)) \pm \sqrt{(E_{X^0}(F) - E_{iX^0}(F))^2 + (2t)^2} \right]. \quad (2.17)$$

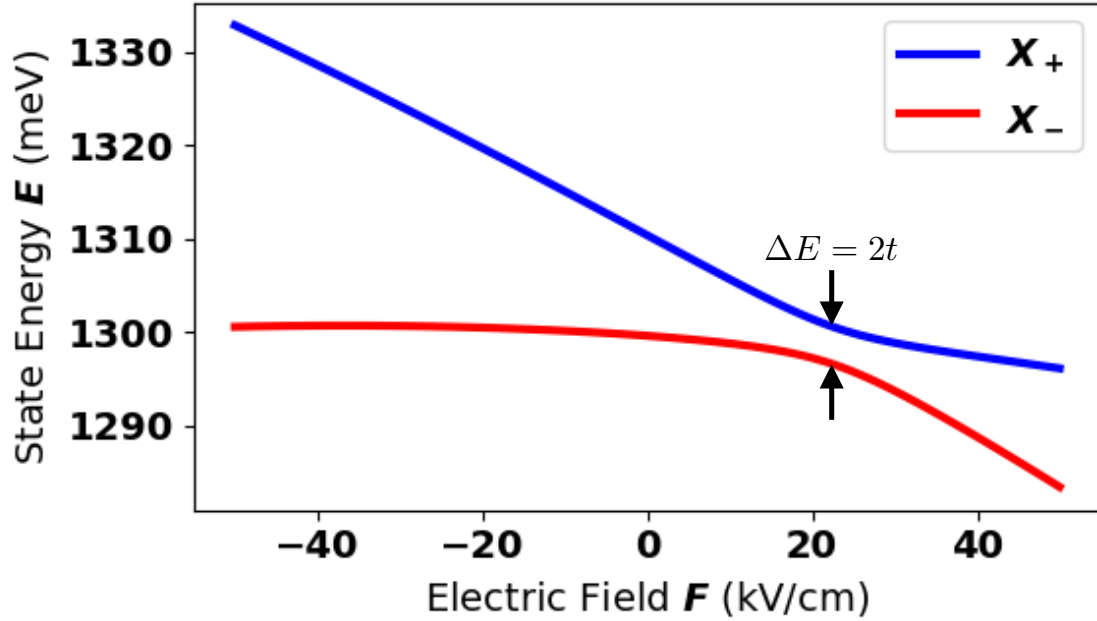


Figure 2.6: Energy as a function of applied electric field for the bonding  $X_-$  and anti-bonding  $X_+$  modes of the new molecular basis of the neutral exciton. In particular, take note of the avoided crossing at the resonance of the two states. For this graph a tunnel coupling of  $t = 2$  meV was used.

and the new molecular eigenstates are defined as

$$|X_{\pm}\rangle = \frac{1}{\sqrt{2}} \begin{bmatrix} 1 \\ \pm 1 \end{bmatrix}. \quad (2.18)$$

The energy gap at the anticrossing can be calculated by taking the difference between anti-bonding and bonding modes at the electric field value of the anticrossing. This leads to an anticrossing energy of

$$\Delta E = 2t, \quad (2.19)$$

and provides a method for experimentally measuring the tunnel coupling strength. Fig. 2.6 depicts the energy as a function of applied electric field for a QDM where the QDs are close enough for the wavefunctions to overlap, enabling tunnel coupling.

### Effect of Temperature on the Band Gap

Increasing temperatures are associated with growing amplitudes of vibration for the constituent atoms of a crystal. These larger vibrations lead to larger average interatomic spacings. This causes the electrons to experience smaller average potentials, thereby lowering the band gap energy. Varshni's law [37] is an empirical formula that relates the band gap energy of a semiconductor to its temperature:

$$E_g(T) = E_g(0) - \frac{\alpha T^2}{\beta + T}. \quad (2.20)$$



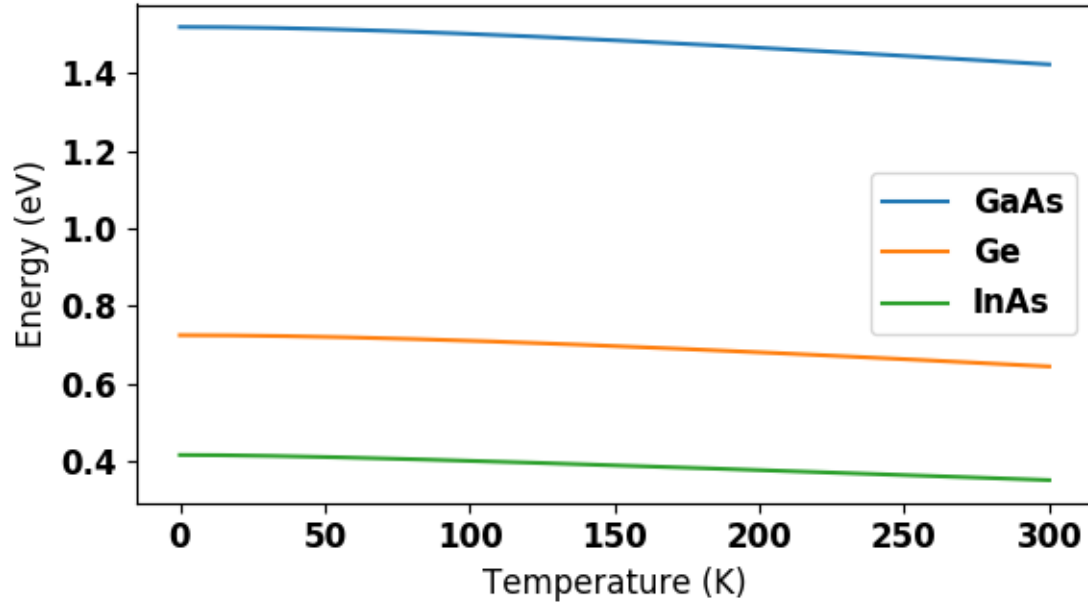


Figure 2.7: Bandgap energy as a function of temperature for GaAs, Ge, and InAs materials. Values from Table 2.2 were used to generate these plots.

In this equation,  $E_g(0)$  is the bandgap energy at 0 K and  $T$  is the temperature.  $E_g(0)$ ,  $\alpha$ , and  $\beta$  are used as fit parameters. Table 2.2 contains literature values for gallium arsenide (GaAs), germanium (Ge), and indium arsenide (InAs) semiconducting materials. Figure 2.7 shows the dependence of the bandgap on the temperature of the material for GaAs, Ge, and InAs.

	GaAs	Ge	InAs
$E_g(0)$ (eV)	1.519	0.724	0.415
$\alpha$ ( $10^{-4} eV K^{-1}$ )	5.405	4.8	2.76
$\beta$ (K)	204	235	83

Table 2.2: Table of parameters used to calculate band gap energies as a function of temperature for GaAs, Ge, and InAs [38, 39, 40].

## 2.6 Photoluminescence

PL is the emission of light from a material following the absorption of a photon. During the absorption process, an electron from the material's ground state is promoted to a higher-lying excited state. Luminescence occurs during the emission process, due to the excited electron emitting a photon while relaxing back to the ground state. As a spectroscopic

technique, PL is a straightforward and non-destructive method of accessing information regarding a system's electronic energy level structure. Fig. 2.8 displays a schematic diagram which illustrates the absorption and emission processes that occur during the PL of a QD.

The energy levels of the valence and conduction bands can be approximated by modeling the system as a particle in a box. Mathematically this is known as the one-dimensional infinite square well because the potential energy is treated as zero inside the box and infinite everywhere else, i.e.

$$U(z) = \begin{cases} 0, & \text{if } 0 < x < L \\ \infty, & \text{otherwise.} \end{cases} \quad (2.21)$$

Solving Schrödinger's equation for the particle in a box yields the wavefunctions

$$\psi_n(z) = \sqrt{\frac{2}{L}} \sin\left(\frac{n\pi z}{L}\right), \quad (2.22)$$

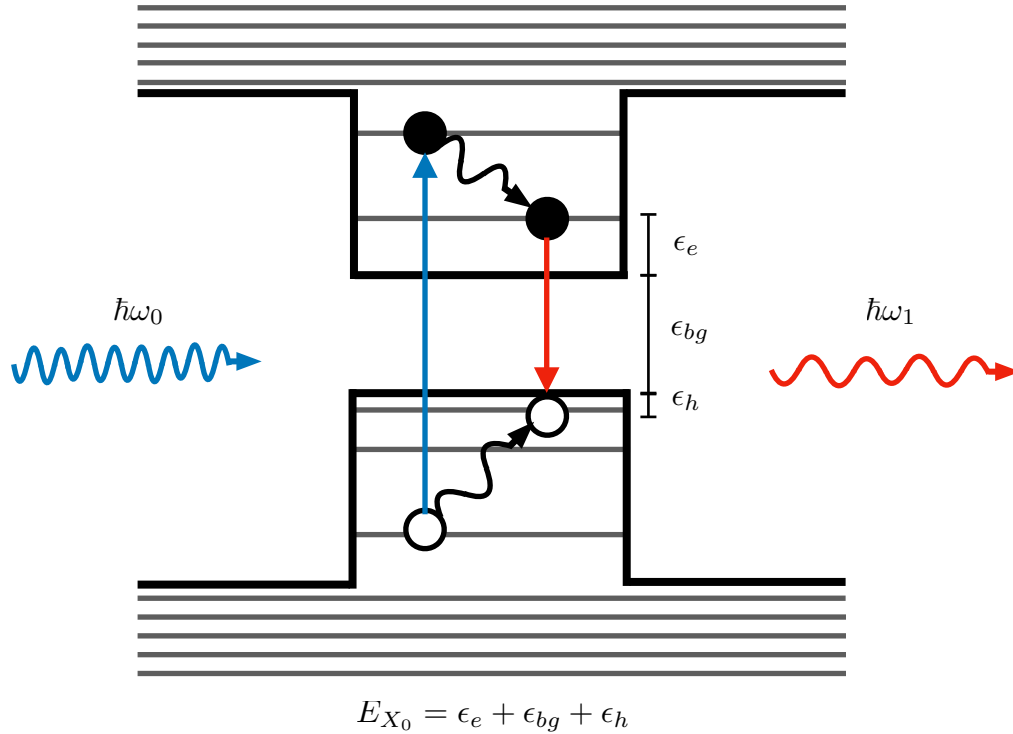


Figure 2.8: Schematic diagram detailing the various transitions that occur during the PL process of a QD. Absorption of a photon (blue) of energy  $\hbar\omega_0$  excites an electron from the valence band into the conduction band, leaving behind a hole. The electron and hole, together known as an exciton, undergo non-radiative relaxation through the emission of phonons (black), putting the charges into the lowest energy configuration. Emission of a photon (red) of energy  $\hbar\omega_1 < \hbar\omega_0$  occurs when the electron returns to the valence band and recombines with the hole. For neutral excitons in InAs QDs grown in GaAs, typical radiative relaxation times are around 800ps [41].

and the energies

$$E_n = \frac{\pi^2 \hbar^2 n^2}{2m_{eff} L^2}, \quad (2.23)$$

where  $n = 1$  corresponds to the lowest possible state. For a realistic QD system, such as InAs QDs grown in GaAs, the potential energy outside of the well is finite. However, the key points are present, namely the energy of the bound states are inversely proportional to the mass of the particle  $m_{eff}$  and the size of the box  $L$ . At first glance this allows us to assign a smaller confinement potential to the holes due to their larger effective mass, as can be seen in Fig. 2.3.

### Exciton recombination

The phenomenon of PL, in the context of QDs, occurs when the electron-hole pair that makes up an exciton recombines and emits a photon. Detection of this photon allows for measurements to be made on the energy level structure of the QDs. For example, a QD in the crystal ground state consisting of no extra charges can undergo photoexcitation into an excited state consisting of an electron-hole pair. This excited state is known as the neutral exciton and upon recombination emits a photon whose energy is equal to the difference between excited and ground states. By setting the energy of the crystal ground state equal to zero, the transition energies can be directly mapped to the state energies.

### Identifying Charge States

As well as neutral excitons, charged excitons can be created through the use of electric field tuning and optical excitation. Radiative recombination still occurs in these charged excitons, leaving behind a bare charge in the ground state. The relative energy shifts of the QD system due to adding charges can be calculated theoretically and compared to experimental data. Through comparisons with the theoretical model, it is possible to identify the individual charge states of a QD. The different charge states are only stable within specific electric field values, outside of which the charges tend to tunnel to the doped substrate layers. These so-called *charge stability regions* can also aid in identifying the different charge states of a QD. When the electric field is applied to the sample, the different charge states of the QD will emit within these charge stability regions. As the field progresses in magnitude, negative charge states will dim out as neutral charge states begin to brighten. When the neutral states begin to finally dim, the positive charge states will begin to brighten [42]. This will continue to occur with a charging mechanism that charges the QDs one charge at a time as a function of the applied electric field.

### Effects of Tunneling and Fine Structure

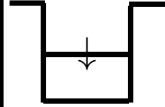
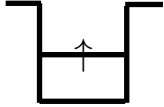
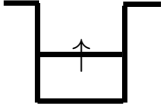
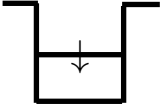
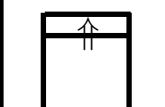
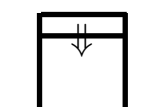
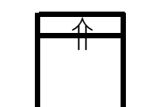
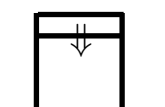
	Bright		Dark	
Conduction Band				
Valence Band				
$m_j$	+1	-1	+2	-2

Figure 2.9: Simple schematic depicting the four different spin states of a neutral exciton in a QD and the total sum of  $m_j$  for each state.

A neutral exciton is made up of a conduction band electron and a valence band hole, typically a heavy hole due to their lower energies. These particles possess properties other than their charge, which can be leveraged to learn more about the system. The angular momentum of these particles is of particular interest. The conduction band electrons exist in an  $s$ -like orbital with no spin orbit coupling, yielding a  $z$ -component of the total angular momentum of  $m_j = \pm 1/2$ . The heavy holes in the valence band, however, exist in a  $p$ -like orbital with strong spin-orbit coupling, yielding  $m_j = \pm 3/2$  [42]. Therefore, a neutral exciton in a QD can exist in one of four degenerate angular momentum states as shown in Fig. 2.9.

If QDMs are being studied, fine structure can be observed in the avoided crossings of the electric field dispersed photoluminescence spectra, even at zero magnetic field [43, 44, 45]. Identification is possible due to the nature of tunneling and the Pauli exclusion principle. Quantum states containing pairs of holes or electrons cannot undergo tunneling if the two charges have identical spin projections. This prevents the tunneling of triplet states and leads to emission lines that pass through avoided crossings.

### Bright and Dark States

As can be seen from Fig. 2.9, there are two main types of neutral excitons, bright and dark. The bright excitons have a  $z$ -projection of the total angular momentum of  $m_j = \pm 1$  while the dark excitons have projection  $m_j = \pm 2$ . Optical selection rules for electronic transitions dictate that only changes of  $\Delta m_j = 0, \pm 1$  are allowed. This is why the  $m_j = \pm 2$  excitons are known as dark transitions; their recombination does not result in the emission of a photon.

### Electron-Hole Exchange

Exchange interactions are a quantum mechanical phenomenon that occur between identical particles. Because the hole in the valence band is really a mathematical abstraction of a missing electron, there can exist an exchange interaction between electrons and holes. The effect is a result of the wavefunctions of indistinguishable particles being subject to exchange symmetries. One can think of it like the effect of inverting the sign of the argument of an even or odd function. The result is that the wavefunction either remains unchanged (symmetric) or inverts its sign (antisymmetric) when two particles are exchanged. Fermionic and Bosonic particles can both experience exchange interactions. In Fermions the exchange interaction results in a repulsion of the two particles, known as Pauli repulsion, and is related to the Pauli exclusion principle. In Bosons the exchange interaction results in an attraction of the particles and leads to identical particles swarming together resulting in a Bose-Einstein condensate.

As an example, we will derive the exchange energy for the two electrons in a hydrogen molecule-like system. We begin by assuming that the two electrons are independent particles and expressing their wavefunctions in position space. The wavefunction for the first electron will be denoted  $\Phi_a(\vec{r}_1)$  and the wavefunction for the second electron will be denoted  $\Phi_b(\vec{r}_2)$ . It is assumed that  $\Phi_a$  and  $\Phi_b$  are orthogonal and that each wavefunction is an eigenfunction of the corresponding electron. The wavefunction for the entire system can be constructed using symmetric and antisymmetric combinations of the products of these two wavefunctions:

$$\Psi_S(\vec{r}_1, \vec{r}_2) = \frac{1}{\sqrt{2}} [\Phi_a(\vec{r}_1)\Phi_b(\vec{r}_2) + \Phi_b(\vec{r}_1)\Phi_a(\vec{r}_2)], \quad (2.24)$$

and

$$\Psi_A(\vec{r}_1, \vec{r}_2) = \frac{1}{\sqrt{2}} [\Phi_a(\vec{r}_1)\Phi_b(\vec{r}_2) - \Phi_b(\vec{r}_1)\Phi_a(\vec{r}_2)]. \quad (2.25)$$

If we treat the exchange interaction in the hydrogen molecule using the perturbation method, we can write the overall Hamiltonian as:

$$H = H^{(0)} + H^{(1)}. \quad (2.26)$$

The unperturbed Hamiltonian can be written as

$$H^{(0)} = -\frac{\hbar^2}{2m} (\nabla_1^2 + \nabla_2^2) - \frac{e^2}{r_1} - \frac{e^2}{r_2}, \quad (2.27)$$

and the perturbation term can be written as

$$H^{(1)} = \left( \frac{e^2}{R_{ab}} + \frac{e^2}{r_{12}} - \frac{e^2}{r_{a1}} - \frac{e^2}{r_{b2}} \right). \quad (2.28)$$

Solving for the eigenvalues of the Hamiltonians yields

$$E_{\pm} = E_{(0)} + \frac{C \pm J_{ex}}{1 \pm B^2}, \quad (2.29)$$

where  $B$  is the overlap integral,  $C$  is the Coulomb integral, and  $J_{ex}$  is the exchange integral. The sum in Eq. (2.29) describes the symmetric solution and the difference describes the spatially antisymmetric solution. The overlap, Coulomb, and exchange integrals are defined as:

$$B = \int \Phi_b(\vec{r}_2)\Phi_a(\vec{r}_2)d^3r_2, \quad (2.30)$$

$$C = \int \Phi_a^2(\vec{r}_1) \left( \frac{1}{R_{ab}} + \frac{1}{r_{12}} - \frac{1}{r_{a1}} - \frac{1}{r_{b2}} \right) \Phi_b^2(\vec{r}_2)d^3r_1d^3r_2, \quad (2.31)$$

and

$$J_{ex} = \int \Phi_a^*(\vec{r}_1)\Phi_b^*(\vec{r}_2) \left( \frac{1}{R_{ab}} + \frac{1}{r_{12}} - \frac{1}{r_{a1}} - \frac{1}{r_{b2}} \right) \Phi_b(\vec{r}_1)\Phi_a(\vec{r}_2)d^3r_1d^3r_2, \quad (2.32)$$

respectively. In these equations, the terms  $R_{ab}$ ,  $r_{12}$ , and  $r_{a1,a2,b1,b2}$  correspond to the Coulombic repulsion of the two protons of the individual hydrogen atoms, the repulsion of the two electrons, and the attraction between the individual protons and electrons, respectively.

In addition to the exchange interaction involving the swapping of particle positions, there also exists a spin exchange interaction that involves the swapping of the spin of two identical particles. When including the spin, there exists symmetric and antisymmetric combinations of the spin variables and their combination with the position wavefunctions, now called the orbital wavefunction, result in the spin-orbitals. The consequence of including the spin is that when the orbital wavefunction is symmetric, the spin wavefunction must be antisymmetric and vice versa. With this in mind, we can see that when the spatial wavefunction is symmetric the spin wavefunction results in the antisymmetric, spin-singlet, solution. Whereas the antisymmetric spatial wavefunction must be coupled with the symmetric, spin-triplet, solution. The resulting exchange interaction including spin is:

$$E_{ex} = C - \frac{1}{2}J_{ex} - 2J_{ex}\langle \vec{S}_a \cdot \vec{S}_b \rangle, \quad (2.33)$$

where  $\langle \vec{S}_a \rangle$  and  $\langle \vec{S}_b \rangle$  are the spin momenta of the two particles.

## 2.7 Phonons and Polarons

Phonons are quantized vibrations of a crystal lattice. In nature, there exist two types of phonons. Acoustic phonons are present in every material and are the coherent motion of atoms in a lattice away from their equilibrium positions (see Fig. 2.12). Optical phonons, however, are only present in materials that have at least two atoms contained in a single lattice basis. This is the result of optical phonons being the out of phase motion of nearby atoms in a crystal (see Fig. 2.12). The term optical comes from the observation that in ionic structures, such as potassium chloride, these phonons are excited by infrared radiation. Each of the two types of phonons has three modes. There are two transverse modes and one longitudinal mode. The transverse modes of vibration occur when the atoms of a crystal are vibrating perpendicular to the propagation direction of the wave and the longitudinal modes occur when the atoms are vibrating parallel to the propagation direction of the wave.

Until now, we have only considered the stationary electronic states of the system. This is due to the underlying assumption that the lattice ions remain static. When this assumption is removed, the solutions to the system must account for vibrations of the ionic cores about their equilibrium positions. These solutions lead to vibrational waves in the crystal lattice, which in their quantized form are coined phonons. Additionally, these phonons can couple with the electronic states of the crystal to produce quasi-particles known as polarons. Typically, the phonons that exist in QD and QDM systems are regarded as an unwanted byproduct resulting in the generation of heat. This decoherent expenditure of energy is often the cause of non-radiative relaxation of excited excitonic states back to the ground state of the exciton [46, 47], an effect that is not present in the gaseous state of atomic physics, which is why rubidium vapor-cell atomic clocks have such enormous coherence times [48]. In this section, we derive the equations for a crystal structure experiencing atomic vibrations and discuss the vibrational states of matter that arise. We will begin with a classical description of a one-dimensional chain of atoms in a diatomic crystal.

### Classical Derivation of Phonons

The analysis of a one-dimensional diatomic chain of atoms is a simple system which yields interesting insights into the nature of vibrations in diatomic structures such as GaAs and InAs. A diatomic system is one in which two atoms occupy a single basis of the repeating crystal structure. The normal mode solutions of the vibrations in these structures result in two sets of waves that depend on the underlying motion of the ion cores involved. There exist low energy acoustic waves which occur when both ionic species are traveling in the same direction, and higher energy optical waves which occur when the two ionic species are traveling in opposite directions. The following derivation will only yield results for the longitudinal modes, atoms traveling along the axis of propagation of the wave, of these two sets of vibrational motion; however there also exist transverse modes along each of the axes orthogonal to the propagation of the wave.

We begin our analysis by considering the one-dimensional crystal depicted in Fig. 2.10 consisting of a repeated basis of two atomic species of mass  $M_A$  and  $M_B$ , where  $M_B > M_A$ . The lattice constant  $a$  represents the distance between neighboring bases and for the sake of simplicity, we will set the two ionic species apart by half the lattice spacing  $a/2$ . By this approximation the bond strength between the two species is assumed to be the same and is represented by the stiffness coefficient  $K$ . This effectively allows us to treat the individual ions as being held together by tiny springs, an assumption that is called the harmonic approximation because it implies that the potential energy of the crystal is a quadratic function of the displacement of the ions. This approximation is valid as long as the displacements of the ion cores is relatively small. Lastly, the displacement of an individual ion from its equilibrium position will be represented by  $u_m$  or  $u_n$  depending on whether the ionic species is of type  $A$  or  $B$ , respectively.

We start the derivation by writing down the sum of forces on the  $m$  and  $n$ th ions due

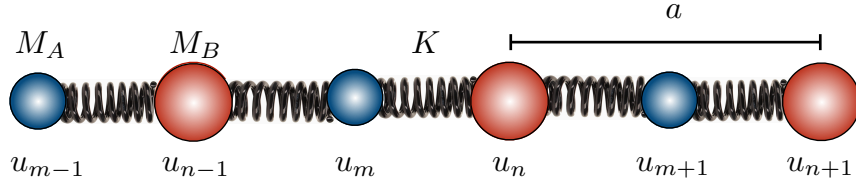


Figure 2.10: Diagram showing the parameters used to derive the normal phonon modes of a one-dimensional diatomic chain of atoms.

to their nearest neighbors, which sum to:

$$F_{A,m} = M_A \frac{d^2 u_m}{dt^2} = -K(u_m - u_{n-1}) - K(u_m - u_n), \quad (2.34a)$$

$$F_{B,n} = M_B \frac{d^2 u_n}{dt^2} = -K(u_n - u_m) - K(u_n - u_{m+1}). \quad (2.34b)$$

The displacement of a harmonic oscillator is a sinusoidal function of time and space. Therefore, we can write equations for the displacement of the  $m$  and  $n$ th ions as:

$$u_m = A_0 e^{-i(\omega t - mka)}, \quad (2.35a)$$

$$u_n = B_0 e^{-i(\omega t - nka)}, \quad (2.35b)$$

where  $\omega$  is the resonant frequency of the vibrational mode and  $k = 2\pi/\lambda$  is the wavevector. The wavevector can only take on specific values and is restricted by the boundary conditions of the crystal lattice. Because we are not interested in edge effects on the solutions to this equation, we can make use of the Born-von Karman boundary conditions which treats the linear chain of ions as having a periodic boundary [49]. This results in the ions of the first basis being connected to the ions in the last basis, which can be written mathematically as

$$u_{m=0} = u_{m=N}, \quad (2.36a)$$

$$u_{n=1} = u_{n=N+1}. \quad (2.36b)$$

This condition treats  $n = 1$  as the first basis and  $n = N$  as the last. By substituting Eq. (2.36) into Eq. (2.35), we find that the following condition must be true:

$$e^{iNka} = 1. \quad (2.37)$$

From this condition, it is apparent that  $k$  must follow the relation

$$k = \frac{2\pi}{Na} p, \quad (2.38)$$

where  $p$  is an integer. Due to the periodic nature of Eq. (2.35), the displacements will be unaffected if  $k$  changes by the amount  $2\pi/a$ . Therefore, there are only  $N$  independent values of  $k$  that yield unique solutions. The range of  $k$  values, by convention, is set to be



$-\pi/a \leq k \leq \pi/a$ . This range of  $k$  values is known as the first Brillouin zone of the crystal lattice.

We can now substitute Eq. (2.35) into Eq. (2.34) to obtain:

$$(2K - M_A\omega^2) A_0 - K(1 + e^{ika}) B_0 = 0 \quad (2.39a)$$

$$(2K - M_B\omega^2) B_0 - K(1 + e^{-ika}) A_0 = 0. \quad (2.39b)$$

We can solve this set of equations by taking the ratio of  $A_0$  to  $B_0$  for each equation and setting them equal to each other. After some algebra, this yields

$$(M_A M_B)\omega^4 - 2K(M_A + M_B)\omega^2 + 4K^2 \sin^2\left(\frac{ka}{2}\right) = 0. \quad (2.40)$$

Equation (2.40) may be solved for  $\omega^2$  as a function of the wavevector  $k$  by use of the quadratic formula and some algebra for simplifying, yielding

$$\omega^2 = K \left[ \left( \frac{1}{M_A} + \frac{1}{M_B} \right) \pm \sqrt{\frac{1}{M_A^2} + \frac{1}{M_B^2} + \frac{2}{M_A M_B} \cos(ka)} \right]. \quad (2.41)$$

Equation (2.41) has two distinct solutions. The solution resulting from the sum gives the optical branch of the phonon dispersion relation while the difference gives the acoustic branch. Due to the wavevector  $k$  being able to take on a total of  $N$  unique values, there are a total of  $N$  normal vibrational modes for the longitudinal phonons.

Some insight can be gained by examining the limiting cases of Eq. (2.41). The first case we will look at is the so-called long wavelength limit where  $k \rightarrow 0$ . For the longitudinal optical phonons this results in

$$\omega_{optical}|_{k \rightarrow 0} = \sqrt{2K \left( \frac{1}{M_A} + \frac{1}{M_B} \right)}, \quad (2.42)$$

and for the longitudinal acoustic phonons this results in

$$\omega_{acoustic}|_{k \rightarrow 0} = \sqrt{\frac{K}{2(M_A + M_B)}} ka. \quad (2.43)$$

The solution to the long wavelength limit of the acoustic modes requires the use of a Taylor expansion in  $k$  to second order. At this point, it is clear how the nomenclature for the acoustic mode came to be, since sound waves in solid materials exhibit a linear dispersion relation. Optical phonons, however, achieved their name through the fact that optical phonons in ionic crystals, like gallium arsenide and indium arsenide, are excited by infrared radiation. This is because the electric field of the incident radiation will move all of the positive ions in the direction of the field and all of the negative ions in the opposite direction, causing the crystal to vibrate.

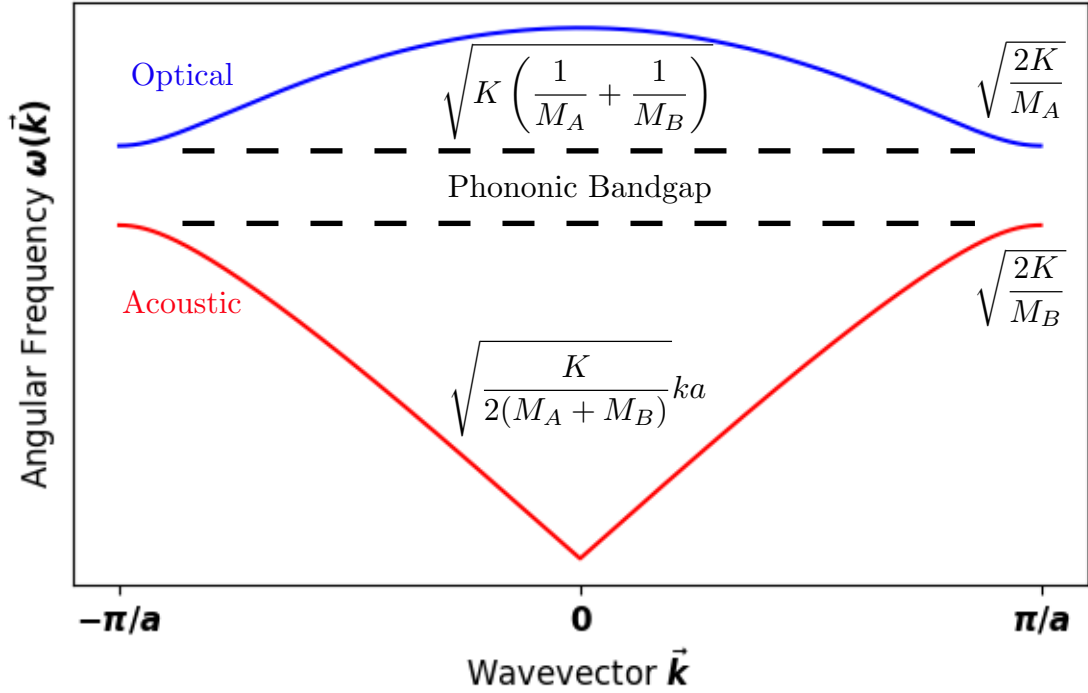


Figure 2.11: Phonon dispersion curve for a one-dimensional diatomic chain of atoms. The acoustic branch has a linear response to the wavevector at the long wavelength limit, while the optical branch is approximately dispersionless.

The other limiting case can be examined by setting  $k = \pm\pi/a$ . This will shed light on the value of the optical and acoustic phonon bands at the Brillouin zone edge. For the optical phonons this leads to a frequency of

$$\omega_{optical}(k \rightarrow \pm\pi/a) = \sqrt{\frac{2K}{M_A}}, \quad (2.44)$$

and for the acoustic phonons this leads to a frequency of

$$\omega_{acoustic}(k \rightarrow \pm\pi/a) = \sqrt{\frac{2K}{M_B}}. \quad (2.45)$$

Figure 2.11 shows the longitudinal optical and acoustic phonon dispersion curves for gallium arsenide. In this case,  $M_A = M_{Ga}$  and  $M_B = M_{As}$  and  $M_B > M_A$ .

One final treatment of the equations derived thus far shows an important difference in the motion between the two vibrational modes. By taking the ratio of the amplitudes of the displacement of the individual ions  $u_m/u_n$  in the limiting case of  $k \rightarrow 0$ , we can determine the relative motions of the ions. This results in :

$$\left(\frac{u_m}{u_n}\right)_{optical} = \left(\frac{A_0}{B_0}\right)_{optical} = -\frac{M_B}{M_A}, \quad (2.46)$$

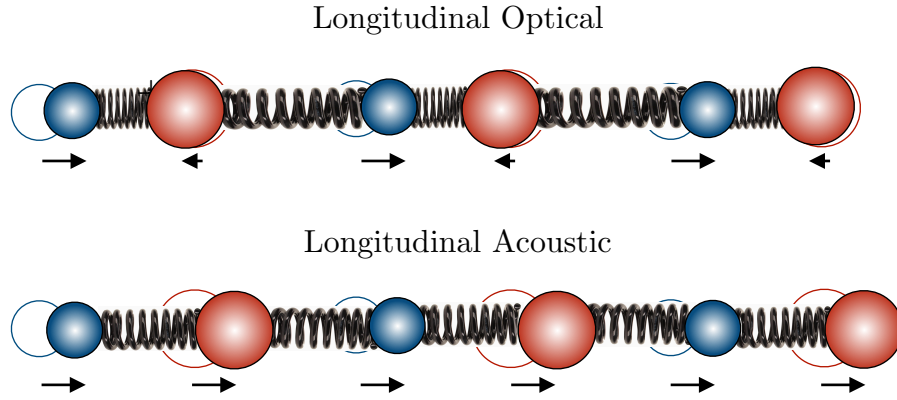


Figure 2.12: Optical and acoustic phonon modes represented by a linear chain of atoms in a diatomic compound. Although only the longitudinal modes are shown here, there are two transverse phonon modes for both the optical and acoustic phonons.

for the optical phonons, and

$$\left( \frac{u_m}{u_n} \right)_{acoustic} = \left( \frac{A_0}{B_0} \right)_{acoustic} = 1, \quad (2.47)$$

for the acoustic phonons. This result reveals that the optical phonon is a vibrational mode in which the two ions travel in opposite directions, out of phase, and are weighted by their masses. For ionic crystals this causes a time-varying oscillation of the dipole moment. Acoustic phonons, however, are a result of both ions traveling in the same direction with the same relative amplitude. Figure 2.12 shows the two types of vibrational modes of a one-dimensional diatomic lattice.

### Quantum Mechanical Treatment of Phonons

In this section, we will quantize the linear chain of atoms to better understand the quantum mechanical nature of vibrations in a crystal lattice. The methods described in this section adopt the formalism of Altland and Simons [50]. We start by defining the Hamiltonian of the system as the sum of kinetic and potential energies for all of the atoms along a one-dimensional monatomic crystal:

$$\hat{H} = \sum_{n=1}^N \left[ \frac{\pi_n^2}{2m} + \frac{1}{2} K (\phi_{n+1} - \phi_n)^2 \right], \quad (2.48)$$

where  $\pi_n$  and  $\phi_n$  are the momentum and displacement operators for the  $n$ th atom in the chain.

Through the use of a Fourier transform, we may obtain a canonically conjugate form of the Hamiltonian that resembles a quantum harmonic oscillator. This allows us to write the Hamiltonian as a sum over the normal modes of the wavevector rather than in terms of

the particle coordinates. The discrete Fourier transforms of the fields  $\Pi_k$  and  $\Phi_k$  are related to  $\pi_n$  and  $\phi_n$  by:

$$\Pi_k = \frac{1}{\sqrt{N}} \sum_n e^{ikna} \pi_n, \quad (2.49a)$$

$$\Phi_k = \frac{1}{\sqrt{N}} \sum_n e^{-ikna} \phi_n, \quad (2.49b)$$

and

$$\pi_n = \frac{1}{\sqrt{N}} \sum_k e^{-ikna} \Pi_k, \quad (2.50a)$$

$$\phi_n = \frac{1}{\sqrt{N}} \sum_k e^{ikna} \Phi_k. \quad (2.50b)$$

Substituting Eqs. (2.49a) and (2.49b) into (2.48) yields the discretized form of the Hamiltonian, which resembled that of a quantum harmonic oscillator:

$$\hat{H} = \sum_k \left[ \frac{\hat{\Pi}_k \hat{\Pi}_{-k}}{2m} + \frac{1}{2} m \omega_k^2 \hat{\Phi}_k \hat{\Phi}_{-k} \right], \quad (2.51)$$

where  $\omega_k$  is the frequency of the  $k$ th mode. The frequencies  $\omega_k$  can be determined from Eq. (2.41) by setting both masses equal to each other, halving the lattice spacing, and taking the subtractive form of the quadratic equation because for a monatomic lattice there are no optical phonons. This results in a frequency of

$$\omega_k = \sqrt{\frac{2k}{m} (1 - \cos ka)}. \quad (2.52)$$

We can make a simplification to the Hamiltonian by factoring out  $\hbar\omega_k$ , and defining the dimensionless operators

$$\hat{f}_k = \frac{\hat{\Pi}_k}{\sqrt{2m\hbar\omega_k}}, \quad (2.53a)$$

$$\hat{g}_k = \sqrt{\frac{m\omega_k}{2\hbar}} \hat{\Phi}_k. \quad (2.53b)$$

The resulting Hamiltonian now looks like

$$\hat{H} = \sum_k \hbar\omega_k \left[ \frac{\hat{\pi}_k \hat{\pi}_{-k}}{2m\hbar\omega_k} + \frac{m\omega_k}{2\hbar} \hat{\phi}_k \hat{\phi}_{-k} \right] = \sum_k \hbar\omega_k \left( \hat{f}_k \hat{f}_{-k} + \hat{g}_k \hat{g}_{-k} \right). \quad (2.54)$$

The commutation relation for the operators  $\hat{f}$  and  $\hat{g}$  results in

$$[\hat{f}_k, \hat{g}_{k'}] = -\frac{i}{2} \delta_{kk'}. \quad (2.55)$$

With the commutation relation known, we can define the creation and annihilation operators  $\hat{b}_k^\dagger$  and  $\hat{b}_k$  as

$$\hat{b}_k^\dagger = \hat{g}_{-k} - i\hat{f}_k, \quad (2.56a)$$

$$\hat{b}_k = \hat{g}_k + i\hat{f}_{-k}. \quad (2.56b)$$

The inverse relations are:

$$\hat{f}_k = \frac{i}{2} (\hat{b}_k^\dagger - \hat{b}_{-k}), \quad (2.57a)$$

$$\hat{g}_k = \frac{1}{2} (\hat{b}_k + \hat{b}_{-k}^\dagger). \quad (2.57b)$$

Another important commutation relation is

$$[\hat{b}_k, \hat{b}_{k'}^\dagger] = \delta_{kk'}. \quad (2.58)$$

Substituting Eq. (2.57) into Eq. (2.54) and making use of the commutation relation, Eq. (2.58), yields

$$\hat{H} = \sum_k \hbar\omega_k \left[ \hat{b}_k^\dagger \hat{b}_k + \frac{1}{2} \right]. \quad (2.59)$$

This solution takes the form of a quantum harmonic oscillator. If we let  $|n_k\rangle$  be an eigenstate of the Hamiltonian for each  $k$ , then the creation and annihilation operators cause the following relations:

$$\hat{b}_k^\dagger |n_k\rangle = \sqrt{n+1} |(n+1)_k\rangle, \quad (2.60)$$

and

$$\hat{b}_k |n_k\rangle = \sqrt{n} |(n-1)_k\rangle. \quad (2.61)$$

These results suggest that the phonon creation and annihilation operators act to increase or decrease the number of phonons in a system. The results also allow us to construct the operator product known as the *number operator*  $\hat{b}_k^\dagger \hat{b}_k$  whose eigenvalue is equal to the number of phonons  $n$  in the eigenstate  $|n_k\rangle$ .

$$\hat{b}_k^\dagger \hat{b}_k |n_k\rangle = \sqrt{n} \hat{b}_k^\dagger |(n-1)_k\rangle = n |n_k\rangle \quad (2.62)$$

We can therefore calculate the vibrational energy due to phonons in each mode by acting the Hamiltonian on the eigenstate, resulting in

$$\hat{H}_k |n_k\rangle = \hbar\omega_k \left( \hat{b}_k^\dagger \hat{b}_k + \frac{1}{2} \right) |n_k\rangle = \hbar\omega_k \left( n_k + \frac{1}{2} \right) |n_k\rangle. \quad (2.63)$$

An interesting feature of this result is that even when the total sum of phonons in all the modes is equal to zero, there still exists a vibrational energy equal to  $\hbar\omega_k/2$ . This energy is called the *zero point energy* and is the lowest energy that a quantum mechanical system can have. The physics in this section described the quantization of phonons in a monatomic lattice, however this quantization exists in lattices consisting of more than one atom. It

is therefore possible to create optical phonons in diatomic crystals via laser excitation. In this type of system an excited excitonic state may emit a phonon prior to photon emission from its ground state. Since the process of emitting a phonon is on a faster time scale than the recombination rate of electrons and holes, this enables the experimental technique of excited state spectroscopy through the observation of the lower energy phonon satellites.

### Polarons in QDs

Polarons are quasiparticles consisting of a phonon bound to a charge carrier. When a charge carrier moves through a dielectric material the nearby atoms of the crystal move slightly from their equilibrium positions and effectively screen the charge from the rest of the material (see Fig. 2.13 [51]). The region of space where the atoms are disturbed from their equilibrium positions is known as a phonon cloud and is shown as a dark circle in Fig. 2.13. The combination of the phonon cloud and the mobile charge carrier is called a polaron. A recent study by Kerfoot et al., has shown the existence of coherent interactions between phonons and excitons in QDMs [52]. Their experiments demonstrate the coupling of a longitudinal optical (LO) phonon to a direct neutral exciton, which is also tunnel coupled to an indirect neutral exciton. This three level “V-type” system creates a “which way” path problem between a quasi-continuum state (the polaron created by the LO phonon coupled to the direct neutral exciton) and a discrete state (the indirect neutral exciton). The main findings of the study describe a Fano-type interference caused by coupling the discrete state to the quasi-continuum state resulting in a phonon induced transparency. They call this hybrid state a molecular polaron.

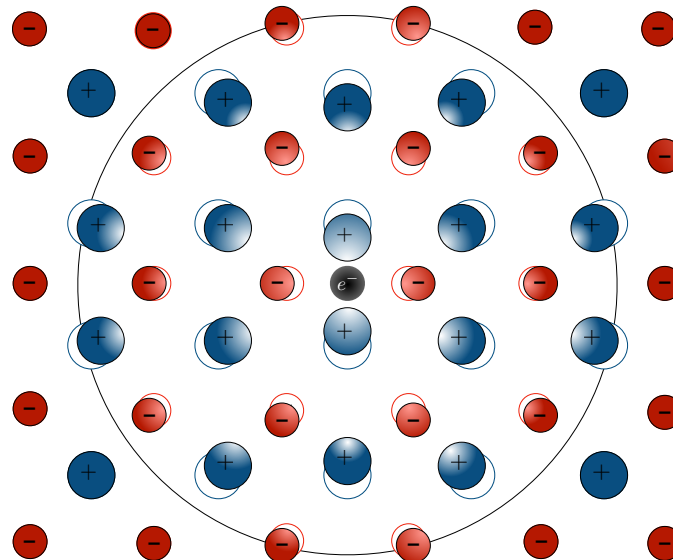


Figure 2.13: The presence of an electron (black) disturbs the nearby atoms causing positive atoms (blue) to shift towards, and negative atoms (red) to shift away from, the electron. The phonon cloud (black ring) and the electron make up the polaron.

# Chapter 3

## Material System

The samples discussed in this dissertation are, at their most fundamental level, epitaxially grown InAs QDs embedded in a GaAs matrix. The various samples utilize a variety of structures that play different roles in the behavior of the device. The electrical properties can be finely tuned by sandwiching the QD system between p-doped or n-doped layers of GaAs. Additionally, barrier layers, typically  $\text{Al}_{0.3}\text{Ga}_{0.7}\text{As}$ , can be added to fine tune the tunneling rates of charge carriers into and out of the QDs. Optical properties can be enhanced by the addition of photonic crystal (PhC) cavities, optical waveguides, or distributed Bragg reflectors (DBR). Lastly, the mechanical properties can be tuned by embedding the QDs into resonators such as tuning forks, micro bridges, or drum head-like membrane structures. The high tunability of these devices derives from the precision of the growth methods and subsequent nanostructuring techniques.

### 3.1 Self-Assembled InAs Quantum Dots

Self-assembled QDs are grown using molecular beam epitaxy (MBE). A popular method of MBE, known as the Stranski-Krastanov (SK) growth method, relies on the lattice mismatch between adjacent layers of semiconducting materials. For InAs quantum dots embedded in a matrix of GaAs, the lattice constant mismatch is approximately 7%. This mismatch causes the deposited InAs to initially form a 2D wetting layer; which accumulates until the build up of strain causes it to plateau at 1.7 monolayers resulting in the subsequent deposition of InAs to pool into droplets [53]. The size of these droplets are on the order of 30nm wide and typically around 5nm tall. The advantages of self-assembled QDs are that the MBE technique allows for atomic precision in the size of the dots along the growth direction and the structures can be easily embedded in other types of semiconducting electronic architectures, such as field effect structures. This allows the manufacturers of such devices to control the energy scales of the dots as well as their electrical environments. Figure 3.1 shows a schematic of how the SK growth technique is typically employed in the design of InAs QDs and QDMs.

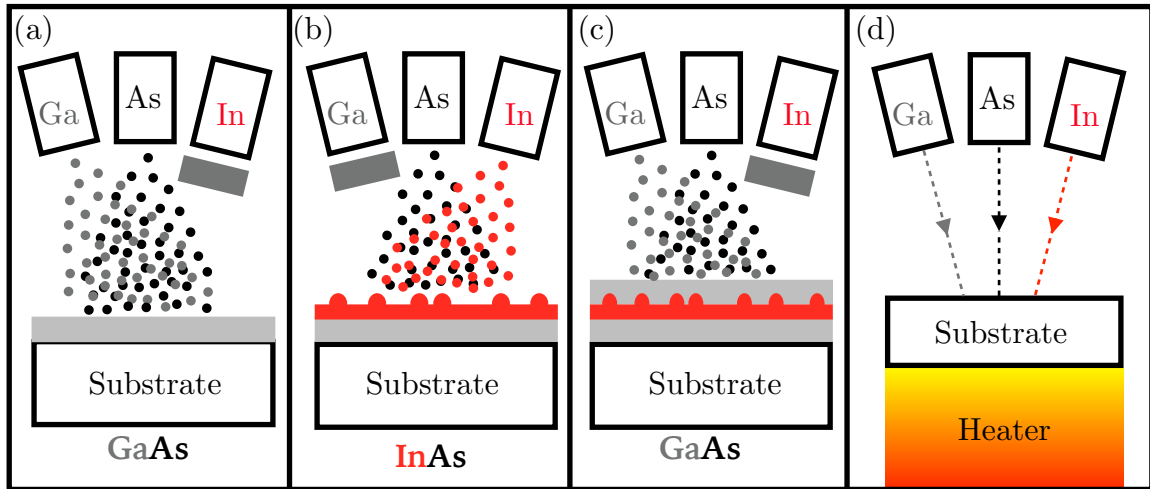


Figure 3.1: Schematic of the SK self-assembled growth method of InAs QDs. (a) The process starts with the deposition of GaAs onto a substrate. (b) Due to strain, the subsequent deposition of InAs plateaus at a thickness of 1.7 monolayers, creating a wetting layer upon which InAs droplets form. (c) The additional deposition of GaAs encapsulates the QDs. The process for fabricating QDMs is to repeat this technique. The build up of lattice strain causes subsequent layers of InAs to preferentially pool into droplets above the initial seed layer of QDs. The process can be repeated a number of times to form multi-dot systems. (d) The schematic of the MBE machine shows how elemental metals contained in individual furnaces can be exposed to the growth chamber by mechanical valves.

## 3.2 Field-Effect Structures

QDs are grown inside the intrinsic region of a field-effect structure where the electric field will have an effect on the electronic energy levels of the device. By controlling this electric field, the ability to electrically tune the properties of the QDs is obtained. The simplest diode is a semiconductor that has one side p-doped and the other side n-doped with an intrinsically doped region in between. The thickness of the intrinsic region can be precisely controlled by the growth process and one can ensure that the QDs are placed at the desired position. The interface between the two oppositely doped sides creates a depletion region where the extra stationary charge carriers are neutralized by the transition of the mobile charge carriers, setting up an intrinsic electric field as a result of the separation of charges. The magnitude of the electric field in this depletion region can be tuned by applying a voltage across the p-doped and n-doped substrates, providing a convenient means of manipulating the electrical state of a QD.

Diodes enable the ability to electrically charge the QDs, promoting the formation of charged excitons. Fig. 3.2 shows the effect of electrical biasing on the conduction and valence band energy levels of a p-i-n diode structure. In this figure,  $E_{C,p}$  ( $E_{C,n}$ ) is the energy of the conduction band,  $E_{V,p}$  ( $E_{V,n}$ ) is the energy of the valence band, and  $E_{F,p}$



( $E_{F,n}$ ) is the Fermi energy at the p-doped (n-doped) edge. Lastly,  $E_B$  is the barrier energy, the energy required to transport an electron from the n-doped edge to the p-doped edge.

At thermal equilibrium the Fermi energies of the conduction band of the n-doped substrate and the valence band of the p-doped substrate are degenerate. However, as the diode is biased in the reverse direction, the Fermi energy of the p-doped edge is raised and the barrier energy increases, further inhibiting the charges from conducting or tunneling through the diode. The opposite is true in forward bias. The ability to control the slope of the intrinsic region of the diode, where the QDMs reside, enables researchers to tune the energy levels of one QD relative to the other. With proper fabrication, the position of the QDs along the growth direction of the diode can be selected with extreme precision. The position of the QDs relative to the doped layers determines whether electrons or holes will more likely tunnel into the dots. If a QD is positioned closer to the p-doped (n-doped) substrate, then holes (electrons) are more likely to tunnel into the QDs. Therefore, the position of a QDM relative to the doped substrates determines which charge carriers can be injected into the QDM. Bracker et. al. go into more detail regarding the fabrication of a QDM system and the effects different dot sizes and positions have on the properties of the system as a whole [54]. In particular they discuss engineering QDM samples in Schottky diodes that promote the tunneling of one type of charge carrier over the other between dots. As a quick summary, when the bottom (top) dot is larger than the top (bottom) dot then electrons (holes) will tunnel under forward bias, while holes (electrons) will tunnel under reverse bias.

The diode structure itself can be modified in numerous ways to gain access to a larger parameter space of sample properties, or can be used for purposes of simplifying certain aspects of an experiment. For example, Schottky diodes, made by the heterojunction of a conducting material and a semiconducting material, allow for the addition of aluminum aperture masks. These masks are not used because of their changes to the electrical properties, rather they are used because they reduce the number of visible QDs in a photoluminescence experiment, creating a spectrum that is less convoluted and easier to analyze. Fig. 3.2 shows the layer structure of a QDM embedded in an n-i Schottky-type diode and topped with an aluminum aperture mask.

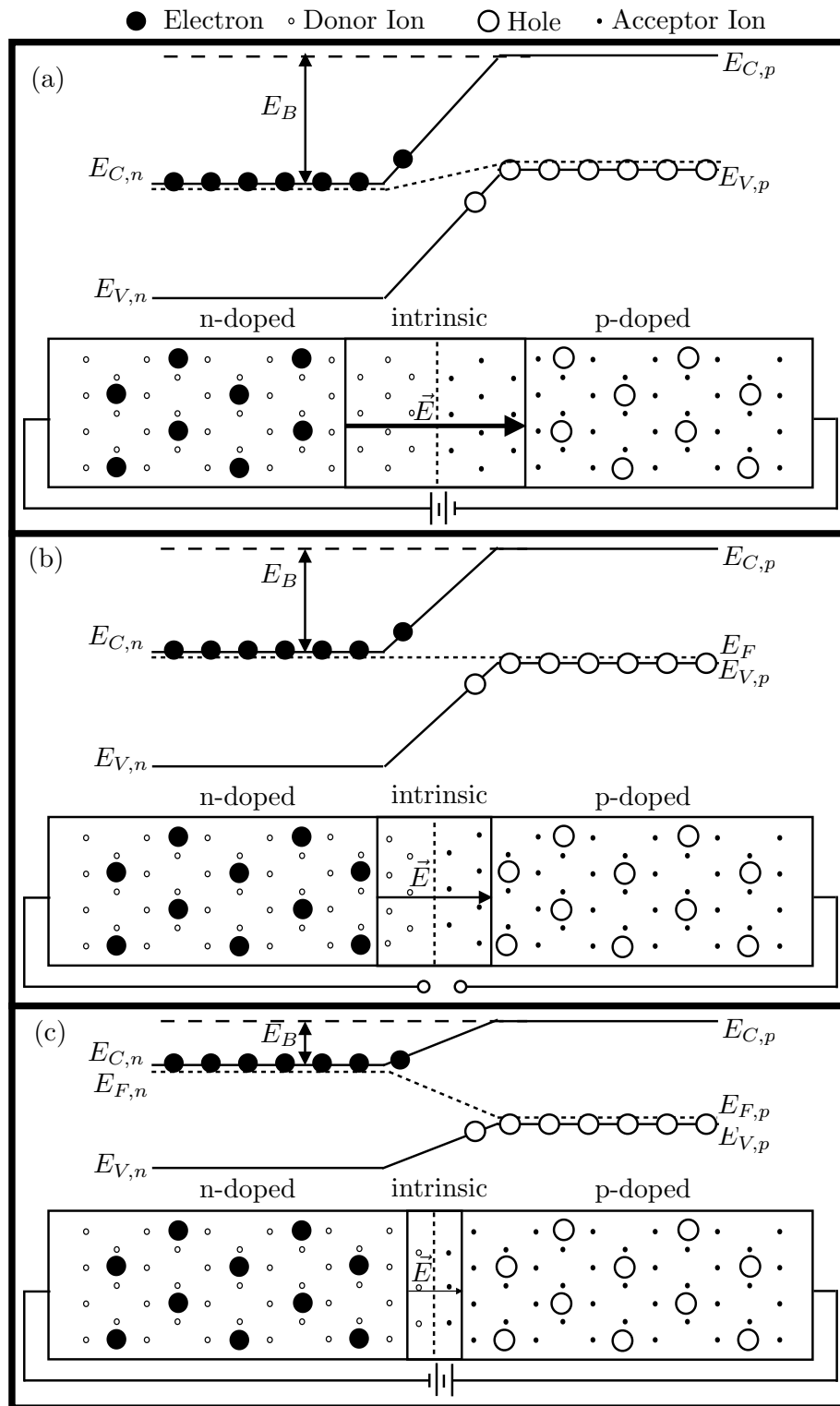


Figure 3.2: (Top) Band edge diagram and (Bottom) electrical circuit of a pn junction based diode under the application of (a) reverse bias, (b) zero bias, and (c) forward bias conditions.

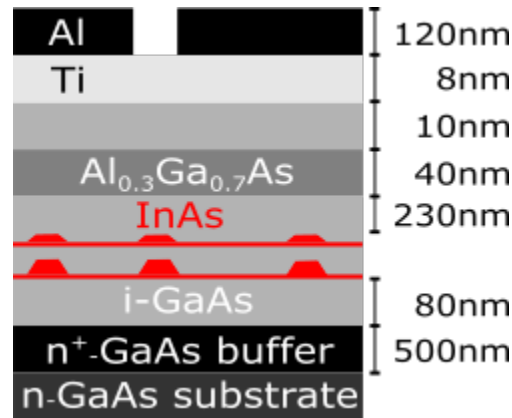


Figure 3.3: Sample layer structure diagram. The aluminum aperture mask provides a  $1\ \mu\text{m}$  diameter window through which PL can be collected. This serves the purpose of reducing the amount of PL from nearby QDMs reaching the detector [55].

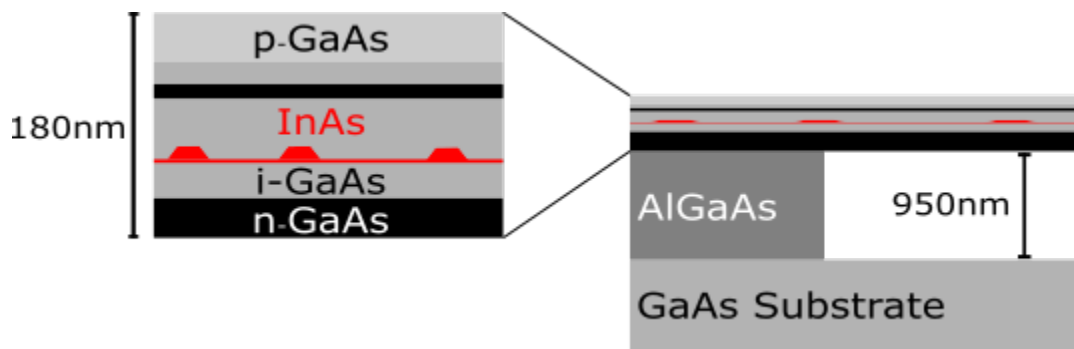


Figure 3.4: Sample layer structure diagram. The sacrificial AlGaAs layer is etched away to form a 180nm thin free floating surface. This becomes the template upon which further patterns, such as photonic crystal cavities, waveguides, tuning forks, and micro-bridges, will be etched. The QDs are in the intrinsic region of an n-i-n-i-p diode structure [13].

Alternative examples are the patterned structures of Carter et. al. [13]. In these samples, a sacrificial layer of  $\text{Al}_{0.3}\text{Ga}_{0.7}\text{As}$  is removed to create thin free-floating membranes, tuning forks, and micro bridges. Fig. 3.4 shows the layer structure of such a device.

### 3.3 Patterned Structures

Different types of patterned structures are etched into the surface of these free-floating membranes. For example, PhC cavity patterns are created because of their ability to enhance the emission intensity of nearby emitters which are resonant with the cavity through the Purcell effect [56]. The PhC cavities affect photons in a material similar to the way ionic lattices affect electrons in solids.

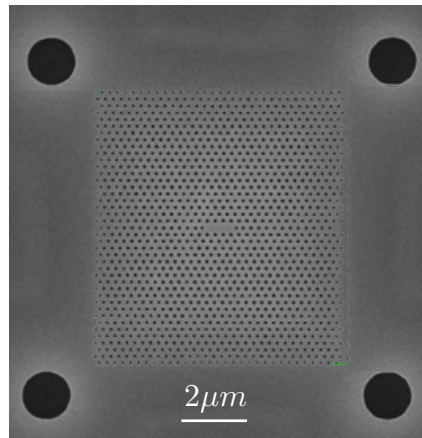


Figure 3.5: Scanning electron microscope image of a photonic crystal cavity structure. The black circles at the corners are drain holes used to remove the sacrificial layer beneath the photonic crystal cavity pattern to create a suspended membrane that is used to couple mechanical motion to the QDs [13].

Optical waveguides have been created with nearby PhC cavities for the purpose of studying cavity coupled modes. The dark-grey semicircular patterns at the left and right edges of Fig. 3.6 are optical couplers that enhance the input and output efficiency of light.

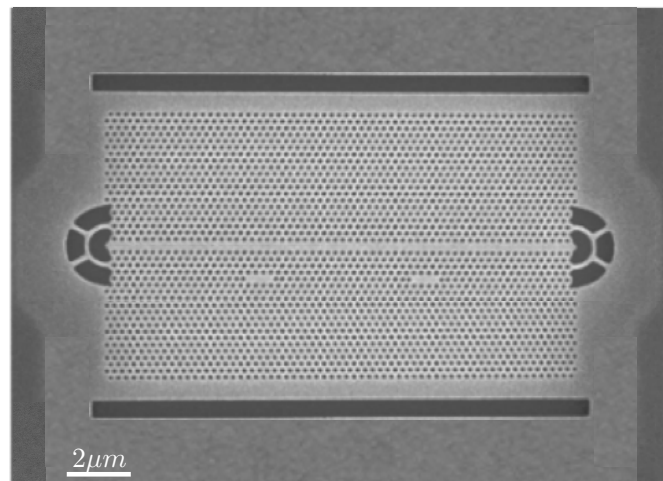


Figure 3.6: Scanning electron microscope image of an optical waveguide with two adjacent PhC cavity structures. On the left and right side of the structure are optical input and output couplers, allowing for a higher efficiency coupling of light. The dark trenches at the top and bottom edge are used to remove the sacrificial layer beneath the photonic crystal cavity pattern to create a suspended membrane that is used to couple mechanical motion to the QDs [13].

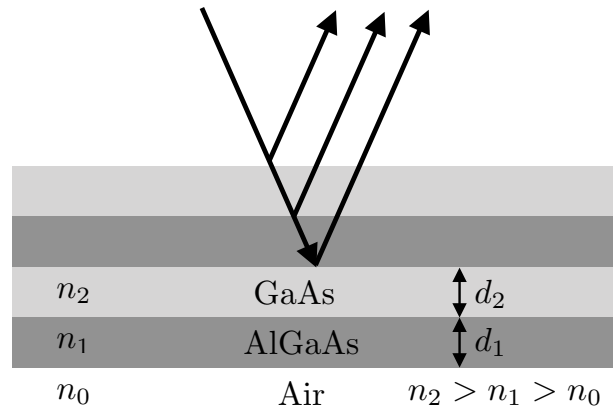


Figure 3.7: Schematic of a distributed Bragg reflector. This structure is used to enhance the coupling of light out of the QDs. The index of refraction of the materials are represented by  $n_i$  and the thickness of the layers are represented by  $d_i$ . For constructive interference, the layer thickness must be proportional to the wavelength of light according to  $d_i = \lambda/4n_i$ .

Another type of patterned structure is a DBR, which is also used to enhance emission of a certain wavelength of light. The addition of multiple layers creates a DBR with a high quality factor. The constructive interference of the resonant wavelength of light causes the enhancement.

Mechanical structures such as tuning forks or bridges can also be constructed. Figure 3.8 shows a scanning electron microscope (SEM) image of these structures. Embedding QDs into tuning fork and bridge structures allows for control of the elastic environment to which the QDs are exposed. When straining these mechanical structures, a shift in the optical properties of the QDs is observed. This type of system couples the mechanical motion of the resonator to the quantum mechanical properties of the QD. One of the major goals of this research is to create a strain sensor based on this coupling.

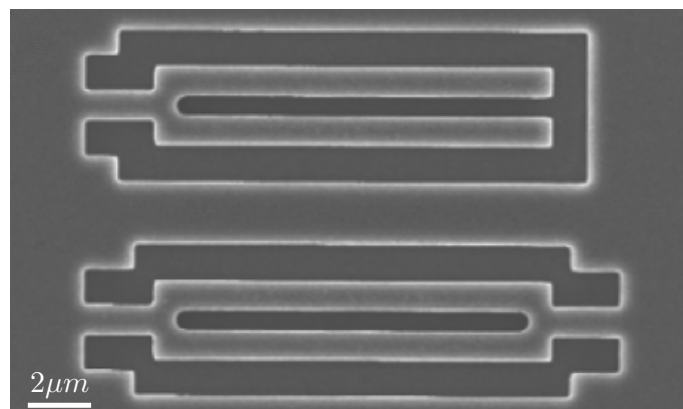


Figure 3.8: Scanning electron microscope image of a tuning fork (top) and a bridge (bottom) mechanical resonator [13].

# Chapter 4

## Experimental Techniques and Procedures

The techniques utilized in this dissertation are, at their core, laser spectroscopy techniques. The highly coherent and high intensity light emitted from modern lasers enables scientists to probe the energy states of materials with high resolution [57]. More recently, techniques such as atomic force microscopy, which came to fruition due to the advent of the laser, have been utilized to probe the many properties of QDs under various conditions [58, 59, 60]. Figure 4.1 shows a schematic of the laser spectroscopy setup used to probe the QD system.

In Fig. 4.1, the main points are the excitation and collection paths of the experimental setup. The excitation path begins by fiber coupling the output of a tunable laser to the PL platform. For the excitation of InAs QDs we use either a titanium sapphire (Ti-Saph) laser with the cavity in a bow tie configuration and a birefringent filter to tune the wavelength, or an external cavity tunable diode laser. These have a range of tunable wavelengths from 850 nm to 950 nm for the Ti-Saph laser and 890 nm to 980 nm for the diode laser. The laser light is first filtered by a short pass filter to remove as much of the low energy tail of the laser as possible. The light then passes through a polarizer which is used to select the excitation polarization for the experiment. A 90R:10T cube beamsplitter reflects 90% of the light onto a power meter for measurement. The other 10% of the light transmits toward the microscope objective upon which it is focused into the cryostation and onto the sample. This is an ideal choice because we generally have an abundance of laser power and can afford to sacrifice this power for the sake of maximizing collection of PL. The QDs within the sample will absorb the laser light and, upon relaxation, emit PL. This PL is collected by the microscope objective and directed back toward the 90R:10T beamsplitter. 90% of the collected PL is reflected toward a collection fiber. Along this path a 45R:55T pellicle beamsplitter is placed on a flip mount so that it can be easily removed from the setup during measurement. The light is split such that 45% is reflected toward an imaging camera for observation and the other 55% is sent toward the fiber collector. Before being collected by the fiber, the light passes through another polarizer and a long pass filter, both of which are used to remove as much of the excitation laser from the signal as possible. Finally, the light is focused into a triple stage spectrometer where it will be dispersed according to wavelength and focused onto a liquid nitrogen (LN) cooled charge coupled device (CCD)

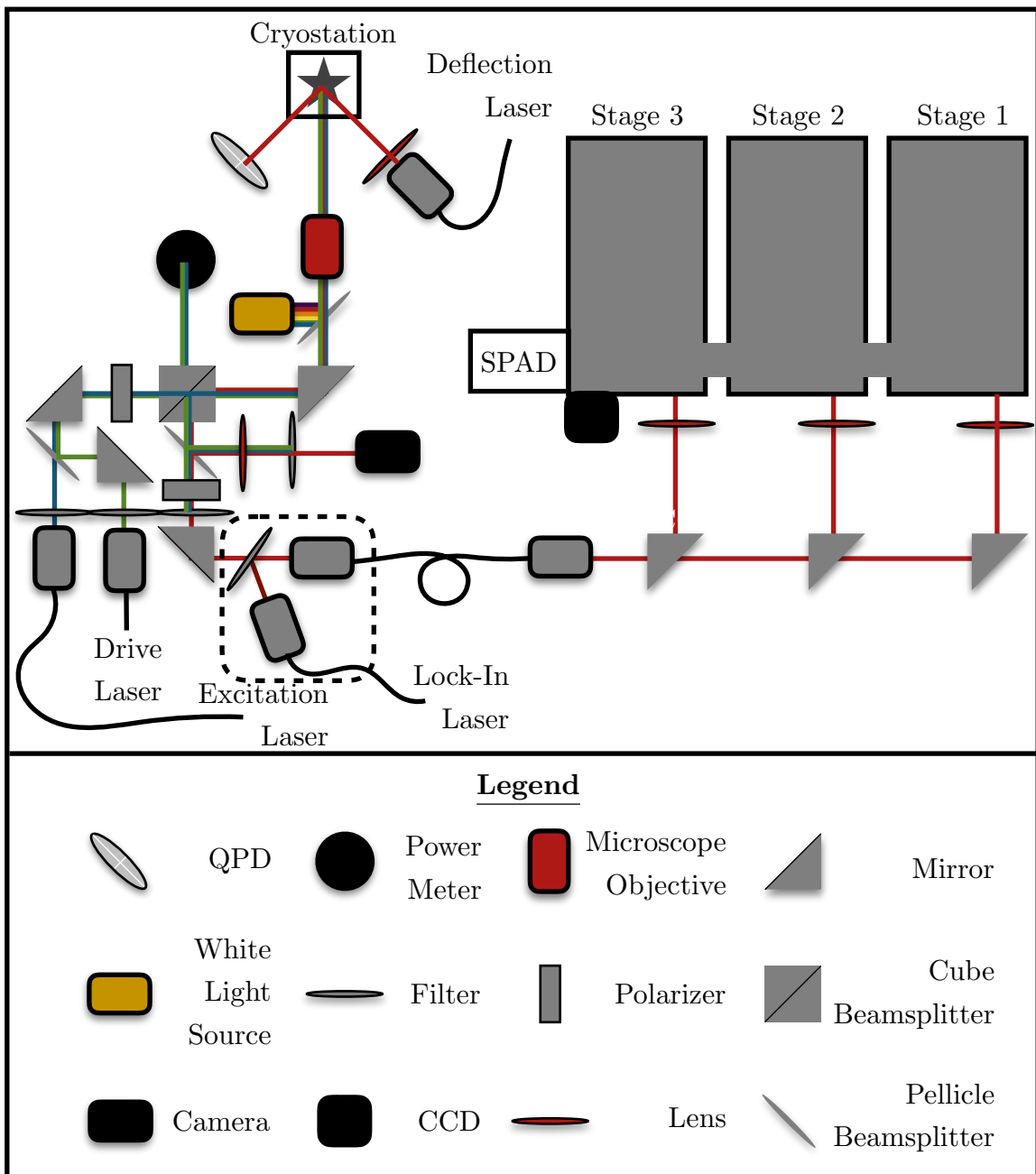


Figure 4.1: Combined experimental setup for laser spectroscopy, atomic force microscopy for static strain measurements, and optically induced mechanical resonance measurements. The setup has the option of focusing the PL into stage 1, 2, or 3 via the addition of flip mounts on the wedge mirrors. The dashed box is also represented in Fig. 4.13

camera. Having the flip-mounted beamsplitter before the PL collection fiber allows the experimenter to visually align a region of the sample with the excitation laser at the focal point of the microscope while simultaneously acquiring PL spectra which can be compared to previously recorded spectra for identification. The placement of this beamsplitter greatly enhances the abilities of the experimenter and provides more flexibility when locating QDs. Because the beamsplitter is on a flip-mount, once the experimenter identifies the correct position, both through visual evidence and spectral evidence, the beamsplitter may be flipped down and removed from the optical path, effectively doubling the amount of collected PL.

The filters and polarizers are utilized to remove as much stray laser light from the signal as possible. This is especially true for more resonant measurements. The closer the energy of the laser is to the energy of the desired transition, the more noise will exist in the signal. The removal of scattered laser light will be discussed in more detail during the latter portion of section 5 on high resolution phonon-assisted quasi-resonance fluorescence spectroscopy. A polarizer on the excitation side can also be used to selectively excite specific polarization states within the sample, and a polarizer on the detection side, when combined with a half wave plate or liquid crystal retarder, can be used to selectively detect emission of specific polarization.

## 4.1 Photoluminescence Spectroscopy

In a typical experiment, a continuous wave (CW) laser illuminates the sample, exciting an electron into a higher excited state. Upon relaxation to the ground state, the electron emits a photon that is directed toward a spectrometer by one or more optical elements. The spectrometer disperses the light that is sent through based on wavelength; once dispersed, the light is focused onto a detector. Since the typical acquisition time of a PL experiment is on the order of one billion times the radiative relaxation rate for a neutral exciton in a QD, the observed spectrum is the sum of many PL events. Because a spectrometer is a dispersive element, and excitation of the sample is typically non-resonant, PL exhibits better laser suppression compared to other spectroscopic techniques such as resonance fluorescence. The signal intensity, proportional to the number of photons striking the detector, can be plotted as a function of photon energy (or wavelength). Such a plot reveals information about the electronic energy level structure of the sample, as well as state lifetimes, and possibly even fine structure if the spectral resolution is high enough. Figure 4.2 shows PL spectra of an InAs QDM at varying excitation powers. Due to the difficulty of identifying all of the charge states using a single PL spectrum, a technique known as electric field dispersed PL is used to capture the changes in the optical spectrum as a function of applied electric field.



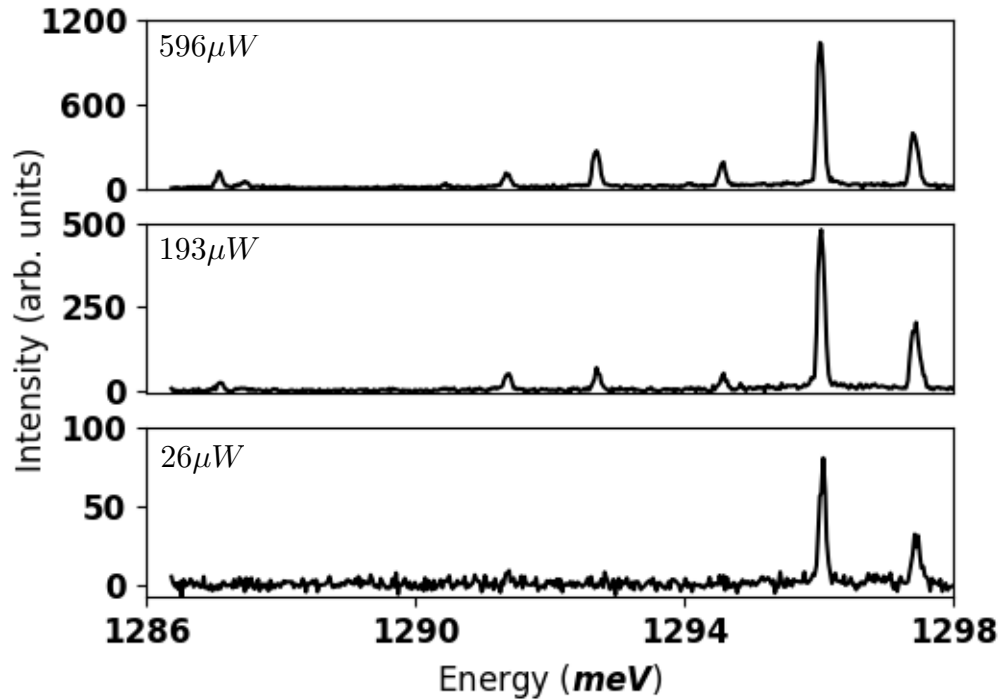


Figure 4.2: PL spectra of an InAs QDM at different excitation powers.

### Electric Field Dispersed Photoluminescence

Dispersing the photoluminescence spectrum of an InAs QDM as a function of applied electric field causes the electronic energy levels to experience a Stark shift. This shift in the energy levels can help identify indirect transitions within the QDM system. This is due to the larger dipole moment of indirect charge states when compared to direct charge states. The formula for the electric dipole of two charges, equal in magnitude but opposite in sign, is  $\vec{p} = q_e \vec{d}$  where  $q$  is the magnitude of the electric charge of the particles and  $\vec{d}$  is the displacement vector that points from the negative charge to the positive charge. In order to employ field-dispersed PL spectroscopy, one simply collects PL spectra of the QDM system at varying values of the applied electric field. To construct an informative electric field dispersed photoluminescence spectrum, often referred to as a bias map due to the applied electric field being a function of bias set by the experimenter, tens to hundreds of spectra are taken at varying bias values and stitched together. The resulting data is plotted as a colormap with the  $x$ -axis representing the bias, or electric field, and the  $y$ -axis representing the photoluminescence energy. The intensity is plotted along the  $z$ -axis and is represented by the color of the data point. It is common to find false color maps of electric field dispersed PL data such as the one in Fig. 4.3.

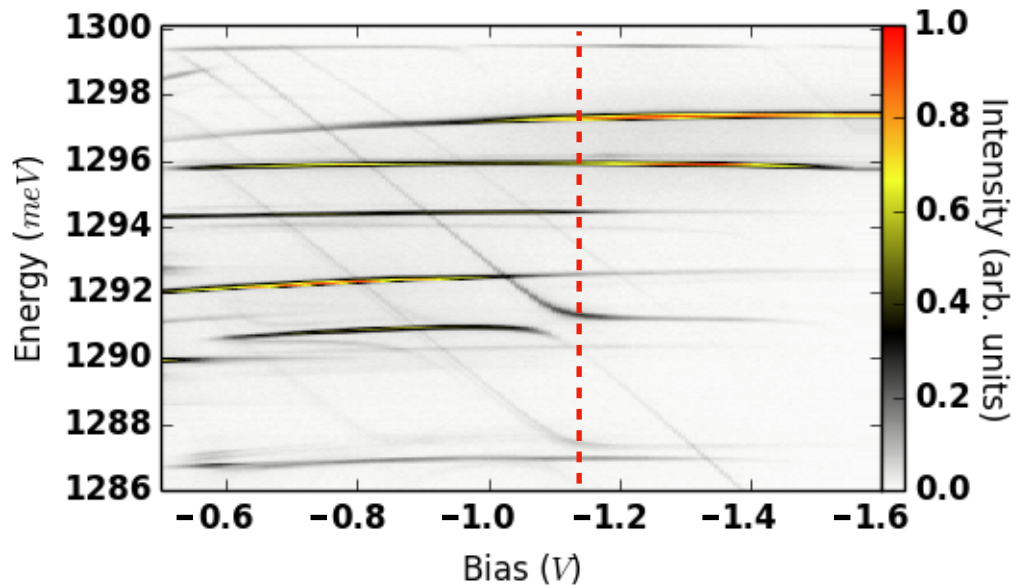


Figure 4.3: Electric field dispersed PL spectrum, also known as a bias map. Plotting the data in this way allows one to clearly discern the indirect transitions from the direct transitions. Patterns emerge from the data that are much more obvious to the eye than in the single spectrum case. The red dashed line indicates the bias at which the power series was taken in Fig. 4.2

### Photoluminescence Excitation Spectroscopy

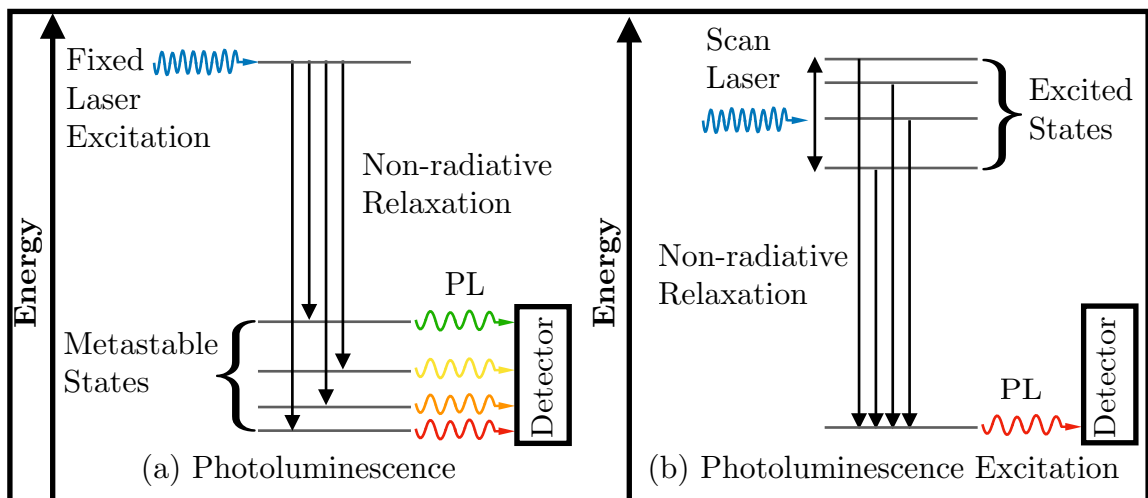


Figure 4.4: Schematic depicting the processes of (a) non-resonant PL spectroscopy and (b) PLE spectroscopy, as discussed in the main text.

Photoluminescence excitation (PLE) spectroscopy monitors the emission of light due to an electron's transition from the lowest energy excited state to the crystal ground state. This allows the excited state absorption spectrum to be measured via emission through the lowest energy transition. When the energy of a blue-detuned laser is scanned through the energies of the excited states, electrons from the valence band jump into these excited conduction band states. The excitation of an electron from the valence band to an excited state in the conduction band is most prominent when the laser energy is tuned into resonance with the electronic transition energy. Most of these excited electrons do not immediately relax and emit a photon; they first undergo non-radiative decay through which energy is lost by the generation of phonons. The electrons quickly lose enough energy to place them in the lowest energy excited state, at which time the electron radiatively relaxes back to the crystal ground state and emits a photon.

The experimental setup is very similar to that of regular PL. The only difference is that now the laser energy is scanned across a range of energies above the transition of interest. In order to investigate the excited state spectrum of the neutral exciton, one monitors neutral

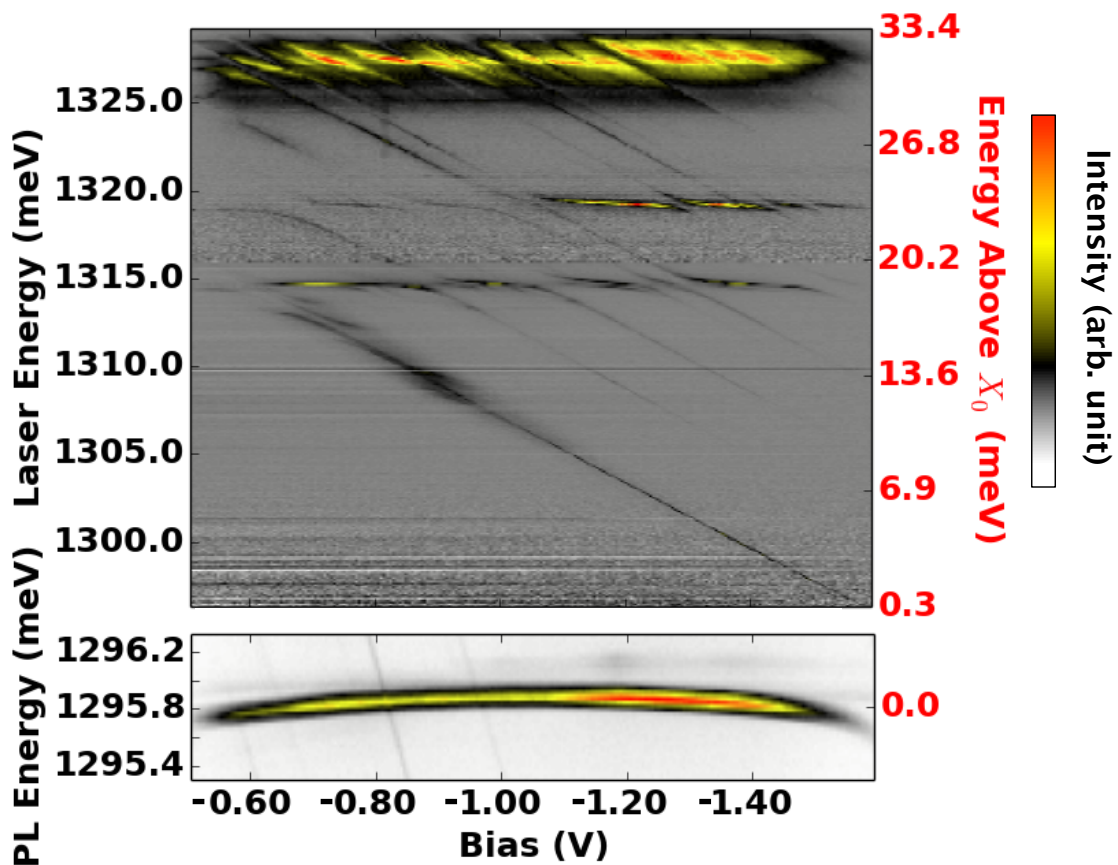


Figure 4.5: **(Top)** Electric field dispersed excited state absorption spectrum, also known as a PLE map, of the neutral exciton in an InAs QD. The PLE map shows the excited state absorption spectrum of the neutral exciton. **(Bottom)** Electric field dispersed PL spectrum of the neutral exciton.

exciton PL while scanning the energy of the excitation laser. Specifically, the laser should be set to energies higher than that of the neutral exciton to crystal ground state transition. Every time the laser energy is shifted, a PL spectrum of the neutral exciton is collected. In essence, a PLE map is the stitching together of PL as a function of excitation energy. Figure 4.4 shows a comparison of the two techniques of PL and PLE.

The technique of electric field dispersion can be used here as well to produce an electric field dispersed PLE map. Figure 4.5 shows an electric field dispersed PLE map of the neutral exciton in an InAs QD along with the sum of all of the electric field dispersed PL maps used to gather the data. The summed bias map is used as a reference point to compare energy differences between excited states. The PLE map can be used to gather information on the properties of the excited states such as the excited state energy level structure or indirectly measure the excited state lifetimes through the Heisenberg uncertainty principle.

## 4.2 Mechanically Inducing Static Strain in QDs

Special samples were grown to perform these experiments. Thin film membranes and tuning forks were patterned into the surface of the samples using electron beam lithography and an inductively coupled plasma etch. Hydrofluoric acid is used to undercut the mechanical resonators by etching away the  $\text{Al}_{0.7}\text{Ga}_{0.3}\text{As}$  layer providing free floating structures capable of undergoing static and dynamic strains; see Figs. 3.5, 3.6, and 3.8. The procedure for measuring the PL of statically strained QDs is as follows. First, a QD sample is placed onto an appropriate sample mount. In our case we utilize a 16-pin chip carrier (see Fig. 4.6). The chip carrier is then mounted to a stack of nano-positioning stages as shown in Fig. 4.7. This allows the sample to be translated in all three dimensions. After the sample is secured to the nano-positioning stages and placed in the cryostation an extra mount is added to hold an atomic force microscopy (AFM) probe above the sample (see Fig. 4.7). The probe is held stationary and the nano-positioners are used to raise the sample into the probe for the purpose of inducing strain in the material. All of this resides inside of the cryostation and is cooled down to around 5 K. Outside of the cryostation, an optical microscope is focused onto the AFM probe. Once the probe is in focus, a laser beam at  $45^\circ$  incidence is brought into focus on the tip of the probe. The reflected beam is collected by a Position Sensitive



Figure 4.6: 16-pin dual in-line package chip carrier for QD samples.

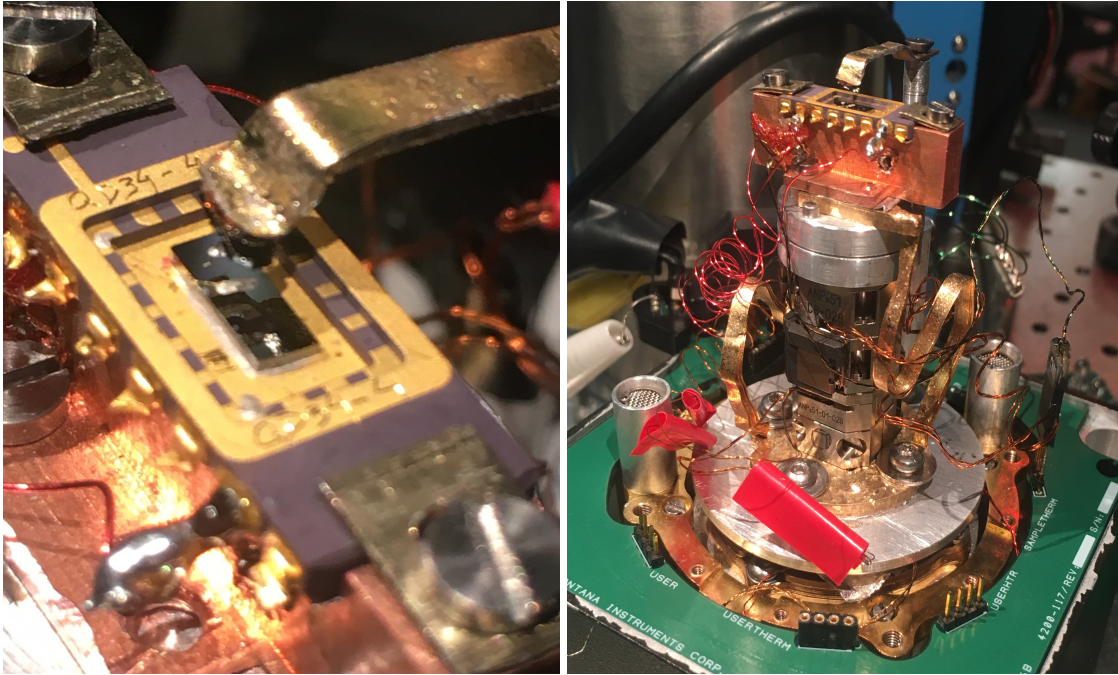


Figure 4.7: **(Left)** Closeup image of a QDM sample in a 16-pin chip header, attached to the nano-positioning stages, mounted inside of the cryostat, and situated underneath the AFM probe holder. **(Right)** Stack of three nano-positioning stages for translation in  $x$ ,  $y$ , and  $z$  dimensions. The gold ribbons connecting the top plate to the base plate provide thermal conductivity between the sample and the cold finger of the cryostat.

Detector (PSD) . This type of detector is sensitive to small displacements of the reflected laser beam caused by nanometer-scale movement at the AFM probe. Alignment and calibration of the setup is performed at this time. For more information on the calibration of the setup see Appendix B.

Once the setup has been aligned and calibrated, the sample can be raised into the AFM probe. At this point, it is necessary to lower the sample a few microns so that the sample can be translated without fear of scratching the surface to perform PL on individual membrane structures. The microscope needs to be refocused on the surface of the sample to locate membranes containing QDs for further study. It is important to keep the lateral position of the microscope objective situated directly above the tip of the AFM probe. Typical PL techniques are utilized at this point to locate a QD warranting further investigation. Once a QD with promising properties has been located, the sample is raised toward the AFM probe until first contact is made (see Fig. 4.8). Upon viewing the image, small adjustments to the position can be made to center the membrane, within which the QD is located, underneath the tip of the AFM probe. The full setup has been aligned at this point and PL spectra can be recorded with the sample pressed into the AFM probe at varying amounts.

Viewing the bottom right corner of Fig. 4.8, one can see the physical damage that has occurred to the membranes due to penetration of the AFM probe tip with the thin film membranes. It is our hypothesis that the damage may be caused by AFM probes whose

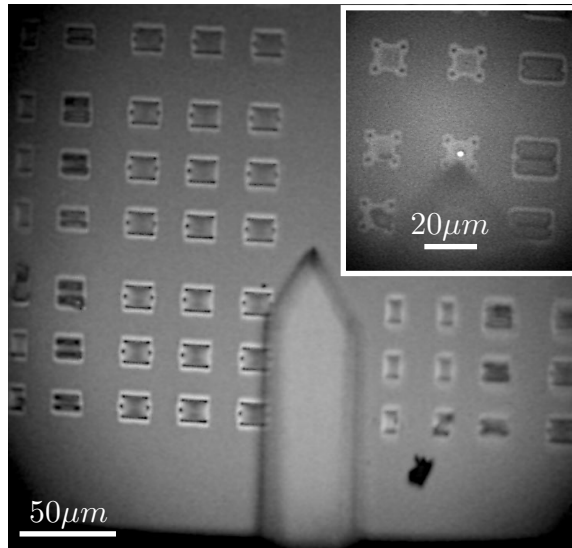


Figure 4.8: Microscopy image of the AFM probe situated just above the sample surface. The inset of the figure shows the tip of the AFM probe aligned with the center of a membrane.

stiffness is much greater than that of the membranes. Other possible reasons for the damage are electrostatic discharge or AFM probe tips whose aspect ratio is sharp enough to pierce through the membranes. For this reason, electron beam deposition (EBD) tips were specially ordered. These probes possess a  $1 \mu\text{m}$  diameter sphere that has been deposited on the tip. This provides a much smoother contact between the AFM probe and the sample membrane and also removes sharp edges which promote coronal discharges of static electricity.

### 4.3 Optically Inducing Dynamic Strain in QDs

A non-contact optical technique has been developed that can drive the mechanical structures at their resonance frequencies. Below bandgap excitation, at the contact point of a microcantilever, can induce vibrations in the structure. In coated cantilevers it is believed that the mechanism behind the driving is photothermal excitation [61, 62]. This is due to differences in the thermal expansion properties of the dissimilar materials. However, not much research has been done to understand this phenomenon in structures that are mostly monolithic. To measure this effect, below bandgap lasers are focused onto the surface of the cantilever. One laser, henceforth called the drive laser, is focused onto the contact point of the microcantilever and the bulk material for the purpose of driving the mechanical motion. The other laser, henceforth called the signal laser, is focused on the free end of the microcantilever to monitor the spot that will experience the largest amplitude of oscillation. The positioning of these lasers is shown schematically in Fig. 4.9.

A frequency generator is used to generate the signal responsible for the modulating

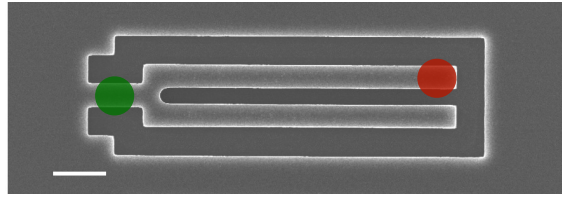


Figure 4.9: SEM image of a micro tuning fork with superimposed beam spots. The drive laser (green) is focused onto the base of the tuning fork while the signal laser (red) is focused on one of the tines at the free end of the tuning fork. The white scale bar represents  $2 \mu\text{m}$ .

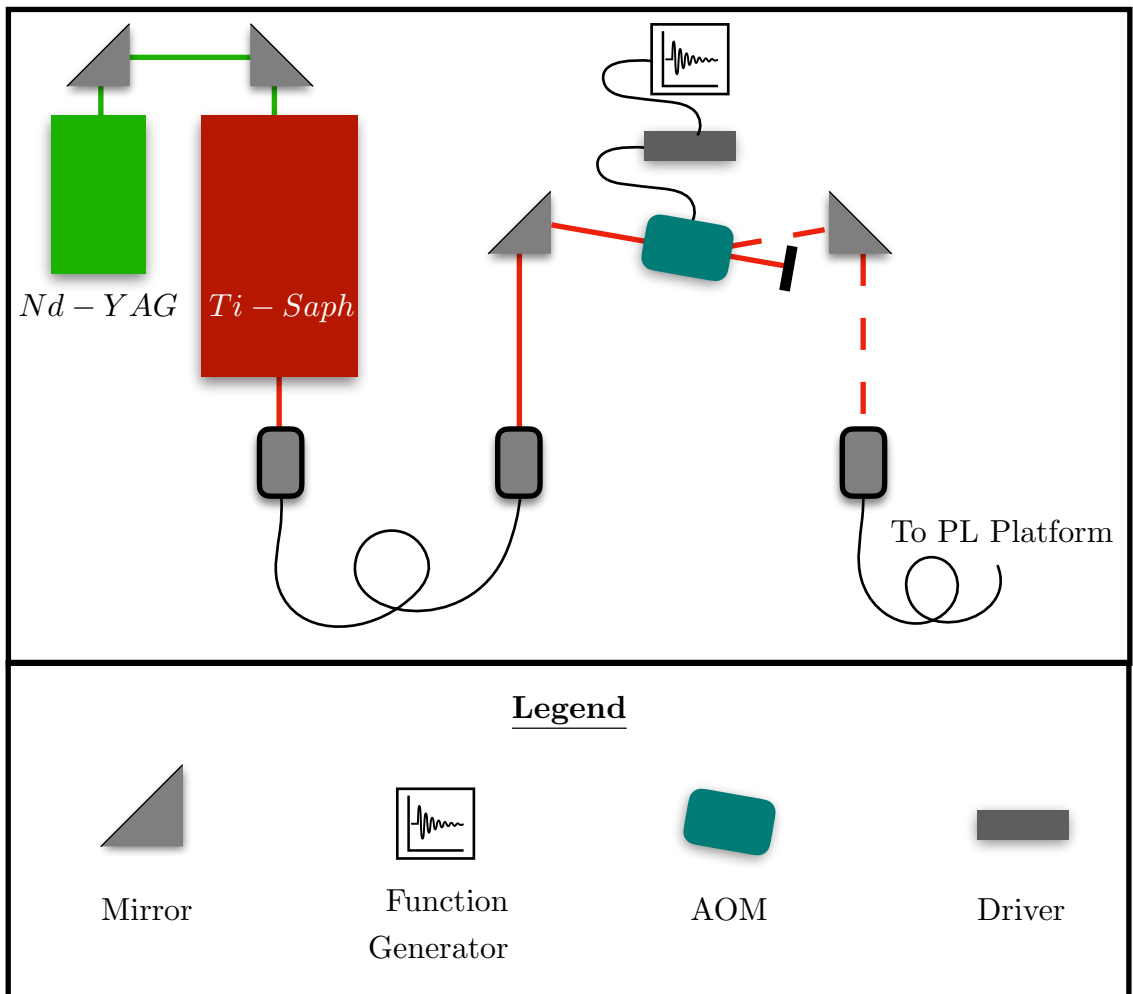


Figure 4.10: Schematic of the AOM used to amplitude modulate the drive laser.

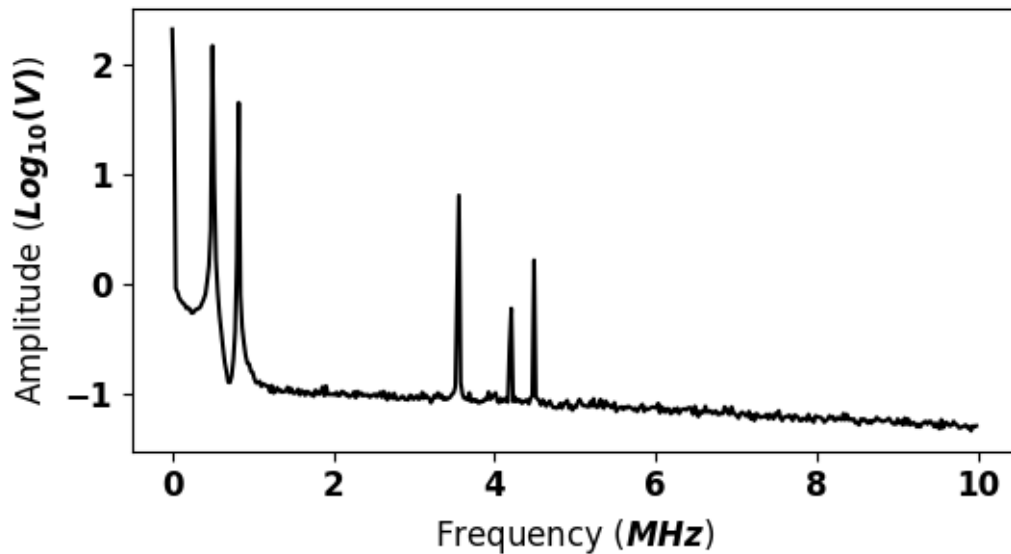


Figure 4.11: Mechanical resonance spectrum of a microcantilever. For the purposes of the following experiments, only the fundamental mode is used.

the drive laser. The output of the frequency generator connects to the modulation input of an acousto-optic modulator (AOM) which is used to amplitude modulate the drive laser. A schematic of this setup is shown in Fig. 4.10. The reflection of the signal laser is collected by the same fiber that is used to collect the PL in other experiments, but rather than being focused into the spectrometer it is focused onto an avalanche photodiode (APD). The output of the APD is connected to a spectrum analyzer for analysis in the frequency domain. As the spectrum analyzer sweeps through a range of frequencies while monitoring the APD signal, the function generator quickly sweeps the AOM through the same range of frequencies. Typically the spectrum analyzer is set to scan over a 10 MHz frequency range in a 10 s period while the frequency generator is set to sweep the same frequency range every 10 ms.

The reflection of the signal laser experiences optical interference due to reflection off of two surfaces. The reflection from the cantilever surface and the reflection from the substrate. The interference signal changes in intensity most drastically when the microcantilever is excited by a resonantly driven laser beam, and the APD detects these changes. This method is well suited for determining the mechanical resonance spectrum of the structure (see Fig. 4.11) prior to searching for a QD that has ideal properties.

Once the mechanical resonance spectrum has been obtained, the interference laser can be used as an excitation laser and PL is performed at the base of the cantilever where it connects to the bulk material. With the drive laser off, a QD with ideal emission properties is identified. The signal from the QD of interest is improved by small adjustments to the optical alignment. The drive laser is turned back on and is allowed to sweep through a range of frequencies centered on the mechanical resonance frequency. Meanwhile, PL is collected at each frequency. With this data, a mechanical resonance frequency dispersed PL map showing PL intensity as a function of emission energy and mechanical drive frequency



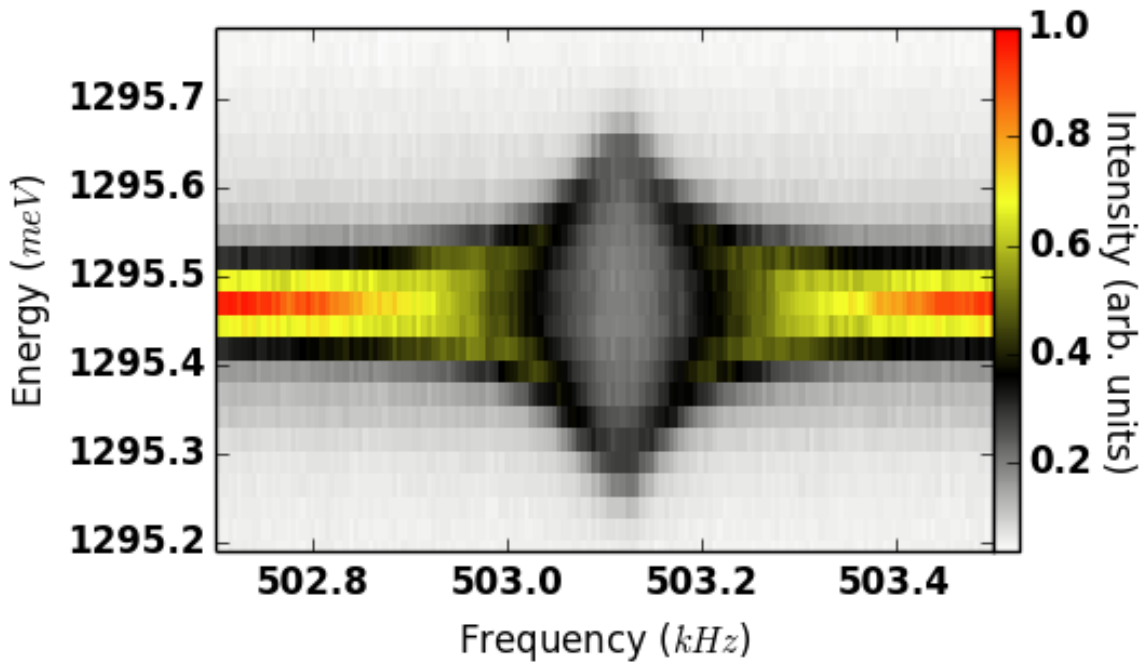


Figure 4.12: PL map showing the linewidth broadening of the QD emission at the mechanical resonance of the microcantilever.

can be generated. These maps typically show a broadening of the emission peak near the mechanical resonance (see Fig. 4.12).

#### 4.4 Fabry-Perot Interferometer and Resolution Enhancement

A typical PL experiment will direct the emission from a sample into a spectrometer to be spectrally dispersed before detection. The resolution with this setup is limited by the focal length of the spectrometer, the groove density of the diffraction grating, the entrance slit width, and either the exit slit width or the pixel width, depending on the type of detector. For a 750 mm focal length spectrometer with an 1100 groove/mm diffraction grating, 20  $\mu\text{m}$  entrance slit width, a LN cooled CCD camera with a 20  $\mu\text{m}$  pixel width, and monitoring a 950 nm (1305 meV) center wavelength, the resolution is 0.02 nm (27.5  $\mu\text{eV}$ ). However, this resolution is per pixel on the CCD camera and generally even the sharpest atomic transitions will have a width of 3 pixels due to instrument constraints. This results in a spectral resolution of 0.06 nm (82.5  $\mu\text{eV}$ ).

This resolution can be enhanced by first passing the PL through a Fabry-Perot (FP) interferometer. In the experiments detailed in this dissertation, we use a FP cavity of length  $d = 1.4$  mm with a free spectral range of 0.322 nm (443  $\mu\text{eV}$ ) and a resolution of 0.006 nm (8.25  $\mu\text{eV}$ ). The experimental method which utilizes this order of magnitude improvement in resolution is described as follows. A 980 nm (1265 meV) locking laser is combined

with the PL from the sample prior to entering the FP interferometer. This is shown in the dashed box in Figs. 4.1 and 4.13. The locking laser is an external cavity diode laser whose frequency is modulated by a piezoelectrically controlled cavity at 1 kHz with an amplitude of a few  $\mu\text{eV}$ . The frequency modulated locking laser can only transmit through the FP when its wavelength is resonant with the interferometer. Through this mechanism, the frequency modulated signal is turned into an amplitude modulated signal, which in turn is monitored by a lock-in amplifier. After exiting the FP, the locking laser is picked off with a 1000 nm short pass filter that is rotated away from normal incidence so that its cutoff wavelength is just below the 980 nm locking laser. This maximizes both the reflection of the locking laser and the transmission of the PL through the short pass filter. The PL, minus the locking laser, is collected by a fiber optic cable and directed to the entrance slit of the spectrometer, while the locking laser is collected by a separate fiber optic cable and sent to an APD. The output signal of the APD is monitored by a lock-in amplifier that is triggered by a reference from the locking laser. If the length of the FP is shifted by half a wavelength, the original wavelength can transmit through a higher mode of the FP but shifted in phase by  $180^\circ$ . The phase of the lock-in amplifier is set to make the X channel positive when the cavity is red detuned and negative when the cavity is blue-detuned from the locking laser. When the locking laser and the FP are resonant, the X channel outputs zero. Therefore, the X channel can act as an error signal to the resonance of the cavity and the locking laser. An auxiliary output on the lock-in amplifier is used to control the voltage applied to the range generator which controls the piezoelectric transducers modulating the length of the FP interferometer. If the X channel is positive, the auxiliary output of the lock-in amplifier voltage controlling the FP is increased, and if the X channel is negative, the voltage to the FP is decreased. A LabView VI is used to control a feedback loop that keeps the X channel at zero, thus locking the FP to the locking laser. As the laser is scanned, the FP follows along as long as there are not any excessive jumps in the tuning that cause the system to lose the lock. A schematic of this setup is described in Fig. 4.13

With this system in place, the PL that enters the spectrometer has already been filtered by the FP interferometer to contain only a  $9 \mu\text{eV}$  bandpass of light. Due to the nature of the FP interferometer, multiple modes of allowable transmission make it through to the spectrometer, each with a bandpass of  $9 \mu\text{eV}$ . The modes are spaced apart by the free spectral range of the FP and can be separated by the dispersion of the spectrometer. Since the free spectral range of the FP is  $0.322 \text{ nm}$  ( $443 \mu\text{eV}$ ) and the spectrometer has a dispersion of  $27.5 \mu\text{eV}/\text{pixel}$  on the CCD camera, there exist approximately 16 modes of transmitted light at the camera. If a single channel detector is used instead, the exit slits can be narrowed to minimize the number of modes at the detector to one. Figure 4.14 shows the resolution enhancement of the PL from the negative trion state  $|X^{-1}\rangle$  of a single QD through a FP cavity enhanced experiment versus a typical spectroscopy experiment. For single channel experiments, a single photon avalanche diode (SPAD) is used as the detector. During a single channel measurement the FP is scanned through the bandpass of the spectrometer until the light has dispersed too much to exit the spectrometer. At this point, the diffraction grating of the spectrometer is rotated so that the light transmitted from the FP is once again at the beginning of the spectrometer's bandpass at the exit slit. This process can be repeated until the FP reaches the end of its free spectral range, at which point the FP is returned to

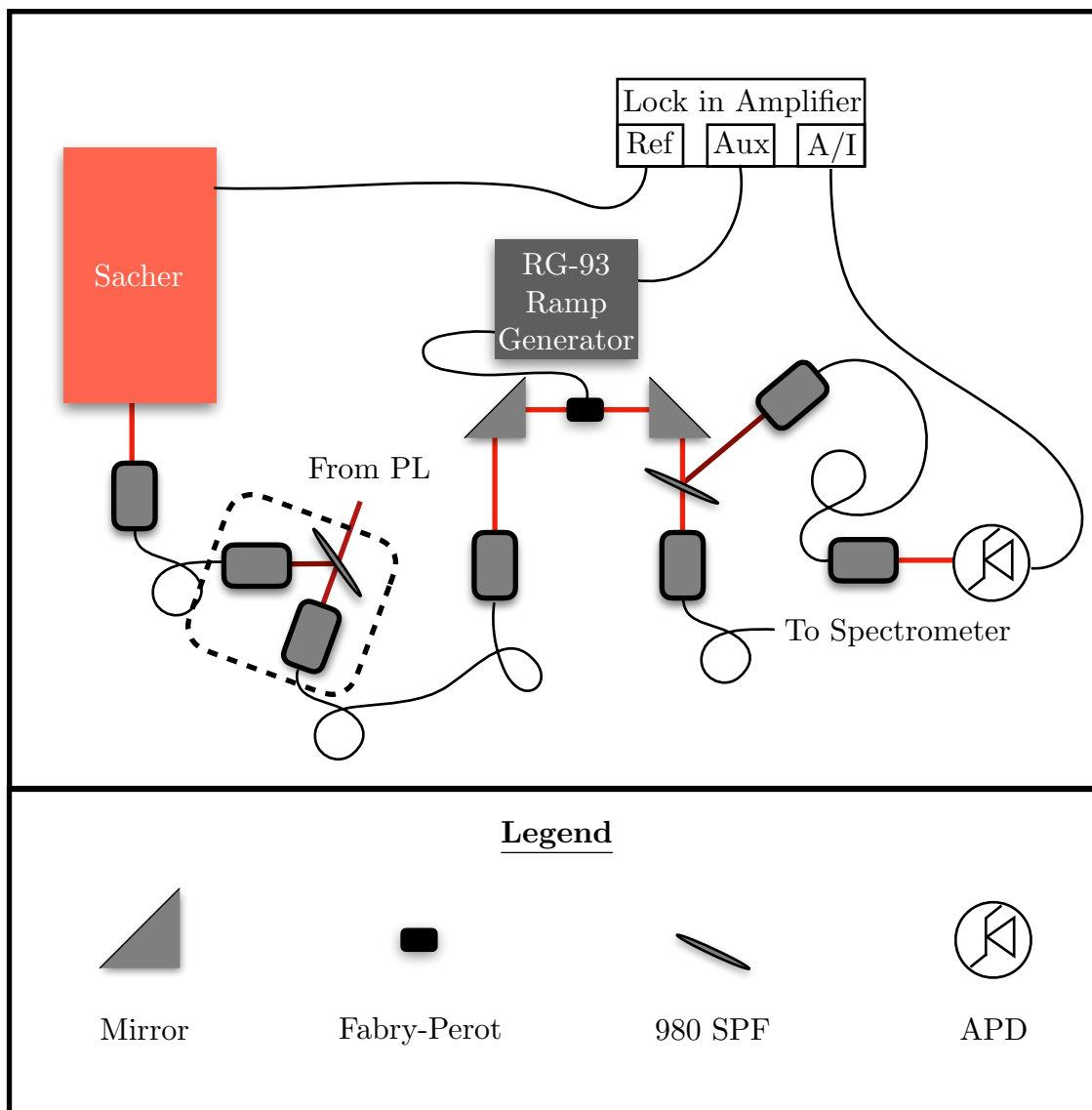


Figure 4.13: Schematic of the Fabry-Perot laser locking technique. The purpose of this technique is to control the thermal drift of the FP over time so that high resolution PL spectra can be obtained with little-to-no drift noise. The dashed box is a section of the PL platform depicted in Fig. 4.1.

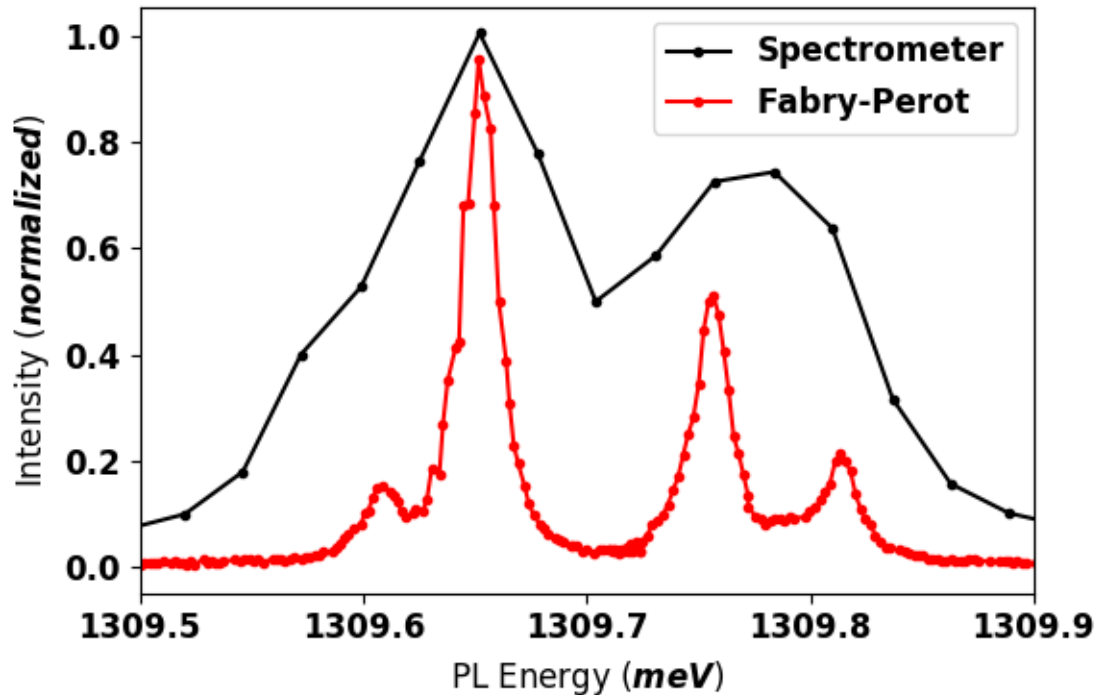


Figure 4.14: Comparison of the signals captured by a typical spectroscopy experiment (black) and a FP resolution enhanced spectroscopy experiment (red).

its original length to allow the same wavelength through, but at a higher mode of the FP. This completes one full cycle of scanning the combined FP interferometer and spectrometer system and can be repeated as many times as necessary. In our experiments, the signal of interest typically does not span more than  $0.291 \text{ nm}$  ( $400 \mu\text{eV}$ ) and does not require iterating the process described above more than once.

## 4.5 Time-Correlated Single Photon Counting

Time correlated single photon counting (TCSPC) is a technique used to measure high frequency and low intensity events such as the emission from individual QDs. Probing the temporal dynamics of a single emitter such as a QD yields insights into the decay lifetimes of specific quantum states. Rather than a typical time resolved experiment which will measure the emission intensity as a function of time, the TCSPC technique measures the time lapsed between an excitation pulse, typically an ultrafast laser, and the emission of a single photon from a quantum emitter. Figure 4.15 shows a schematic of the detection mechanism [63]. The device will accumulate this data over a series of emission events and record a histogram relating the number of photons emitted within specific time bins relative to the laser pulse (see Fig. 4.16) [64].

The advantage of this technique lends itself to the difficult nature of observing quan-

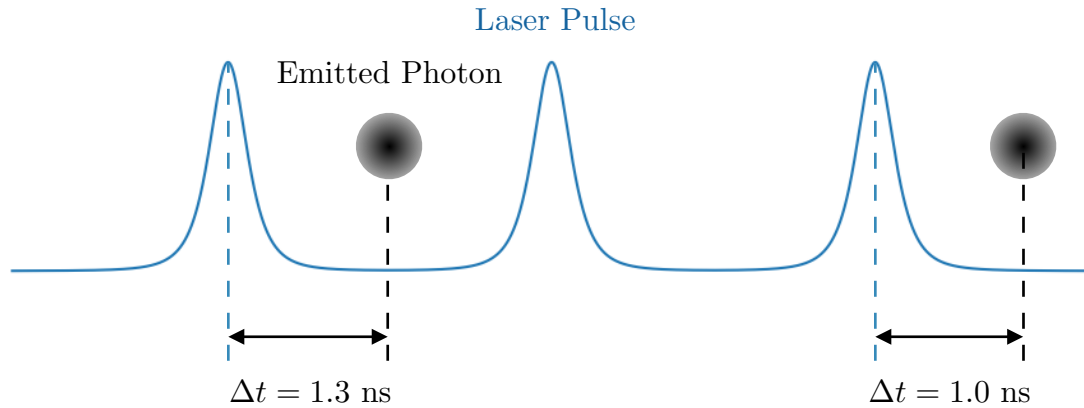


Figure 4.15: Measurement schematic for the TCSPC technique. A laser pulse generates an exciton in a QD which quickly recombines and emits a photon. The photon is tagged by the electronics in the TCSPC module. The detection rate should be 20 to 100 times less than the excitation rate and should therefore include cycles that contain no emitted photons. The situation of a zero decay cycle is depicted as the second laser pulse in the three pulse train.

tum events in general. It is not a simple task to devise an experiment in which a single cycle of excitation and emission can be recorded by an electronic detector. First, the time scale of QD emission is on the order of hundreds of picoseconds to a few nanoseconds, much faster than the temporal resolution of most optical detectors. Second, the light emitted by a QD during an excitation and emission cycle would be a single photon, much too low of a signal to be sampled by any analog device in a reliable manner. By continuing the data collection across many excitation and emission cycles, the TCSPC technique is able to overcome both of these issues.

The caveat to this technique is that the light levels must be kept low enough so that multiple photon events rarely occur during a single excitation and emission cycle. This requirement is so strict that it is recommended to attenuate the emission before striking the detector such that a photon is only detected 1 out of every 20 to 100 cycles. In other words, the count rate at the detector should be 1 to 5% of the excitation rate.

The experiments conducted in this dissertation utilize the TCSPC technique to capture the emission energy of individual spin states as a function of the period of a mechanical resonator. As described in previous sections, a QD is embedded in a mechanical resonator which is then driven optically by an amplitude modulated laser. The TCSPC module is triggered by the frequency generator which controls the AOM that modulates the drive laser. This synchronizes the mechanical motion to the TCSPC module. PL from the QDs, which are experiencing strain due to the mechanical motion, is detected by the SPAD then given a time tag and accumulated by the TCSPC module. This provides data on the optical shift due to the strain caused by the mechanical motion and allows us to correlate the shifts in individual spin states at each moment in time. This experiment will be discussed in more detail in ch. 5.2.

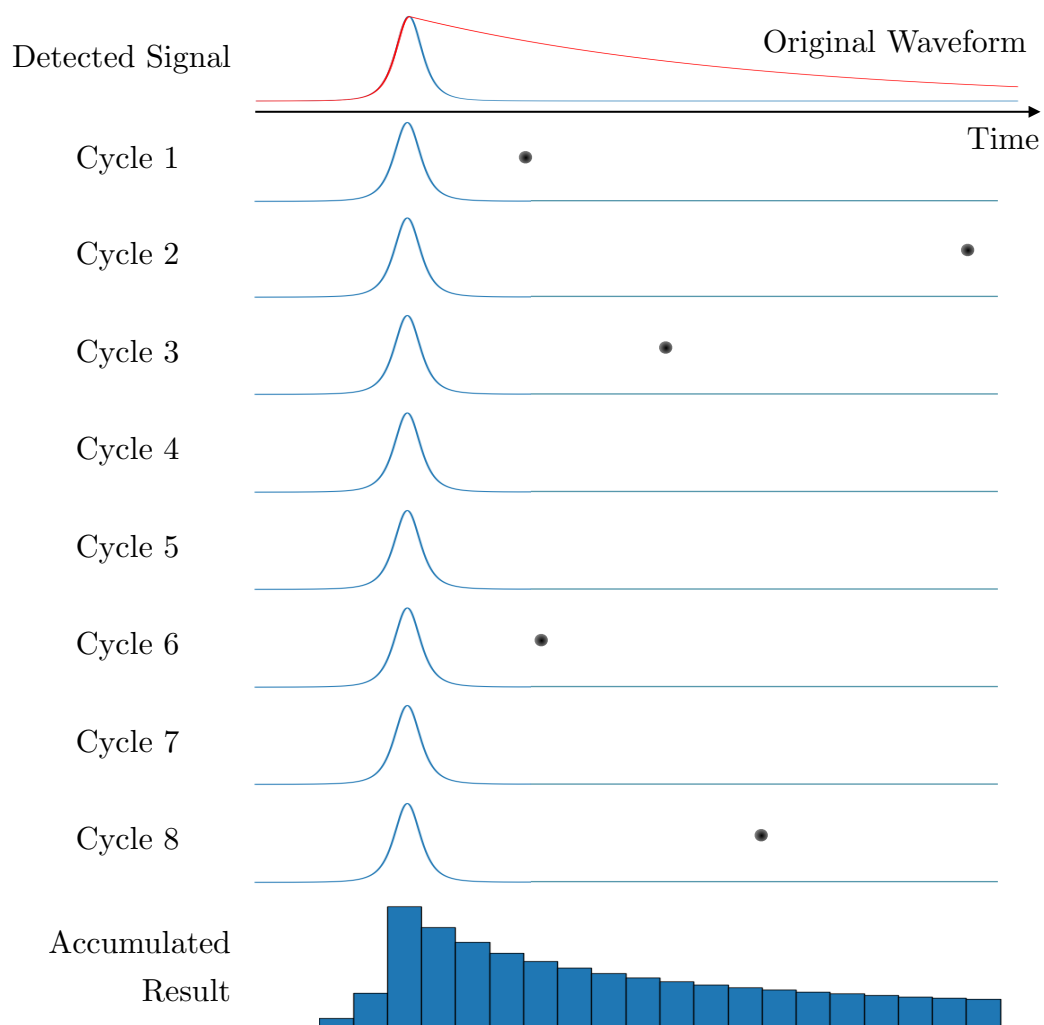


Figure 4.16: Schematic showing eight excitation and emission cycles of a TCSPC experiment. The original waveform is plotted at the top and the individual cycles collect the random events of photon emission. At the bottom is the final histogram of recorded photon collection times relative to the laser pulse.

## Chapter 5

# High Resolution Phonon-Assisted Quasi-Resonance Fluorescence Spectroscopy

A video walkthrough of the following technique as well as a full text of the associated article can be viewed at the Journal of Visualized Experiments [65]. This phonon-assisted spectroscopy technique provides a system with the effective resolution of a resonant measurement, which is advantageous because it affords such resolution to a system that otherwise would be dispersion limited. Similar to Raman spectroscopy, this technique utilizes the phonon sidebands of a quantum state to analyze its properties. It is also similar to the technique of PLE because you are passing an energy state and a laser through one another and monitoring the emission at a lower energy. The basic principle of the technique is to sweep the energy of the excitation source through resonance with the ground state transition of a QD and observe the emission from either the tail of the acoustic phonon resonance or the  $-1$  LO phonon satellite.

This technique can be achieved by either holding the energy of a transition fixed and scanning the laser through the transition, or by holding the energy of the laser fixed and scanning the transition energy through the laser. Tuning the transition energy across the laser can be performed in two ways. By changing the sample temperature, the transition energy of the QD is shifted according to Varshni's law, causing it to pass through the laser energy [66]. Alternatively, by applying an electric field to the sample, the exciton's transition energy Stark shifts through the laser energy [67]. This latter technique is most useful for indirect transitions where there is a large dipole moment allowing stronger Stark shifts. Examples of the different methods of this technique are shown in Figures 5.1 - 5.4 and are described in detail in the following sections.

The main technique utilizes dielectric short pass and long pass filters, which are placed in the excitation and detection paths respectively. These filters provide a versatile feature in that their cutoff frequencies blueshift when the angle of incidence is incremented away from normal and they are also useful as di-chromatic beam splitters. Therefore, it is possible to rotate the short pass filter in the excitation path to remove as much of the low energy tail of the laser as possible. Similarly, it is possible to rotate the long pass filter in the detection

path to achieve the same goal. The rotation of these filters is key to removing the noise caused by stray laser light. Once the rotation of the filters has been optimally aligned, a signal should be present on the screen. This is the -1LO phonon satellite of the ground state transition. The signal present is due to resonant excitation of the ground state transition followed by emission of an LO phonon and subsequently emission of a photon. At this point, one of the three methods of tuning the transition and laser energy through each other can be employed.

This technique is a convenient method for investigating features on small energy scales such as homogenous linewidths, fine structure splittings, or anisotropic e-h exchange splittings. The convenience comes from the technique being applicable to a standard PL spectroscopy setup. Besides the dielectric filters, no additional changes to the optical path must be made prior to performing this technique. Additionally, due to the nature of phonons not carrying any spin information, the optical emission collected by this technique maintains its spin polarity. As an example the neutral exciton ground state of a QD has four degenerate spin states (see Fig. 2.9). The four-fold degeneracy is lifted when the two spin 2 (dark) states separate from the two spin 1 (bright) states due to isotropic exchange. The degeneracy of the two bright states is further lifted due to the in-plane asymmetry of the QD, which is inherent to the growth process. The splitting of these two bright states causes the neutral exciton to have a doublet whose individual peaks can be determined by its spin configuration. Anisotropic Exchange Splittings (AESs) in these samples can range from 0 - 30  $\mu\text{eV}$ . Due to the spin-free nature of phonons, a properly polarized detection path can yield information about an isolated transition. Therefore, this technique can be utilized to reliably read out stored polarization information with high resolution.

## 5.1 Laser Resolved

When scanning a tunable diode laser across the transition, the resolution is set by either the energetic step size of the laser or the laser linewidth itself, whichever is larger [6, 52, 68]. To fully resolve the excited state spectrum, the laser's energetic step size must be smaller than the linewidth of the emission.

Figure 5.1 shows a comparison of three different PL techniques. The **(Blue)** curve depicts a spectrum acquired with a single stage spectrometer and CCD camera. The resolution in this case is determined by the spectrometer focal length, diffraction grating groove density, entrance slit width, and CCD pixel width. A spectral resolution of 26  $\mu\text{eV}$  per pixel results in only a single peak being discernible using this technique. The **(Green)** curve was acquired with a triple stage spectrometer and CCD camera. In this case the resolution is 10  $\mu\text{eV}$  per pixel due to the longer travel length over which light can disperse; however it is still limited by the diffraction gratings, the entrance slit, and the CCD pixel width. The method has just enough resolution to show signs of a doublet, but the spectral feature is still not fully resolved. The **(Red)** curve displays the  $-1$  LO phonon satellite, which was monitored while the laser was scanned through the ground state transition energy. Because the resolution of this method does not rely on the dispersion of light, but rather the step size of the laser  $\sim 1.8 \mu\text{eV}$ , it is able to capture the individual peaks through a single spectrometer.



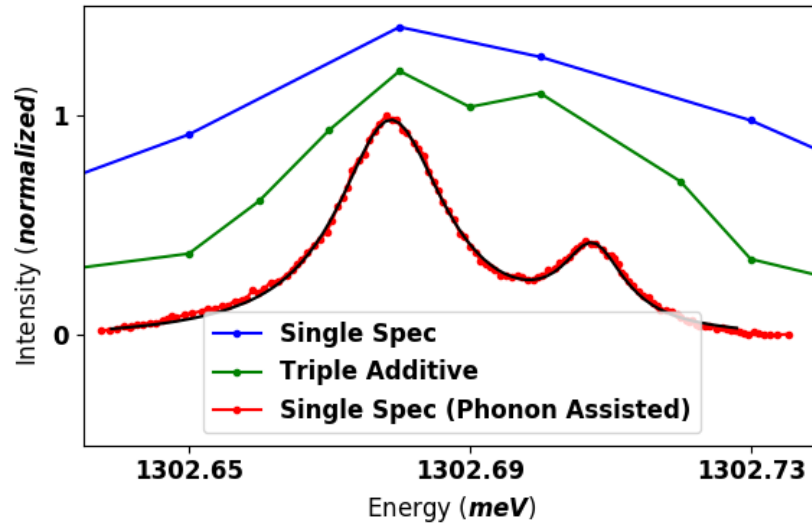


Figure 5.1: Resolution comparison of three different PL techniques [65].

A mathematical fit to the red curve with a double Lorentzian function (**Black**) provides an anisotropic e-h exchange splitting of  $23.3 \pm 0.1 \mu\text{eV}$ .

Figure 5.2 shows a bias map of the anisotropic exchange splitting collected using the laser resolved method of high resolution phonon-assisted quasi-resonance fluorescence spectroscopy. The ground state of the neutral exciton is swept through a fixed laser energy by varying the voltage applied in 2 mV increments, creating a single horizontal slice of the

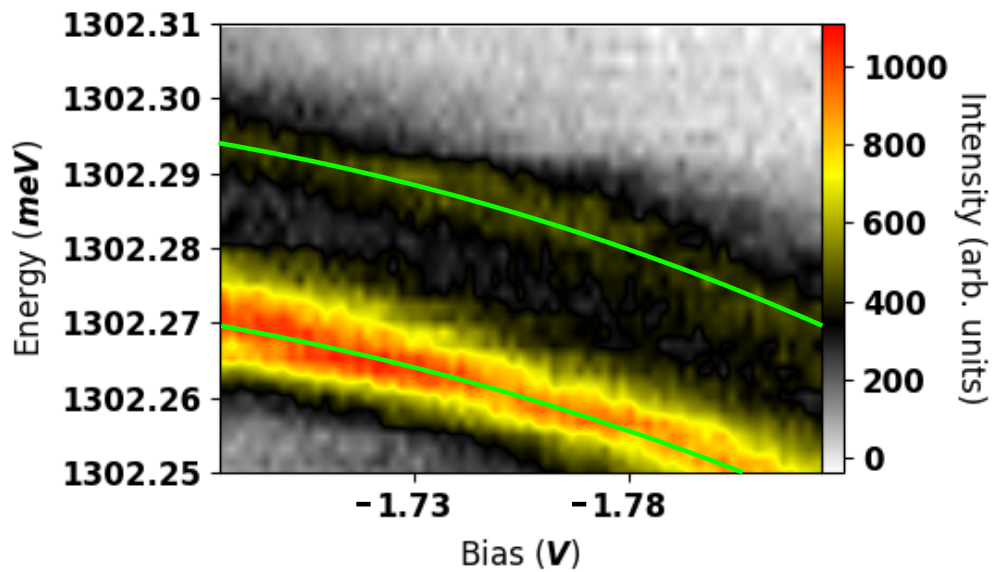


Figure 5.2: Bias map of the anisotropic exchange splitting collected by high resolution phonon-assisted quasi-resonance fluorescence spectroscopy [65].

map. The laser energy is then incremented by  $1.7 \mu\text{eV}$  and the experiment is repeated. This happens 37 times to cover the energy range shown. The average of the e-h exchange energy (the difference between the two green curves) is  $25.4 \pm 0.8 \mu\text{eV}$  over this bias region.

## 5.2 Temperature Resolved

The resolution of this method is determined by both the slope of the curve relating the energy of the transition to the temperature of the sample and the precision with which one can tune the temperature of the sample. The procedure is performed by first identifying the ground state transition of a QD through non-resonant PL. Once the ground state has been identified, the excitation laser is centered on the transition energy. This is accomplished quite easily by placing a cursor on the spectrum where the ground state transition shows up

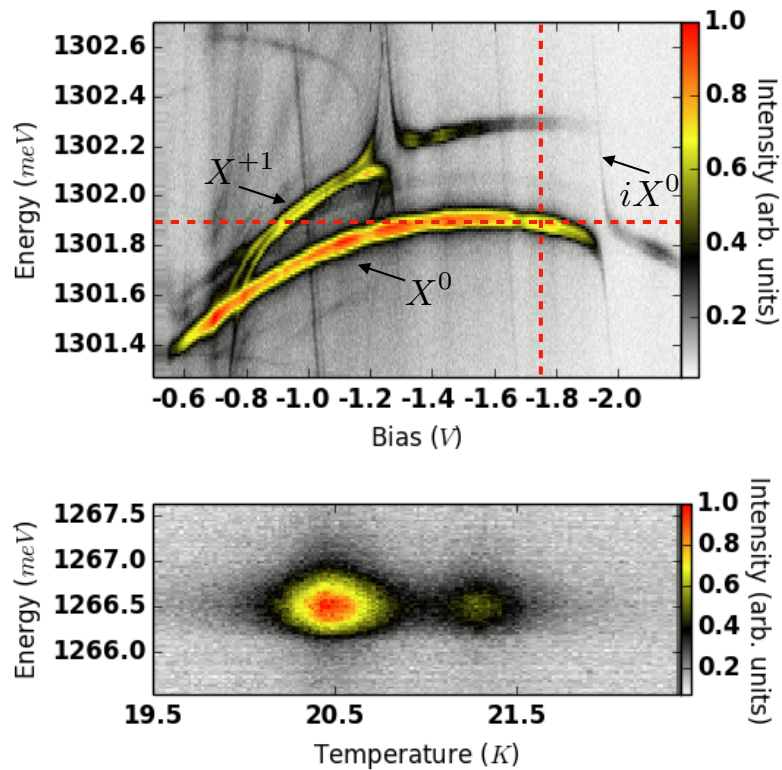


Figure 5.3: **(Top)** Bias map acquired by triple additive electric field dispersed PL spectroscopy under non-resonant excitation. Emission from the neutral exciton ( $X^0$ ), indirect exciton ( $iX^0$ ), and the positive trion ( $X^{+1}$ ) are identified. The vertical red dashed line at  $-1.75 \text{ V}$  represents the bias applied to the sample for the phonon-assisted technique, and the horizontal red dashed line is the energy at which the laser was held constant. **(Bottom)** High resolution phonon-assisted quasi-resonance fluorescence spectroscopy at the -1 phonon satellite of the neutral exciton. The transition energy of the exciton was tuned through a fixed laser energy of  $1301.9 \text{ meV}$  ( $952.4 \text{ nm}$ ) by stepping the temperature. The -1 LO phonon satellites appear around  $36 \text{ meV}$  below the zero phonon lines [65].

and then tuning the diode laser until the peak overlaps with the cursor. At this point, the center wavelength of the spectrometer is red shifted from the ground-state transition energy by the equivalent of 1 LO phonon.

### 5.3 Bias Resolved

Figure 5.4 shows the results of stepping the bias of the neutral exciton to sweep the resonance through the excitation laser. In this method, the resolution is set by the slope of the curve relating the energy of the transition to the applied electric field and the precision with which one can tune the applied electric field. The anisotropic electron hole exchange energy can be clearly discerned from this treatment as well as the lifetime-limited linewidths of the transitions ( $8 \mu\text{eV}$  and  $4 \mu\text{eV}$  respectively).

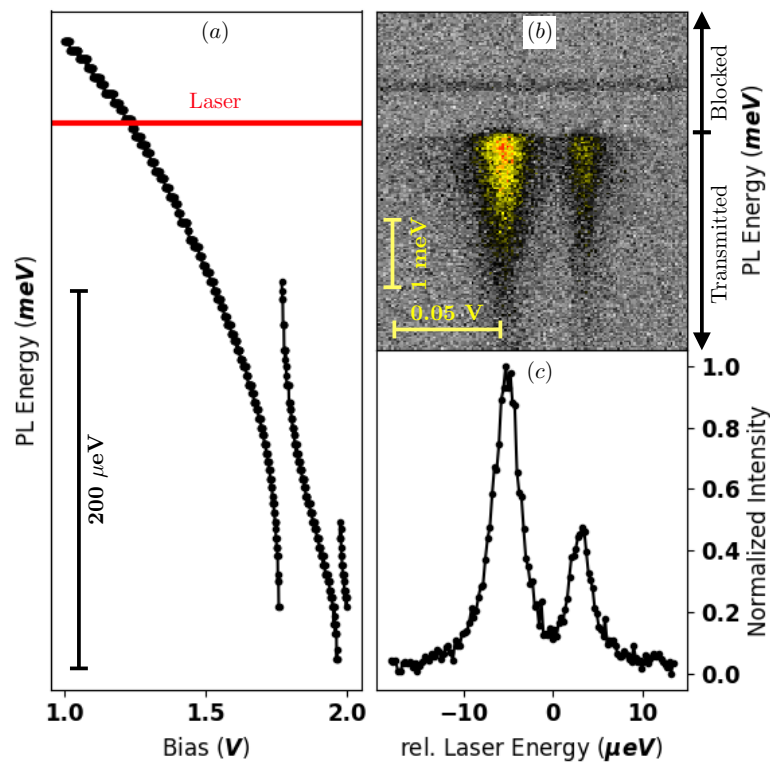


Figure 5.4: **(a)** Maximum PL intensities of the ground state neutral exciton. The quasi-resonant laser excitation energy is shown as a horizontal red line. **(b)** The tail of the acoustic phonon resonance as the exciton is swept through the laser energy. The benefits of a triple spectrometer in subtractive mode can clearly be seen as some stray laser light is shown less than 1 meV above the phonon tails. **(c)** Averaged PL from **(b)** showing the high resolution of this technique. The e-h exchange splitting can clearly be seen and the lifetime-limited linewidths can be easily extracted from fits of the data [65].

# Chapter 6

## Statically Strained PL

In the previous chapter, we described a method for improving the resolution of a basic spectroscopy setup by utilizing the interactions of phonons with the electronic transitions in QDs. In this chapter, we discuss the application of static strain via a home-built cryogenic atomic force microscope. In this set of experiments, we are able to determine the sensitivity of the optical transitions in QDs to strain in their local environment. Most crucially, we quantify the effect of force on the transition energies of QDs embedded in PhC membranes. The experimental apparatus discussed in this chapter allows direct measurements of the strain induced PL shift in QDs and can be used to quantitatively compare the sensitivity of the QDs to strain with other, less direct, methods of inducing strain.

### 6.1 Sample Heterostructure

The sample used in these experiments was grown by molecular beam epitaxy. The layer structure is as follows:

30 nm p-GaAs (Be doped)  
10 nm i-GaAs  
10 nm n-GaAs (Si doped)  
70 nm i-GaAs  
2.5 nm QDs InAs  
20 nm i-GaAs  
40 nm n-GaAs (Si doped)  
950 nm  $\text{Al}_{0.7}\text{Ga}_{0.3}\text{As}$   
n-GaAs Substrate

The resulting n-i-n-i-p diode structure makes use of an extra n-doped layer for the purpose of reducing the built-in electric field [69]. This has the effect of lower the forward bias at which the QDs trap charges resulting in smaller currents and less overall heating of the structure [70, 71].

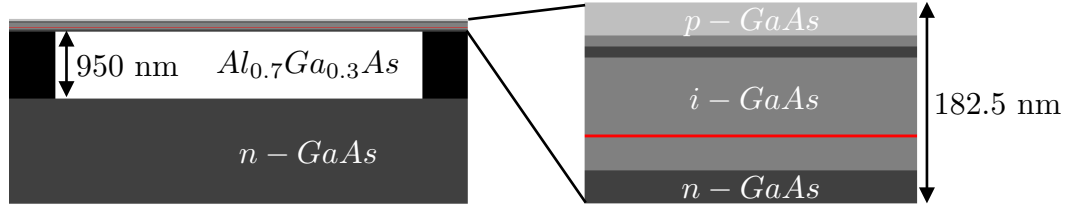


Figure 6.1: Layer structure diagram displaying the absence of the sacrificial  $\text{Al}_{0.7}\text{Ga}_{0.3}\text{As}$  layer underneath the resonators as well as the n-i-n-i-p diode layer that makes up the resonators. The red line is the QD layer.

## 6.2 Force Calibration

As the sample approaches the AFM probe, a change in reflectivity is picked up by the QPD as the reflections of the laser light from the AFM probe and the sample surface contribute toward an interference signal. The intensity of such a signal can be calculated with:

$$I = I_0 \cos^2(kd \cos \phi), \quad (6.1)$$

where  $I_0$  is the intensity in the case of constructive interference,  $k = 2\pi/\lambda$  is the wave number,  $d$  is the distance between the two surfaces, and  $\phi$  is the angle of incidence. Knowing the angle  $\phi = 45^\circ$  and the wavelength  $\lambda = 890$  nm of the incident laser light, an equation can be made relating the distance between the two surfaces  $d$  and the period of the detected signal, which for the cosine squared function is  $\pi$  (see Fig. 6.2):

$$kd \cos \phi = \frac{\sqrt{2}\pi d}{\lambda} = \pi \rightarrow d = \frac{\lambda}{\sqrt{2}}. \quad (6.2)$$

Equation (6.2) can be used to calibrate the position of the sample as a function of voltage, the ratio of which is known as the piezoelectric constant:

$$C_{\text{piezo}} = \frac{d}{\Delta V}. \quad (6.3)$$

Combining Eqs. (6.1) - (6.3) yields the calibration of the sample stage position as a function of the applied voltage, which is  $C_{\text{piezo}} = (16.7 \pm 1.2)$  nm/V. It is important to note that this measurement is the major source of uncertainty in the force calculations.

Now that the applied voltage has been converted to the sample stage position, the sample can be pressed into the AFM probe to cause a deflection signal at the QPD. If this is done on a solid part of the sample, then the response curve should result in a linear relationship between the sample stage position and the normalized voltage at the QPD,

$$V_{\text{norm}} = S_{\text{sensor}}d. \quad (6.4)$$

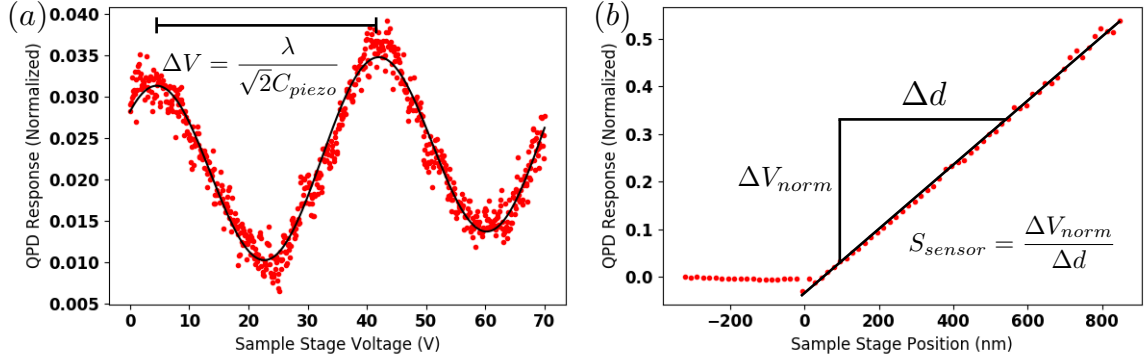


Figure 6.2: **(a)** Interference signal caused by the change in reflectivity of a laser beam due to the decreasing distance between the two surfaces. The black curve represents a fit to Eq. (6.1) and is used to extract the piezoelectric constant  $C_{piezo}$ . **(b)** OBDM performed on a solid section of the sample. This curve is fit to Eq. (6.4) and is used to convert the normalized QPD response to a displacement of the AFM probe. The data from this graph is used to calibrate Fig. 6.4(b).

The slope of this curve is used to calibrate the sensitivity,  $S_{sensor} = (6.96 \pm 0.06) \times 10^{-4} \text{ nm}^{-1}$ , of the QPD to the deflection of the AFM probe  $d$  (see Fig. 6.2(b)). Further experiments can be performed where a portion of the sample containing a PhC cavity membrane is pressed against the AFM probe to determine the deflection in the probe (see Fig. 6.4(b)), which can then be converted to the displacement of the PhC cavity membrane. More details on the calibration method can be found in Appendix B.

Lastly, a calculation of the stiffness of either the AFM probe or the PhC cavity membrane can be used to convert the displacements measured in Fig. 6.4(b) to applied forces. Due to the uncertainty in the stiffness reported by the manufacturer of the AFM probes  $k_{AFM} = (12 - 110) \text{ N/m}$  used in our experiments, there was less error if we used the calculation for the stiffness of the membranes to perform this conversion. This indicates that as long as one can measure the deflection and the geometry of the resonator, then one can calibrate the force. The stiffness coefficient  $k$  for a membrane whose thickness  $t$  is much smaller than its length  $L$  and width  $w$ , and whose width is 0.9 times its length, can be calculated using the equation [72]

$$k = 15 \frac{Et^3}{w^2}, \quad (6.5)$$

where  $E = 85.5 \text{ GPa}$  is the Young's modulus of GaAs [73]. Since the PhC membrane is made by etching holes in a solid free-floating membrane of GaAs, the effective Young's modulus is expected to be lower than that of bulk. However, this effect is not expected to reduce the modulus by more than a factor of two at most. Finite element analysis of a perforated membrane made of GaAs would provide a good estimate for the Young's modulus of the membranes, but for now the calculations are done using the Young's modulus of bulk GaAs. For a PhC cavity membrane with a width of  $7.6 \mu\text{m}$ , length of  $8.3 \mu\text{m}$ , and

thickness of 182.5 nm, the stiffness coefficient is calculated to be  $k = 136$  N/m. This value is obtained by measuring the dimensions of the membrane using SEM. The uncertainties in these lengths are less than 1% and are therefore ignored in the force calculations due to larger sources of uncertainty in the displacements. The forces in the membranes are thus calculated using Hooke's law:

$$|\mathbf{F}| = k|\mathbf{d}|. \quad (6.6)$$

### 6.3 Strain Measurements

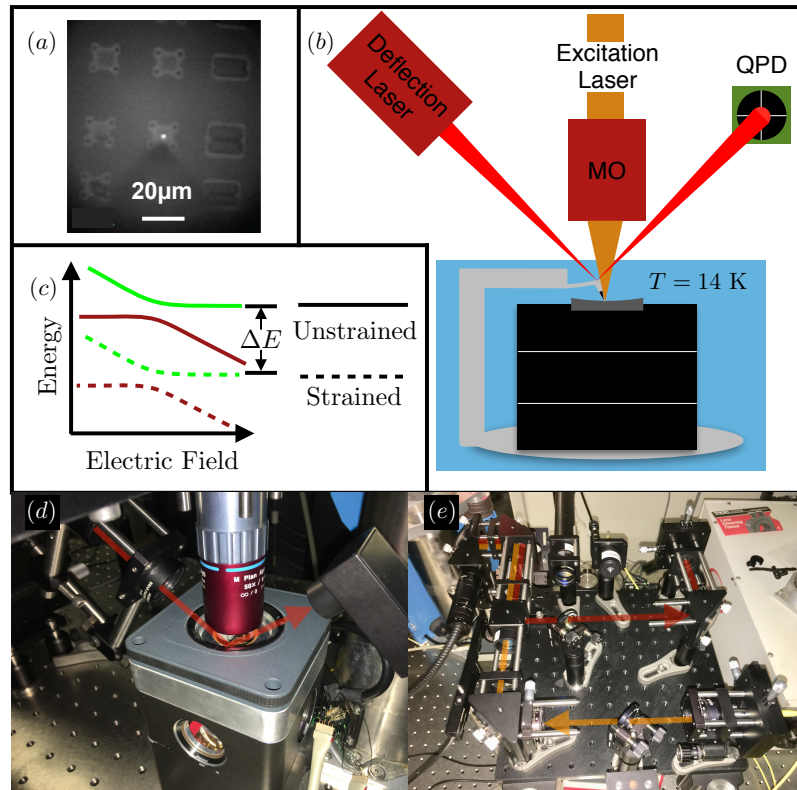


Figure 6.3: (a) Microscope image of the AFM probe situated above the membrane. The excitation laser is positioned to excite QDs near the center of the membrane. (b) Schematic representation of the instrument. A closed-cycle helium cryostat contains the sample on three nanopositioners. An AFM probe is mounted above the sample. The orange laser is used to perform PL on the QDs embedded in the membranes while the red laser is used to perform the OBDM for measuring displacements. (c) Schematic of the effect strain has on the PL of the neutral exciton. (d) Photograph of the OBDM apparatus. (e) Photograph of the entire PL platform situated above the cryostat.

Static strain measurements are performed using a custom-made cryogenic AFM. The AFM is constructed by inserting a specially designed sample mount that incorporates an over-

hanging arm above the sample. This arm accommodates an AFM probe. The entire sample mount is housed inside of a closed-cycle helium cryostat, which allowed the experiments to be conducted at a temperature of  $(14.00 \pm 0.01)\text{K}$ . The detection technique for the strain measurements utilizes the optical beam deflection method (OBDM) where a probe beam is reflected off the back of the AFM cantilever and onto a QPD. The small displacements in the AFM cantilever cause deflection at the reflected laser spot on the QPD, generating a position sensitive readout. A schematic of this setup as well as photographs of the instrument are shown in Fig. 6.3.

The sample under study is an InAs QD embedded in a GaAs substrate that has been doped to create an n-i-n-i-p diode. The *n*-type layers are doped with Si and the *p*-type layers are doped with Be. The diode structure enables control over the electrical environment of the QDs and allows for tuning of the QD electronic states. Below the diode structure lies a 950 nm region of Si-doped  $\text{Al}_{0.7}\text{Ga}_{0.3}\text{As}$  to act as both a blocking layer, to prevent the tunneling of charges to the n-doped substrate, as well as a sacrificial layer which is to be removed by chemical etching for the purpose of creating a free-floating membrane out of the diode section of the sample. The diode region of the sample is further processed by patterning nanostructures using electron-beam lithography and chemical etching techniques. PhC cavity membranes, photonic waveguides, and tuning fork and bridge structures are patterned into the surface using these techniques. The QDs themselves are positioned 60 nm from the bottom of the diode region and 120 nm from the top of the diode region, placing them 30 nm below the mid plane of the diode. This placement allows the QDs to experience an in-plane tensile strain as the membrane is depressed downward.

The experiments were conducted on the PhC cavity membrane structures and involve using a 3D stack of nanopositioners to control the position of the sample beneath the AFM probe. The sample is positioned such that a PhC is directly beneath the tip of the AFM probe (see the inset in Fig. 6.4(c)) and will be raised into the probe to produce a displacement of the PhC cavity membrane which induces an in-plane tensile strain on the QDs. The deflection of the AFM probe is monitored on the QPD to quantify the displacement of the membrane (see Fig. 6.4(b)) while a separate optical setup is used to excite and collect PL from the QDs embedded in the structure. PL bias maps are created by monitoring the PL while stepping the voltage applied to the sample. After acquiring a reference PL bias map at zero strain, the sample is stepped vertically into the AFM probe causing both the probe and the membrane to displace. Another PL bias map is created and the entire process is repeated. A series of 5 PL bias maps were collected as the force on the membrane reached a total of  $(65 \pm 9) \mu\text{N}$  (see Fig. 6.4(a)). After collecting the PL bias maps, the emission signal from the QDs was analyzed to measure the shift in PL energy. From these experiments, it has been shown that the QD PL energy shifts  $\Delta E$  follow a quadratic curve as a function of the force applied to the membrane  $F$  (see Fig. 6.4(c)). The equation for this curve, in units of  $\mu\text{eV}/\mu\text{N}$ , is

$$\Delta E(F) = -0.57F^2 - 6.37F. \quad (6.7)$$

In these experiments, the spectral resolution was  $82.5 \mu\text{eV}$ , due to the parameters of the spectrometer, and the force resolution was  $0.67 \mu\text{N}$  due to the membrane geometry and the vibration amplitude of the cryostation. According to Eq. (6.7), a force of  $0.67 \mu\text{N}$  would



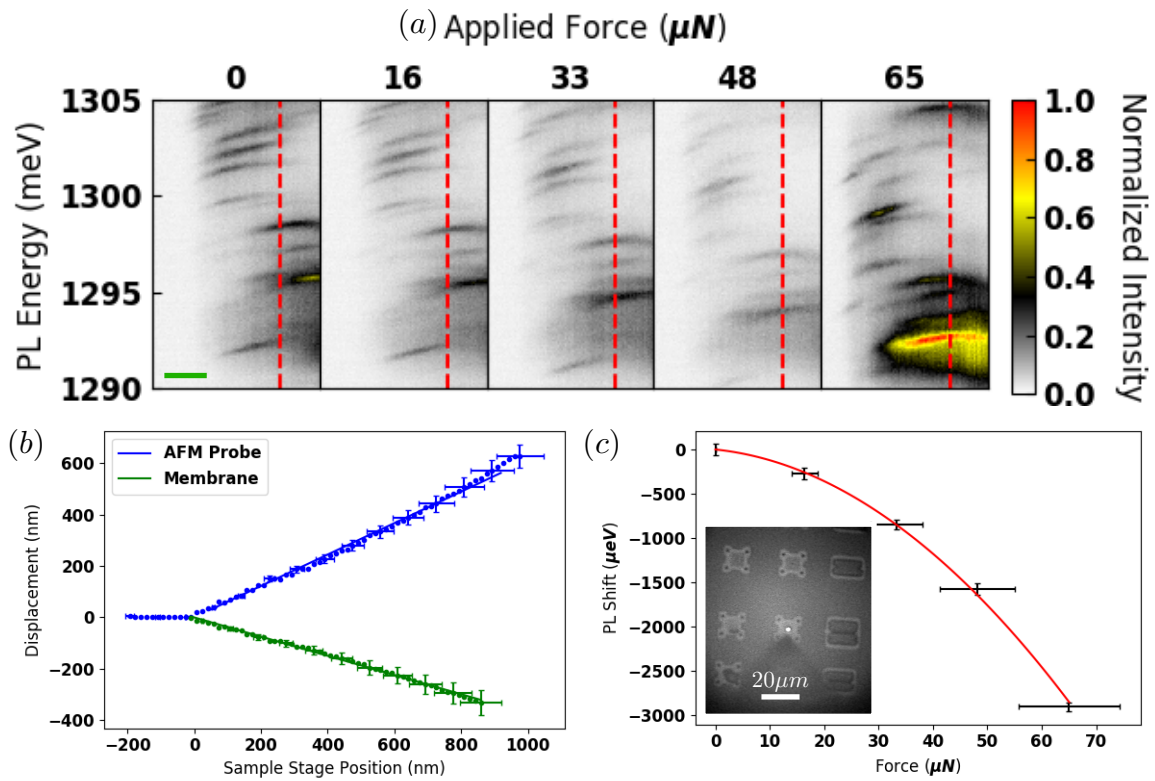


Figure 6.4: (a) Electric field dispersed PL spectra of QDs embedded in a 180 nm thin membrane under in-plane tensile strain. From left to right, the panels represent a QD in a thin membrane experiencing increasing amounts of transverse force as indicated by the values above each false color map. The solid green bar at the bottom of the leftmost panel represents a 0.25 V scale for the horizontal axis of each map. The red dashed vertical lines represent the bias at which the PL energies were recorded. (b) OBDM measurements of the AFM probe displacement (blue) and the associated membrane displacement (green). (c) Quadratic fit to the PL energy shift as a function of applied force. The inset shows the position of the AFM probe above the membrane.

cause a QD strain shift of  $4.52 \mu\text{eV}$ . Therefore, the spectrometer would limit the minimum resolvable force of this experiment to  $7.68 \mu\text{N}$ . There are a number of strategies that could be employed to improve this measurement. A spectrometer of higher resolution, or adding a scanning Fabry-Perot interferometer into the initial optical setup, could enhance the spectral resolution down to the regime where the force resolution becomes the limiting factor. At this point, membranes with smaller stiffness coefficients could be used to further increase the resolution. If the QDs are positioned farther from the central plane of the membranes, they would experience a stronger strain causing their PL to shift by greater amounts. This would also lead to an increase in resolution.

To get an idea of how this system could be utilized as a sensor, I will describe a thought experiment which compares the sensitivity of the system to a gravitational force. The fundamental question this thought experiment addresses would be ‘How close to the mechanical resonator would a 1 kg mass have to be in order to generate the minimally detectable force?’ The gravitational force between two objects is given by Newton’s law of universal gravitation:

$$F = G \frac{m_1 m_2}{r^2}, \quad (6.8)$$

where  $G = 6.674 \times 10^{-11} \text{N}(\frac{\text{m}}{\text{kg}})^2$  is the gravitational constant,  $m_1 = 1\text{kg}$  and  $m_2$  are the masses of the 1kg object and the mass of the mechanical resonator (in this case the membrane), and  $r$  is the distance between the two objects. The mass of the membrane can be calculated by multiplying the density of the material (GaAs) by the volume of the membrane:

$$m_2 = \rho V = 5320 \frac{\text{kg}}{\text{m}^3} (8.3\mu\text{m})(7.6\mu\text{m})(0.2\mu\text{m}) = 67\text{pg}. \quad (6.9)$$

The gravitational force between a 1kg mass and a 67pg mass as a function of separation is:

$$F(r) = \frac{4.48 \times 10^{-24}}{r^2} \text{Nm}^2 \quad (6.10)$$

Inserting Eq. (6.10) into Eq. (6.7), setting  $\Delta E = 82.5\mu\text{eV}$ , and solving for  $r$  will yield the required separation of the two objects in order to resolve the strain shift with the current experimental setup. This yields a separation of  $r = 0.48\text{nm}$ . This is an impossible separation to achieve when considering that 1kg of the densest metal on Earth, which is gold with a density of  $1932 \text{kg/m}^3$ , would have a spherical radius of 5cm. This would require the membrane to be physically inside of the gold sphere in order to feel a strong enough gravitational attraction to the center of mass in order to yield a measurable strain shift. Improvements can be made to the sensitivity by embedding QDs at the high strain point of a cantilever and adding a large test mass to the free end of the cantilever. The technique of phonon assisted quasi-resonant fluorescence spectroscopy could also be utilized to improve the sensitivity of the system to optical shifts. Even more sensitivity can be obtained if one could couple entangled spin states in QDs to the mechanical strain induced by such a gravitational force. The beginnings of realizing such a spin-mechanical coupling in QDs embedded in mechanical resonators is discussed in the following chapter.

# Chapter 7

## Dynamically Strained PL

In the previous chapter, we described the apparatus and results of an experiment to measure static strain imparted on QDs using the nanoindentation tip of an AFM. Here, we shift focus and consider the application of dynamic strain via an amplitude-modulated laser. In this set of experiments, we are able to determine the mechanical resonance frequency of the nanoscale structure in which the QDs are embedded. We also visualize a few of the mechanical oscillation modes of a photonic crystal membrane via strain-induced PL shifts. Most crucially, we discern the effect of strain on hole spin states of the QD, paving the way for future experiments of higher precision that may eventually measure electron spin-strain coupling and have applications in quantum metrology and sensing. More information about this work can be found in an upcoming article [26].

### 7.1 Sample Heterostructure

The sample used in these experiments was grown by molecular beam epitaxy. The layer structure is as follows:

30 nm p-GaAs (Be doped)  
10 nm i-GaAs  
10 nm n-GaAs (Si doped)  
70 nm i-GaAs  
2.5 nm QDs InAs  
30 nm i-GaAs  
30 nm n-GaAs (Si doped)  
950 nm  $\text{Al}_{0.7}\text{Ga}_{0.3}\text{As}$   
n-GaAs Substrate

The resulting n-i-n-i-p diode structure makes use of an extra n-doped layer for the purpose of reducing the built-in electric field [69]. This has the effect of lowering the forward bias at which the QDs trap charges resulting in smaller currents and less overall heating of the structure [70, 71].

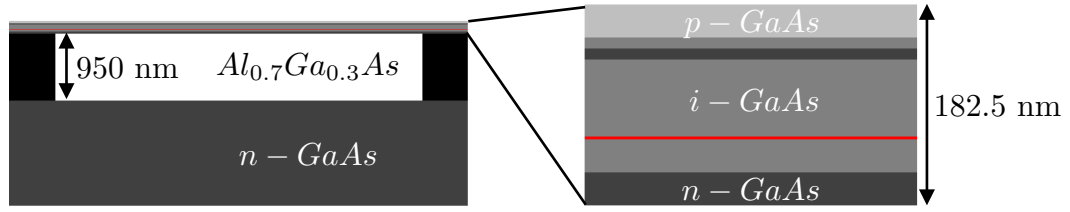


Figure 7.1: Layer structure diagram displaying the absence of the sacrificial  $\text{Al}_{0.7}\text{Ga}_{0.3}\text{As}$  layer underneath the resonators as well as the n-i-n-i-p diode layer that makes up the resonators. The red line is the QD layer.

## 7.2 Displacement Calibration

The mechanical resonator displacement can be estimated through interference measurements. The signal laser focused onto the mechanical resonators will reflect off both the top and bottom surfaces of the mechanical resonator, as well as the substrate beneath the sacrificial layer. The superposition of these reflected waves will create an interference pattern at the detector. This interference pattern will shift as a function of the gap between the mechanical resonator and the substrate. This interference can be utilized in a manner similar to Ch. 6 where the force and distance were calibrated using interferometric techniques. By modeling the system as three parallel surfaces undergoing a sinusoidal change in their relative positions, the calculated interference signal in the time domain can be matched to the experimental data.

The experiment is performed by focusing two laser beams onto the mechanical resonator. The first is for the purpose of driving the mechanical resonances of the structure and the second is for measuring the interference signal due to the induced oscillations. With the optical setup, we have the ability to independently control the positioning of these two laser beams. This reduces cross-talk between the two optical signals as well as allows us to probe the generated modes of vibration spatially.

Figure 7.2(a) depicts the scenario where a beam reflects off the three surfaces before recombining at the detector. The optical signal is detected by an APD which is connected to an oscilloscope that is triggered at the modulation frequency of the drive laser.

When the drive power is low, the reflected signal is sinusoidal because the change in reflectivity is in a regime where its response to the changing gap size is linear. At higher powers, however, there is a saturation effect that occurs near the extrema of the sinusoidal reflectivity curve. This occurs due to the change in reflectivity being periodic with the gap height  $h$  at a given wavelength with a spatial period of  $\lambda/2$ . The saturation occurs when  $\Delta h = 1/4$  period because this is where the reflectivity as a function of gap height has very little change. This yields a saturation gap height of  $\Delta h_{sat} = \lambda/8 = 118$  nm.

Cantilever reflectivity is calculated by modeling the system as a multilayer dielectric stack. The plane waves of the laser are assumed to have normal incidence relative to the stack, which consists of three layers: 180 nm of GaAs (the cantilever), a gap of variable

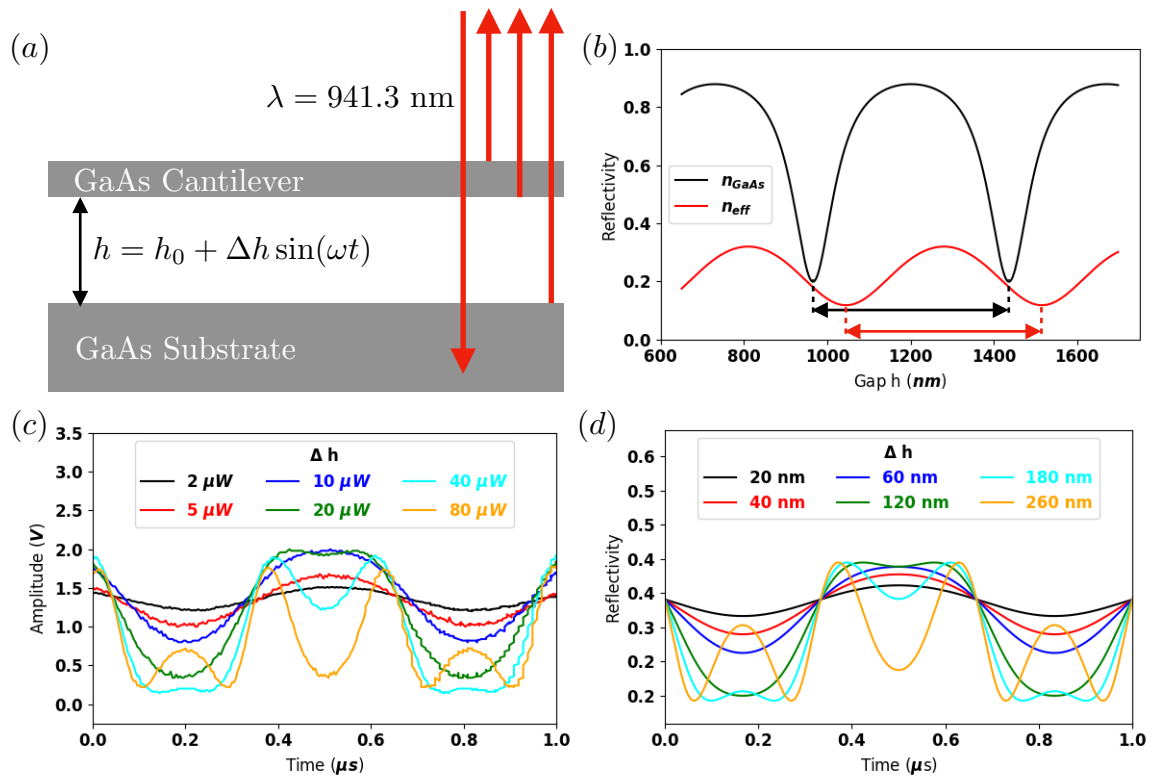


Figure 7.2: (a) Schematic of the GaAs cantilever with multiple reflections of the signal laser from the different surfaces. (b) Fabry-Perot model of reflectivity at 941.3 nm as a function of the gap between the cantilever and the substrate. The black curve shows the reflectivity when using the index of refraction for GaAs and the red curve uses an effective index of refraction. (c) Experimental reflectivity data showing the detected signal amplitude as a function of time for a series of drive laser powers. (d) Fabry-Perot model of the reflectivity as a function of time for a series of gap oscillation amplitudes [26].

height  $h$  (the sacrificial layer), and a semi-infinite layer of GaAs (the substrate). This model assumes that the angle of the cantilever relative to the substrate is negligible, the entire slab fits within a constant portion of the Rayleigh length of the beam waste, and ignores the multiple layers making up the cantilever. Despite these assumptions, the model is still useful for comparison to the experimental results.

When modeling the system using the index of refraction for bulk GaAs  $n_{GaAs} = 3.45$  at  $\lambda = 941.3 \text{ nm}$  the model exhibits too high of a fringe contrast relative to the experimental results. For this reason an effective index of refraction  $n_{eff} = 0.7n_{GaAs} + 0.3n_{vac}$ , where  $n_{vac} = 1$  is the vacuum index, is used. This model was chosen because the effective index of refraction reduces the fringe contrast of the theoretical reflectance to match the experimental data. The explanation for this effective index is that the beam diameter  $w_b$  at the cantilever is likely larger than the width of the cantilever  $w_c = 1.0 \mu m$  itself. Knowing the width of the cantilever and the values for the coefficients of the two indices that produce the closest

match to experimental data, we can calculate the beam width to be  $w_b = 1.43 \mu\text{m}$ . The estimated beam width is consistent with the given input beam parameters and the objective parameters.

Although this theoretical model seems to capture the observed optical response for small cantilevers that have widths smaller than the diameter of the focused beam spot, it does not replicate the expected fringe contrast of a cantilever that has a width equal to or larger than the focused beam spot. For this reason, an alternative theoretical model can be used for these structures that is based on the interference of a range of plane waves at various angles focused onto the cantilever rather than a single plane wave. This range of plane waves causes a broadening of the interference fringes. Reference [74] provides the Fourier spectrum of a focused Gaussian beam, and is used in conjunction with the calculated reflection coefficients for each plane wave component to arrive at the integrated Fourier spectrum, yielding the reflected power. This method retains the original fringe contrast of the effective index of refraction method, but also works for the case when the cantilever width is larger than the focused beam spot size. The calculated reflectivity is plotted as a function of time for a series of maximum sinusoidal displacements  $\Delta h$  where

$$h = h_0 + \Delta h \sin(\omega t) \quad (7.1)$$

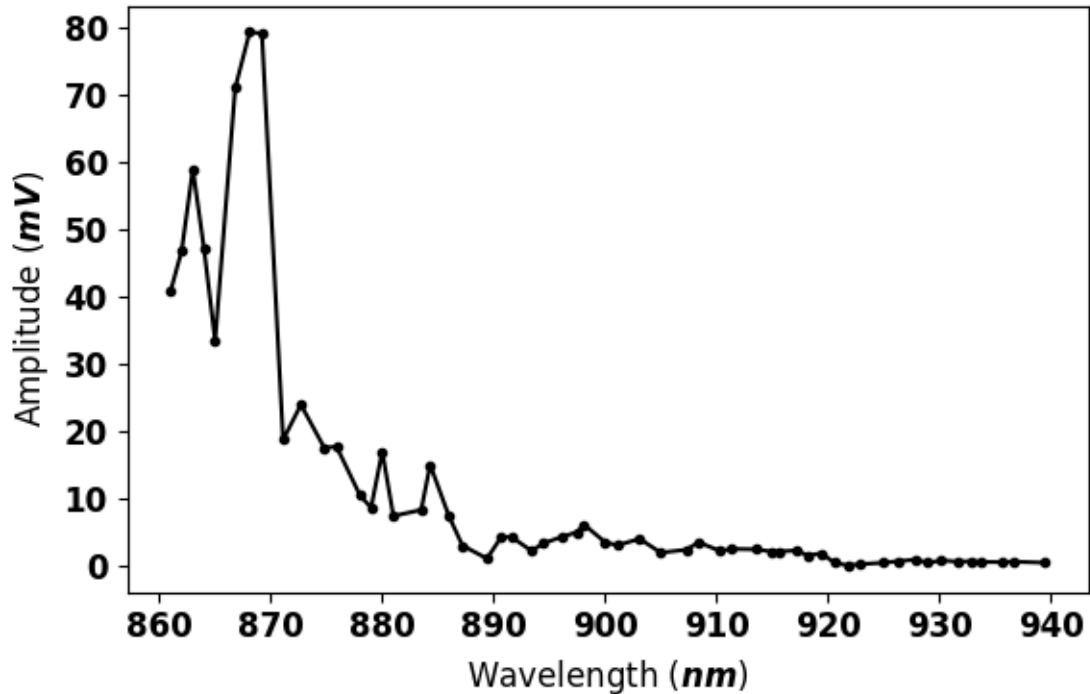


Figure 7.3: Mechanical response amplitude as a function of drive laser wavelength for a microcantilever. Note the peak in the response curve on resonance with the wetting layer for the InAs QDs at  $\lambda = 870 \text{ nm}$ .

and  $\omega$  is the mechanical resonance frequency. We have calculated that the reflectivity best matches the experimental data for the case of a 40  $\mu\text{W}$  drive when  $\Delta h = 180$  nm. This power was chosen because it was closest to the drive power used in the QD experiments.

In addition to calibrating the amplitude of oscillation as a function of drive power, the amplitude of the interference signal was also measured as a function of drive wavelength. It is clear that the resonator is driven more intensely at low wavelengths which could be due to the higher energy photons creating more phonons in the structure. It is interesting to note that there is a peak in the response curve at  $\lambda = 870$  nm, the wavelength of light that is equivalent to the band gap energy of the InAs wetting layer of the QDs. This suggests that a photothermal effect for the drive mechanism could potentially map out the electronic states of a QD sample. Figure 7.3 shows the results of this experiment. For each wavelength the drive power was adjusted to be 20  $\mu\text{W}$  at the sample. However, the laser spot size was not adjusted at each wavelength to compensate for the refractive effect of the lenses. This could introduce errors in the form of intensity variations at the sample due to changes in the area covered by the laser spot, even though the laser power was kept constant.

### 7.3 Single Phonon Coupling Strength

According to Aspelmeyer et al. [17], the zero point motion for a cantilever at the free end is

$$x_0 = \sqrt{\frac{\hbar}{2m_{eff}\Omega_m}}, \quad (7.2)$$

where  $m_{eff}$  is the effective mass of the cantilever and  $\Omega_m$  is the mechanical resonance frequency. Equating the potential energy of the cantilever to the kinetic energy,

$$U = \frac{1}{2}m_{eff}\Omega_m^2 x^2 = T = \frac{1}{2}m\Omega_m^2 \langle d^2 \rangle, \quad (7.3)$$

where  $\langle d^2 \rangle$  is the average of the square of the displacement over the cantilever and  $m$  is the total mass of the cantilever, results in an effective mass of

$$m_{eff} = m \frac{\langle d^2 \rangle}{x^2}. \quad (7.4)$$

Since  $x$  is defined as the displacement at the tip of the cantilever, we obtain  $m_{eff} = 0.3m$ , where the total mass is  $m = 1.38 \times 10^{-14}$  kg. This yields a zero-point motion of  $x_0 = 95$  fm. Through the use of finite element analysis, the zero-point strain can be calculated at the position of the QD for a given tip displacement. The results of our model yield a zero-point strain of  $\epsilon_0 = 1.25 \times 10^{-10}$  and a single phonon coupling strength of  $g_0 = G\epsilon_0 = 2$  kHz, where  $G = 16.5$  THz/strain.

### 7.4 Strain Measurements

The first step was to measure the mechanical resonance spectra of the resonators to gather the frequencies of the various vibrational modes. Figure 7.4 shows a SEM image of a mi-

cantilever along with the calculated strain profile, the mechanical resonance spectrum for a tuning fork along with a closeup of the fundamental mode, and PL from the negative trion transition of a QD embedded at the high strain point of a tuning fork. One will notice that the PL has a strong shift in transition energy when the micro resonator is driven on resonance with the fundamental mode. The resonators were driven by focusing an amplitude modulated drive laser at the point of contact between the micro resonators and the bulk of the sample. A signal laser was then positioned at the free end of the structure because this is the point of highest amplitude. The reflection of the signal laser would subsequently be modulated by the mechanical motion of the resonator. To perform PL, the signal laser would instead be used to optically excite the electronic states of a QD near the point of

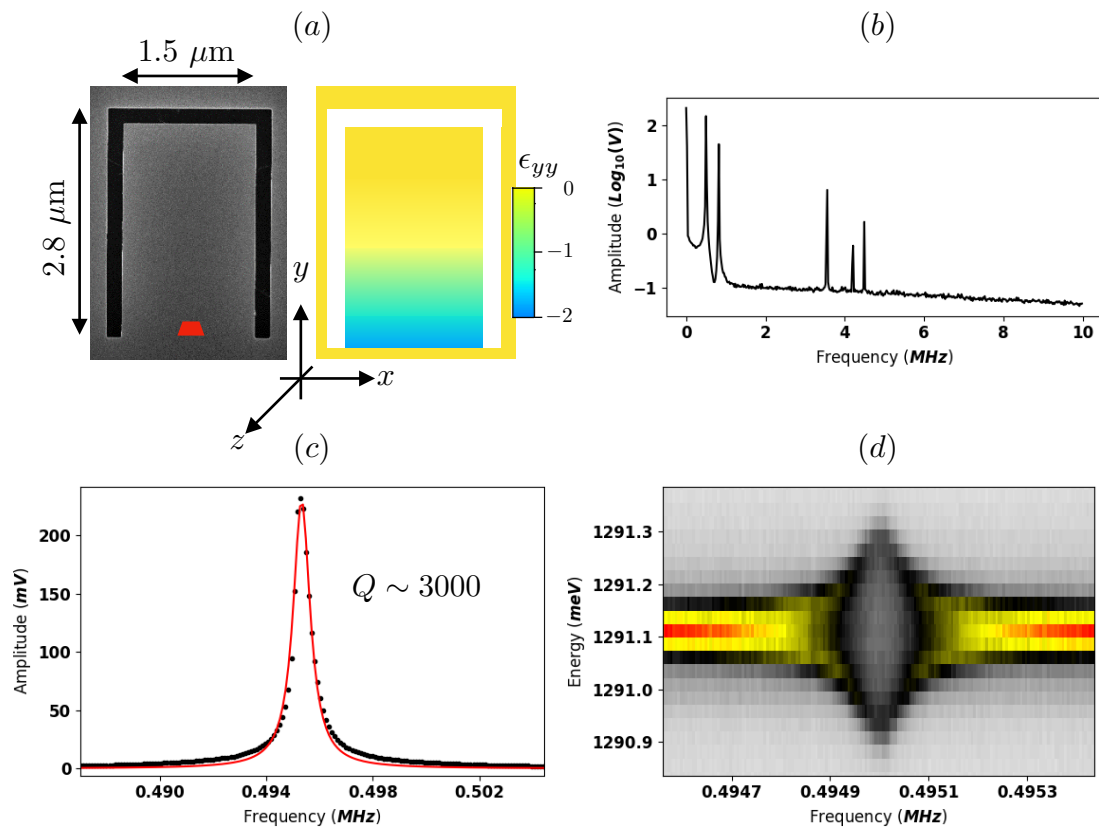


Figure 7.4: (a) SEM image of a cantilever shown with the estimated position of the QD studied on the left accompanied by a colormap on the right displaying the axial strain at the QD layer calculated using a finite element method. The colorbar has a scale of  $10^{-4}$  fractional change in length. (b) Mechanical resonance spectrum of a tuning fork structure measured by a spectrum analyzer. (c) Closeup of the fundamental mode of a tuning fork structure. The red curve is a Lorentzian fit to the data and the fit parameters indicate a quality factor of  $Q \sim 3000$ . (d) PL emission of a QD in a tuning fork as the frequency of the drive laser is swept through the mechanical resonance [26].



contact between the mechanical resonator and the supporting material.

The next measurements probing the strain-induced PL shifts of QDs embedded in mechanical resonators sought to uncover the effect the QD position on the magnitude of the shift. To do this, the membranes were driven by an amplitude modulated laser near the middle of the long edge, at the drain lines (or holes), to induce mechanical motion. A second probe laser was used to excite the electronic states of the QDs along the waveguide. The PL from the excited QDs would travel down the waveguide and exit the structure along one of the output couplers. This PL is collected by a microscope objective and sent to spectroscopic equipment for analysis. The probe laser is moved along the waveguide to excite QDs at varying positions along the membrane. From this experiment we were able

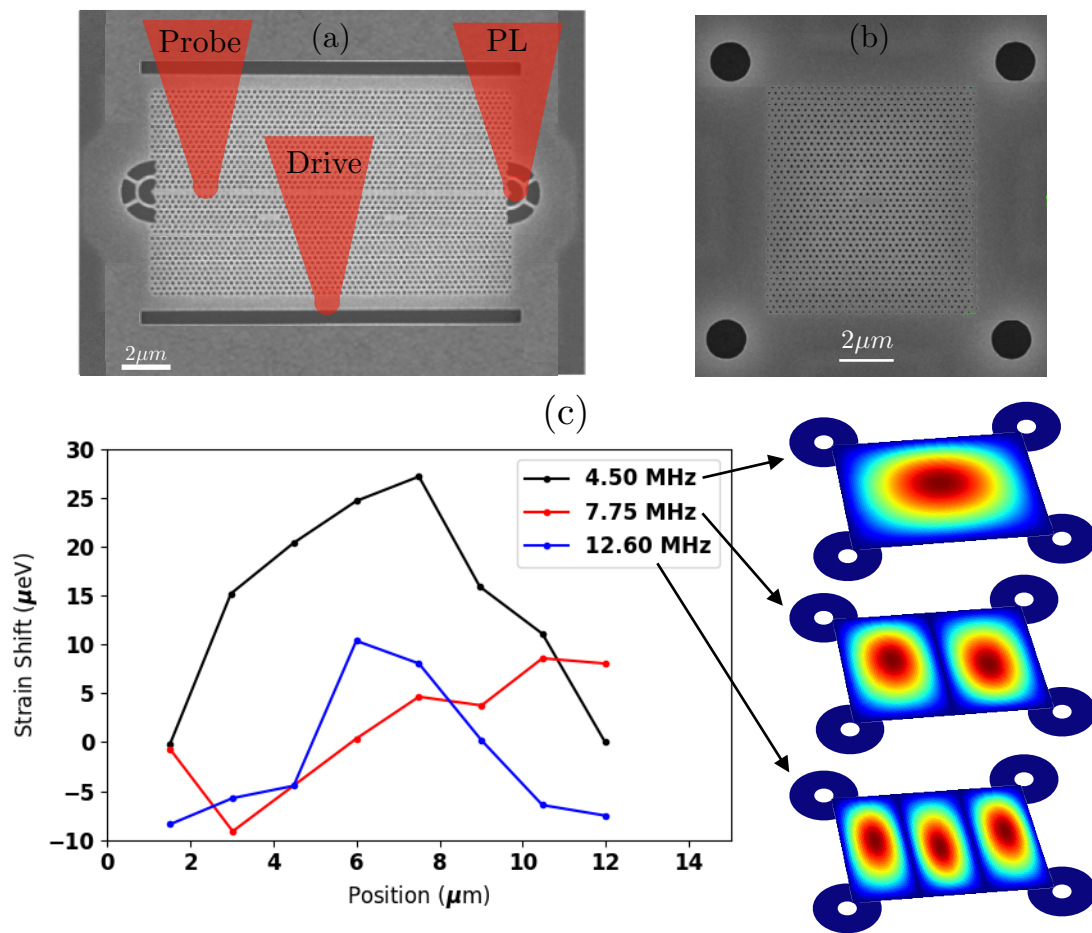


Figure 7.5: (a) SEM image of a PhC membrane structure with a waveguide, two cavities, and output couplers patterned into the surface. For this pattern, the sacrificial layer was removed through drain lines. (b) SEM image of a PhC membrane containing a single cavity. For this pattern, the sacrificial layer was removed through drain holes. (c) Strain induced PL shift as a function of the position of QDs along a membrane. The images on the right show colormaps of the displacement of the first three modes [13].

to map out the strain shift in the PL of the QDs as a function of their position along the membrane as well as the optical driving frequency used to induce the mechanical motion. Figure 7.5 shows the results of this experiment for the first three modes of a PhC membrane. It can be seen that the strain shift of the PL in these QDs follows the displacement of the membrane quite closely for the first three fundamental modes. Wherever the displacement is large, the strain shift is large.

After observing the effect strain has on the electronic states of a QD, our focus shifted toward observing the effect of strain on the spin states. To perform this experiment, the negative trion to bare electron transitions were chosen as the prime candidates. These transitions were chosen due to the fact that the excited state has a pair of electrons locked in a spin singlet, leaving only the spin of the hole as a variable, while the ground state of the transition has a single hole. By Zeeman splitting the spin states with a 6T magnetic field oriented perpendicular to the growth direction of the QDs (Voigt geometry), the transition energies of the four possible recombinations were measured. Taking the difference between peaks 1 and 2 or 3 and 4 would yield the value of the hole spin splitting, while taking the difference between peaks 1 and 3 or 2 and 4 would yield the electron spin splittings. Figure 7.6 shows the transitions of interest as well as a high resolution PL spectrum of the different transitions of a negative trion. The high resolution PL was collected through a Fabry-Perot with a resolution of  $\sim 9 \mu\text{eV}$ , dispersed by a 750 mm spectrometer, and detected by a LN cooled CCD camera.

The most recent experiments performed utilized TCSPC to measure the strain shifts of the electron and hole spins undergoing mechanical oscillations. Figure 7.7(a) shows the PL

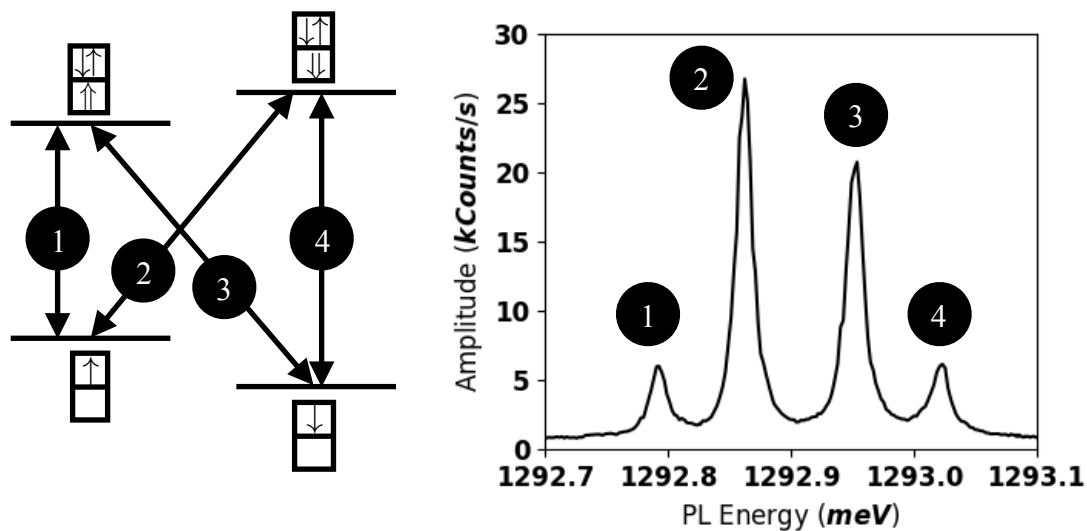


Figure 7.6: **(Left)** Simple energy diagram of the spin states of a negative trion  $X^{-1}$  under a magnetic field and the possible transitions. **(Right)** High resolution PL spectrum of the negative trion under a magnetic field. The possible transitions have been labeled and correspond to those on the left [13].

emission from the transitions of a negative trion as a function of time for an entire period of oscillation of the mechanical resonator, which in this case was a tuning fork structure modulated at its fundamental vibrational mode. The main finding of this experiment is displayed in Fig. 7.7(b), where the spin splitting for the holes exhibit a noticeable shift along with the overall electronic transitions of the negative trion, while the electron spin splittings appear to stay relatively constant. This is attributed to the spin-orbit coupling of the hole states in a semiconductor crystal. Electrons occupying the conduction band are in *s*-like orbitals, while the electrons (holes) occupying the valence band are in *p*-like orbitals which exhibit spin-orbit coupling. For this reason, the strain coupling of the electron spins is sometimes below the limit of what can be experimentally measured and has been estimated to be roughly 3-4 times weaker than that of the hole spins.

In semiconductor QDs, the charges are strongly confined along the growth direction, and through spin-orbit coupling can cause the *p*-like orbitals of the holes to preferentially orient themselves along this axis. With the application of an in-plane magnetic field, the hole spins slightly shift away from vertical alignment; however differences between different atomic locations average out the vertical component, yielding a cumulative spin aligned closer to the in-plane magnetic field. By applying strain, the individual hole spins shift in alignment either closer or farther from a vertical orientation. This has the effect of changing the strength by which the spins couple to the magnetic field, causing a shift in the Zeeman splittings.

At first glance, it is apparent that the coupling of hole spins to strain is much weaker than that of the electronic transitions ( $\sim 1 - 4\%$ ). However, hole spin coherence times have been shown to be about 3 orders of magnitude longer than those of electronic transitions  $\tau_{h,spin} \sim \tau_{electronic} \times 10^3 \sim 1 \mu s$  [75, 76, 77]. This suggests that hole spins can be much more sensitive to strain than the electronic transitions if one takes advantage of the longer hole spin coherence times. The experiments we have performed thus far utilize the techniques of PL and do not make use of the advantages gained by the longer coherence times. There are other experimental techniques which could be performed that would take advantage of this longer-lived transition, namely Raman spin flip spectroscopy [71, 78, 79] or Ramsey fringe interferometry [80, 81, 82].

By converting the zero point motion of the cantilever to the strain felt at the QD, we are able to calculate the coupling strength of the hole spin to a single quantum of mechanical motion  $g_0 = 2$  kHz. This value is orders of magnitude stronger than the spin-strain coupling of similar quantum systems such as nitrogen vacancy centers in diamond ( $g_0 = 0.04 - 2$  Hz) [83, 84, 85, 86]. This value could be increased further by shrinking the size of the mechanical resonator. If the value of  $g_0$  could reach the MHz regime, then the spin-strain coupling of the zero point motion would be comparable to the coherence times of the spins themselves. This would open the door to quantum systems sensitive to the motion on the order of single phonons. These results suggest that QDs embedded in mechanical systems are a promising candidate for spin-mechanical couplings that allow access to the quantum limits of motion, and could advance the fields of quantum sensing and coupled quantum systems.

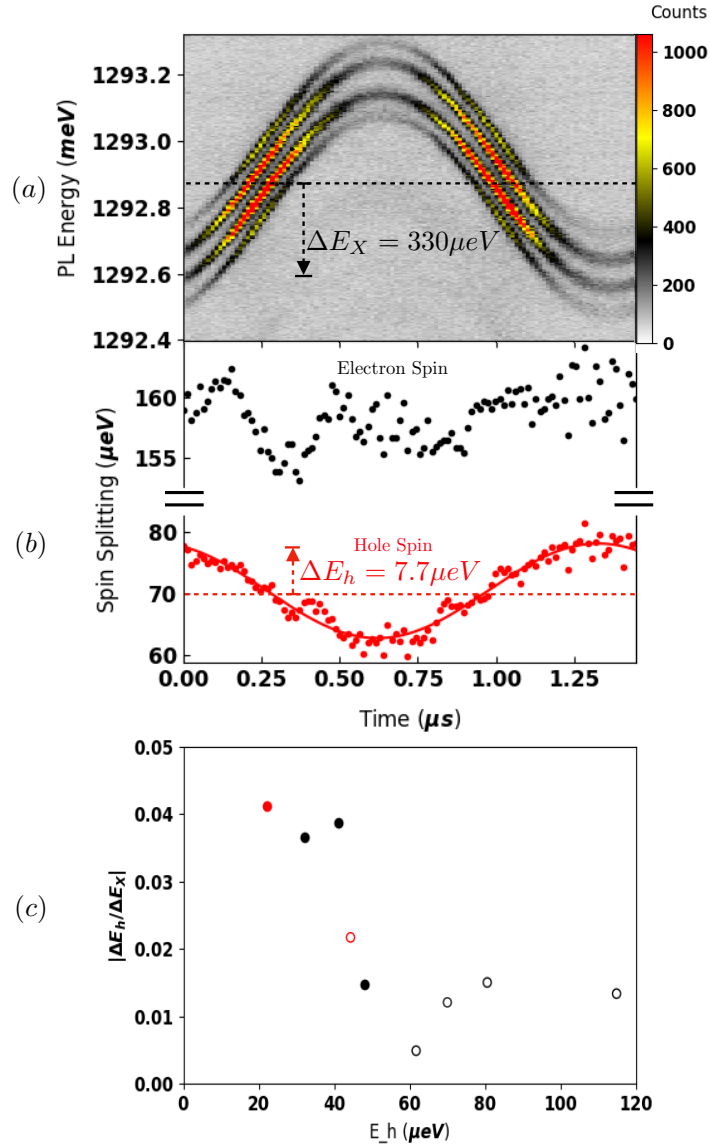


Figure 7.7: **(a)** TCSPC measurement of the individual spin states of the negative trion under 6T magnetic field and as a function of the oscillation period of the fundamental mode of the mechanical resonator [13]. **(b)** Electron and hole spin splittings as a function of the oscillation period of the mechanical resonator [13]. The solid red line indicates a sinusoidal fit to the hole data. **(c)** Ratio of the change in hole Zeeman splitting to the change in optical transition energy as a function of the hole Zeeman splitting for 9 different QDs. Red circles indicate that only one set of lines could be measured, either inner or outer. For these cases,  $\Delta E_e$  is assumed to be negligible to find  $\Delta E_h$ . Open (closed) circles indicate the hole and optical transition shifts are out of phase (in phase). The average drive power varies from 20-40  $\mu W$  for different QDs, and the PL laser power is 5  $\mu W$  [26].

# Chapter 8

## Conclusion

Throughout this dissertation, many techniques of optical spectroscopy were discussed along with their benefits towards probing the quantum mechanical properties of QDs. Along with the techniques of optical spectroscopy, this dissertation demonstrated the use of a cryogenic based atomic force microscope to impart  $\mu\text{N}$  forces on PhC membranes containing QDs and reported on the observations of the strain induced shifts that occurred as a result. Such a direct method for probing the coupling of strain to the optical properties of QDs is ideal for numerous reasons. The method does not rely on any external fields which could act as sources of noise towards the measurements of the optical transitions of the QDs. The optical beam deflection method for measuring the displacement of the cantilever has a low setup cost relative to other optical techniques of straining the mechanical system which rely on expensive optical modulators, spectrum analyzers, and time correlated detection devices. The technique of nanoindentation atomic force microscopy was utilized to gather information on the sensitivity of the quantum system to the mechanically induced strain.

In addition to the atomic force microscope induced strain shifts, all-optical methods were also utilized to study the strain shifts in QDs. In particular, the spin states of QDs embedded in microcantilevers were observed to shift along with the electronic states when strained. Most notably, the spin splittings of holes in QDs exhibit strain shifts and demonstrate the coupling of quantum mechanical systems to mechanical resonators.

In summary, QDs embedded in mechanical resonator systems have the potential to enable a new class of precision sensors. These devices can be tailored to exhibit characteristics sensitive to specific aspects of the environment. The relatively high sensitivity of the QD properties to mechanical motion compared to other quantum systems, such as nitrogen vacancy centers in diamond, deems them worthy candidates for a number of technologies, including accelerometry for inertial navigation, and gravitational gradiometry for detection of shielded nuclear materials. Since QDs embedded in mechanical resonators are sensitive to the motion of the structure, one could imagine that the reverse could also be possible. In particular, the macroscopic mechanical motion could be coherently coupled to the quantum mechanical degrees of freedom of the QD system. Another avenue of research is to understand the relationship between heat and energy within the hybrid system. It may be possible to study heat dissipation in nanoscale systems. There also exists potential for the research of these devices to advance the field of quantum information processing.

# Appendix A

## Derivation of the Euler-Bernoulli Beam Theory

The material described in this chapter adopts the formalism of chapter 5 of Bauchau and Craig's *Structural Analysis* [87]. A beam is defined as a rigid object whose length is much larger than its extent in the other two dimensions. The beam's axis runs along the longest dimension. Euler-Bernoulli beam theory examines the relationships between an applied force at a position along the beam and the corresponding stress and strain fields that result. This theory begins with the assumptions that the beam is infinitely rigid within the plane of a cross-section perpendicular to the beam axis, and that the cross-section remains plane and normal to the beam axis during deformation. Empirical data demonstrates that these assumptions are generally valid for long, thin beams made of isotropic materials with rigid cross-sections. Figure A.1 depicts such a beam before and after applying an end bending moment  $M$ .

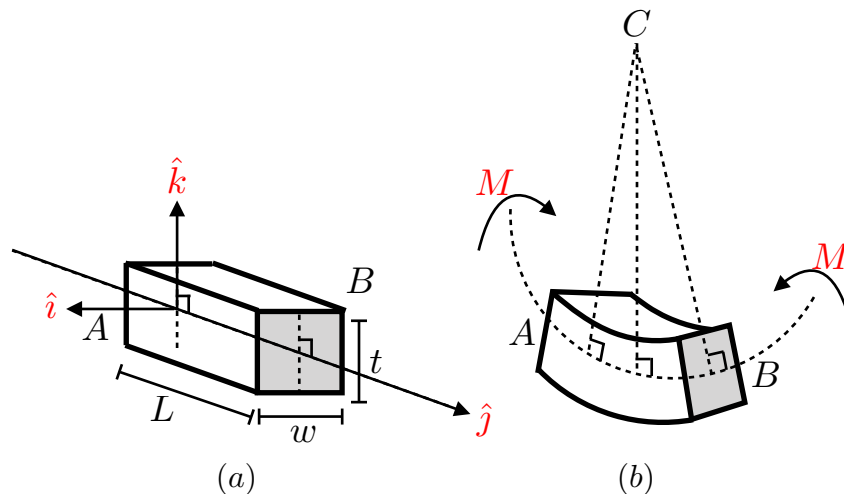


Figure A.1: Schematic of a simple beam in (a) unbent and (b) bent positions. The beam has length  $L$ , width  $w$ , and thickness  $t$ . The bending moments  $M$  cause the beam axis to make a circular arc with center  $C$ .

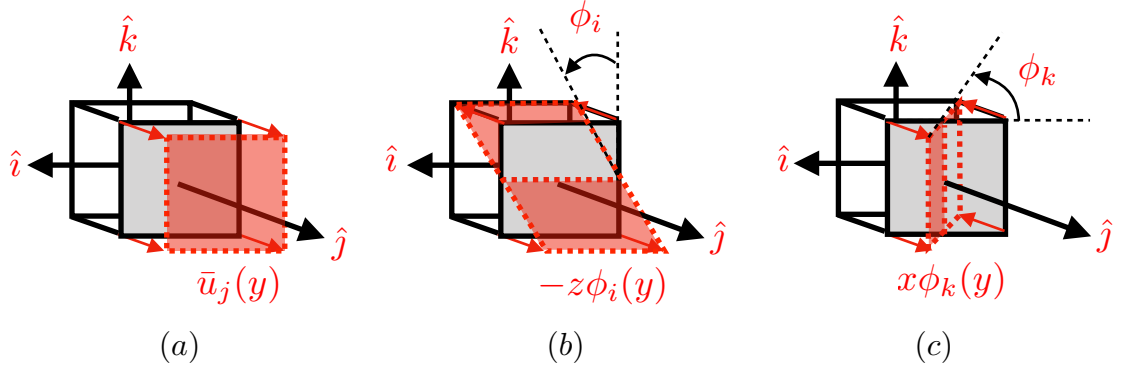


Figure A.2: Schematic of the (a) rigid-body translation and the (b,c) two rigid-body rotations of the axial displacement field.

We define a Cartesian coordinate system at the center of the cross-section with the unit vectors  $(\hat{i}, \hat{j}, \hat{k})$ . The displacement of an arbitrary segment of the beam in each of these three directions is  $u_{ijk}(x, y, z)$ , where  $x, y$ , and  $z$  are the coordinates. Examining the aforementioned assumptions further, we can deduce specific constraints that allow us to simplify the mathematical model. Due to the assumption of infinite rigidity, the displacement field within the plane of the cross-section is composed of two rigid-body translations  $u_i(x, y, z) = \bar{u}_i(y)$  and  $u_k(x, y, z) = \bar{u}_k(y)$ . The planar assumption restricts the axial displacement field to one rigid-body translation  $\bar{u}_j(y)$  and two rigid-body rotations  $\phi_i(y)$  and  $\phi_k(y)$ , as in Figs. A.2 and A.3. These results yield a displacement field of:

$$u_i(x, y, z) = \bar{u}_i(y), \quad (\text{A.1})$$

$$u_j(x, y, z) = \bar{u}_j(y) + x\phi_k(y) - z\phi_i(y), \quad (\text{A.2})$$

$$u_k(x, y, z) = \bar{u}_k(y). \quad (\text{A.3})$$

Therefore, the entire displacement field of the beam can be analyzed using the three cross-sectional displacements  $\bar{u}_i(y)$ ,  $\bar{u}_j(y)$ ,  $\bar{u}_k(y)$  and their derivatives with respect to  $y$ . The normality assumption allows us to relate the slope of the beam to the rotation of the cross-section as depicted in Eq. (A.4) and Fig. A.3:

$$\phi_i = \frac{d\bar{u}_k}{dy}, \quad \phi_k = -\frac{d\bar{u}_i}{dy}. \quad (\text{A.4})$$

Due to these three assumptions, the Euler-Bernoulli beam theory allows for a one-dimensional beam model where the unknown displacements are all a function of a single variable, the beam-axis coordinate  $y$ . If we consider the strains  $\epsilon$  and angular distortions  $\gamma$  along the in-plane axes, we find:

$$\epsilon_k = \frac{\partial u_k}{\partial z} = 0, \quad \epsilon_i = \frac{\partial u_i}{\partial x} = 0, \quad \gamma_{ki} = \frac{\partial u_k}{\partial x} + \frac{\partial u_i}{\partial z} = 0. \quad (\text{A.5})$$

The in-plane elongations must vanish due to the first assumption of the theory, which states that the cross-section is infinitely rigid in its own plane. As a consequence of the cross-

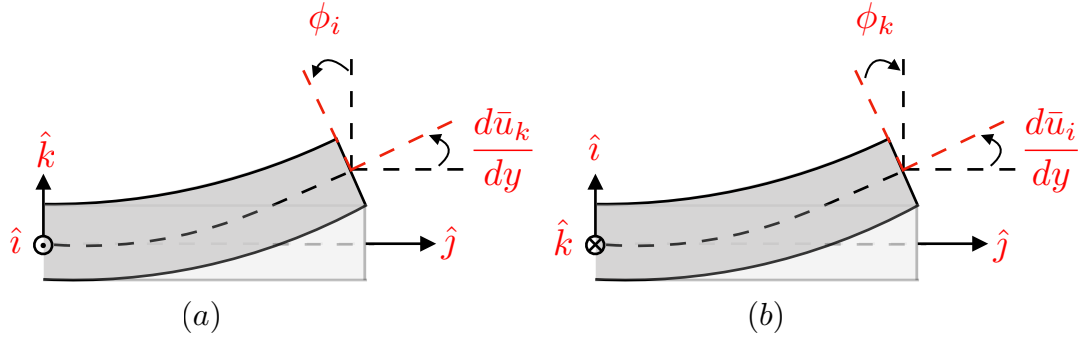


Figure A.3: Relationship between the slope of the beam and the cross-sectional rotation.

section remaining normal during deformation, the transverse angular distortions must vanish:

$$\gamma_{jk} = \frac{\partial u_j}{\partial z} + \frac{\partial u_k}{\partial y} = 0, \quad \gamma_{ji} = \frac{\partial u_j}{\partial x} + \frac{\partial u_i}{\partial y} = 0. \quad (\text{A.6})$$

Lastly, the axial strain field results from the assumption that the cross-section must remain plane during deformation:

$$\epsilon_j = \frac{\partial u_j}{\partial y} = \frac{d\bar{u}_j(y)}{dy} - x \frac{d^2\bar{u}_i(y)}{dy^2} - z \frac{d^2\bar{u}_k(y)}{dy^2}. \quad (\text{A.7})$$

We can simplify this equation by rewriting some of the terms. To do this, we introduce the cross-sectional axial strain  $\bar{\epsilon}_j(y)$  and the cross-sectional curvatures  $\kappa_i$  and  $\kappa_k$  about the  $x$  and  $z$  axes respectively:

$$\bar{\epsilon}_j(y) = \frac{d\bar{u}_j(y)}{dy}, \quad \kappa_i(y) = \frac{d^2\bar{u}_k(y)}{dy^2}, \quad \kappa_k(y) = -\frac{d^2\bar{u}_i(y)}{dy^2}. \quad (\text{A.8})$$

Substituting these terms into Eq. (A.7) yields

$$\epsilon_j(x, y, z) = \bar{\epsilon}_j(y) + x\kappa_k(y) - z\kappa_i(y). \quad (\text{A.9})$$

So far, we have described the displacement and strain in a beam. We can now introduce the stress by examining the internal forces that are generated by the bending. There are three resultant forces and therefore three corresponding stresses. An axial force,  $N_j(y)$ , acts along the  $\hat{j}$  axis, while the two transverse shearing forces,  $V_i(y)$  and  $V_k(y)$ , act along the  $\hat{i}$  and  $\hat{k}$  axes, respectively. The axial force is the result of a stress normal to the  $(\hat{i}, \hat{k})$  plane and is defined as

$$N_j(y) = \int \sigma_j(x, y, z) dA, \quad (\text{A.10})$$

where  $A$  is the cross-sectional area of the beam. The two transverse forces are due to shear stresses and are defined as

$$V_i(y) = \int \tau_{ji}(x, y, z) dA, \quad V_k(y) = \int \tau_{jk}(x, y, z) dA. \quad (\text{A.11})$$



Lastly, there are two bending moments that result from the normal stress,  $M_i(y)$  and  $M_k(y)$ . They are defined as

$$M_i(y) = - \int z \sigma_j(x, y, z) dA, \quad M_k(y) = \int x \sigma_j(x, y, z) dA. \quad (\text{A.12})$$

The negative sign in  $M_i(y)$  stems from the choice of calling the bending moments positive when they are concave up as viewed from the positive side of the axis. Now that we have a mathematical framework, we can apply it to the transverse motion of a beam.

### Transverse Motion of Beams

Here we start with a cantilevered beam that is clamped on one end and free on the other, as in Fig. A.4. The three assumptions of the Euler-Bernoulli beam theory still apply here and allow us to write out the displacement field. Since there are no forces in the  $\hat{i}$  direction, the  $(\hat{j}, \hat{k})$  plane is a plane of symmetry:

$$u_i(x, y, z) = 0, \quad (\text{A.13})$$

$$u_j(x, y, z) = -z \frac{d\bar{u}_k(y)}{dy}, \quad (\text{A.14})$$

$$u_k(x, y, z) = \bar{u}_k(y). \quad (\text{A.15})$$

This results in an axial strain field of:

$$\epsilon_j(x, y, z) = -z \kappa_i(y). \quad (\text{A.16})$$

The transverse loading of a beam yields only one stress resultant and one bending moment: the shear stress along the axis the load is applied,  $V_k(y)$ , and the bending moment normal to the plane of symmetry,  $M_i(y)$ . It is also assumed that the material comprising the beam is made up of a linearly elastic material such that the elastic modulus is simply the ratio of the stress to the strain. With this in mind, the axial strain can be written as

$$\sigma_j(x, y, z) = E \epsilon_j(x, y, z) = -E z \kappa_i(y). \quad (\text{A.17})$$

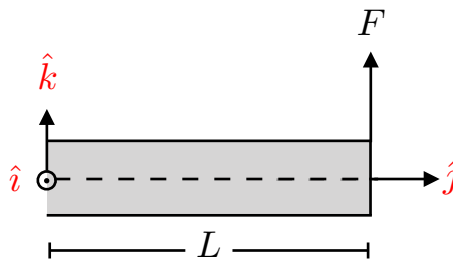


Figure A.4: Schematic of an unbent beam of length  $L$  with concentrated transverse load  $F$  and coordinate system orientation indicated. The left end of the beam is clamped while the right end is free to move.

For a transverse load the beam does not experience an axial force and therefore

$$N_j(y) = \int \sigma_j(x, y, z) dA = -\kappa_i(y) \int E z dA = 0. \quad (\text{A.18})$$

Because the curvature  $\kappa_i(y) \neq 0$ , the integral must vanish:

$$\int E z dA = 0. \quad (\text{A.19})$$

The axial strain can be inserted into the bending moment equation for evaluation:

$$M_i(y) = \kappa_i(y) \int E z^2 dA = \kappa_i(y) H_{11}^c. \quad (\text{A.20})$$

$H_{11}^c$  is the centroidal bending stiffness about axis  $\hat{i}$  and is defined as

$$H_{11}^c = \int E z^2 dA. \quad (\text{A.21})$$

For a homogenous material, the elastic modulus is a constant and can be removed from the integral, leaving behind the area second moment,  $I_{11}^c$ :

$$I_{11}^c = \int z^2 dA. \quad (\text{A.22})$$

Here, the area second moment can be evaluated using Cartesian coordinates:

$$I_{11}^c = \int_{-w/2}^{w/2} \int_{-t/2}^{t/2} z^2 dz dx = \frac{1}{12} w t^3. \quad (\text{A.23})$$

The  $z$ -axis is integrated over the cross-sectional thickness,  $-t/2$  to  $+t/2$ , while the  $x$ -axis is integrated over the cross-sectional width, from  $-w/2$  to  $+w/2$ .

### Static Solution

By constructing a shear load and bending moment diagram on an infinitesimal segment of the beam (see Fig. A.5), these forces and moments can be summed into their respective equilibrium equations. For the case of a cantilever beam with a load concentrated at the free end, the sum of forces must be zero everywhere:

$$dV_k(y) + F\delta(y - L)dy = 0. \quad (\text{A.24})$$

In this equation,  $\delta(y - L)$  is the delta function, which equals one at the position  $y = L$  and zero everywhere else. The sum of torques due to the shear forces and bending moments yields

$$dM_i(y) - V_k(y)dy = 0. \quad (\text{A.25})$$

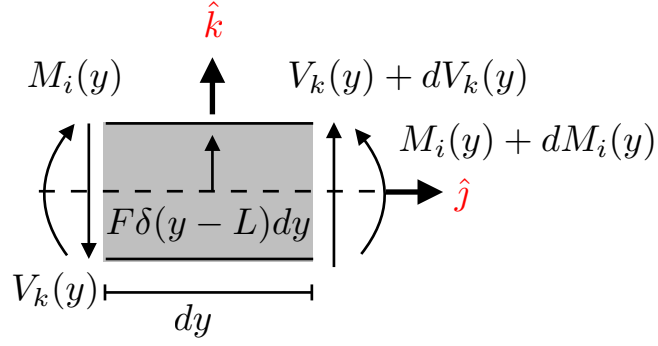


Figure A.5: Shear load,  $V_k(y)$ , and bending moment,  $M_i(y)$ , diagram for an infinitesimal segment of the cantilevered beam.  $F\delta(y - L)dy$  is a concentrated load treated as a distributed force. The delta function ensures that the load only takes effect at  $y = L$

These equilibrium equations can be combined to create

$$\frac{d^2 M_i(y)}{dy^2} = \frac{dV_k(y)}{dy} = -F\delta(y - L). \quad (\text{A.26})$$

Substituting the area second moment, elastic modulus, and the beam curvature for the bending moment yields the following fourth order ordinary differential equation:

$$\frac{d^2}{dy^2} \left[ EI_{11}^c \frac{d^2 \bar{u}_k(y)}{dy^2} \right] = -F\delta(y - L). \quad (\text{A.27})$$

The elastic modulus will be treated as a constant and the area second moment is independent of  $y$ , allowing it to be pulled through the derivative:

$$EI_{11}^c \frac{d^4 \bar{u}_k(y)}{dy^4} = -F\delta(y - L). \quad (\text{A.28})$$

The solution to this differential equation involves integration constants that must be obtained using boundary conditions. The boundary conditions are a consequence of the supports and loads distributed throughout the beam. For a cantilevered beam with a concentrated load on the free end, the boundary conditions are

$$\bar{u}_k(y)|_{y=0} = 0, \quad \left. \frac{d\bar{u}_k(y)}{dy} \right|_{y=0} = 0, \quad \left. \frac{d^2 \bar{u}_k(y)}{dy^2} \right|_{y=L} = 0. \quad (\text{A.29})$$

The first boundary condition comes from the assumption that the fixed end of the cantilever cannot move. The second boundary condition states that there must be zero slope at the fixed end, which is a consequence of the first boundary condition. The third boundary condition states that the bending moment disappears at the loaded end. The solution to this differential equation is

$$\bar{u}_k(y) = \frac{F}{6EI_{11}^c} (3Ly^2 - y^3). \quad (\text{A.30})$$

Substituting in the area second moment of inertia and evaluating the displacement at the loaded end of the cantilever yields

$$\bar{u}_k(y = L) = \frac{4FL^3}{Ewt^3}. \quad (\text{A.31})$$

This equation can be used to determine the amount of force applied to an AFM probe for a known probe tip displacement.

### Dynamic Solution

Dynamic solutions to the static beam equation can be modeled by choosing time-dependent loading functions. For example, the free vibration of a cantilever beam can be modeled by introducing the load function

$$F(y, t) = \mu \frac{\partial^2 \bar{u}_k(y, t)}{\partial t^2}, \quad (\text{A.32})$$

where  $\mu$  is the linear mass density of the beam.<sup>1</sup> With the substitution of this time-dependent loading, the beam equation, Eq. (A.28), becomes a partial differential equation:

$$EI_{11}^c \frac{\partial^4 \bar{u}_k(y, t)}{\partial y^4} = -\mu \frac{\partial^2 \bar{u}_k(y, t)}{\partial t^2}. \quad (\text{A.33})$$

Dividing by the linear mass density yields

$$\alpha^2 \frac{\partial^4 \bar{u}_k(y, t)}{\partial y^4} = -\frac{\partial^2 \bar{u}_k(y, t)}{\partial t^2}, \quad (\text{A.34})$$

where  $\alpha^2 = EI_{11}^c/\mu$ . This equation is a coupled partial differential equation that is fourth order in space and second order in time. However, using separation of variables, we transform the partial differential equation into two ordinary differential equations. If we let  $\bar{u}_k(y, t) = Z(y)T(t)$ , then

$$\alpha^2 \frac{\partial^4 Z(y)T(t)}{\partial y^4} = -\frac{\partial^2 Z(y)T(t)}{\partial t^2}. \quad (\text{A.35})$$

We now isolate each variable on separate sides of the equation. The partial derivatives become total derivatives, the solutions of which must be a constant. Let this constant be  $\omega^2$  such that

$$\frac{\alpha^2}{Z(y)} \frac{d^4 Z(y)}{dy^4} = -\frac{1}{T(t)} \frac{d^2 T(t)}{dt^2} = \omega^2. \quad (\text{A.36})$$

---

<sup>1</sup>It is important to note that the linear mass density of the beam results in an effective mass causing the mathematics to deviate from the massless spring model.

### Temporal Solution

The result for the time-dependent expression is the classical harmonic oscillator:

$$\frac{d^2T(t)}{dt^2} = -\omega^2T(t), \quad (\text{A.37})$$

$$T(t) = C_0 \cos(\omega t) + C_1 \sin(\omega t). \quad (\text{A.38})$$

The constants  $C_0$  and  $C_1$  can be solved for given the initial position and velocity of the beam. If we treat  $Z(y)$  as if it carries the information regarding the shape of the beam, then we can treat  $T(t)$  as the amplitude of the deflection of the beam as a function of time. This treatment effectively normalizes  $T(t)$  between  $-1$  and  $1$ , forcing the integration constant  $C_0 = 1$ . If we setup the problem with the beam having a slightly bent shape and zero initial velocity, then

$$C_1 = 0, \quad (\text{A.39})$$

and we can rewrite Eq. (A.38) as

$$T(t) = \cos(\omega t). \quad (\text{A.40})$$

### Spatial Solution

For the solution of the position-dependent expression, we first set  $\beta^4 = \omega^2/\alpha^2$ :

$$\frac{d^4Z(y)}{dy^4} = \beta^4Z(y). \quad (\text{A.41})$$

Here, the solution can be exponential or sinusoidal, so we need a linear combination of all possible solutions. This yields

$$Z(y) = C_2e^{i\beta y} + C_3e^{-i\beta y} + C_4e^{\beta y} + C_5e^{-\beta y}, \quad (\text{A.42})$$

where the constants  $C_2$ ,  $C_3$ ,  $C_4$ , and  $C_5$  can be solved for with the boundary conditions. This equation becomes easier to solve if we cast it in its trigonometric form:

$$Z(y) = C_2 \sin(\beta y) + C_3 \cos(\beta y) + C_4 \sinh(\beta y) + C_5 \cosh(\beta y). \quad (\text{A.43})$$

Before we discuss the boundary conditions, it will be useful to calculate the first three derivatives of this equation:

$$\frac{dZ(y)}{dy} = \beta [C_2 \cos(\beta y) - C_3 \sin(\beta y) + C_4 \cosh(\beta y) + C_5 \sinh(\beta y)], \quad (\text{A.44})$$

$$\frac{d^2Z(y)}{dy^2} = \beta^2 [-C_2 \sin(\beta y) - C_3 \cos(\beta y) + C_4 \sinh(\beta y) + C_5 \cosh(\beta y)], \quad (\text{A.45})$$

$$\frac{d^3Z(y)}{dy^3} = \beta^3 [-C_2 \cos(\beta y) + C_3 \sin(\beta y) + C_4 \cosh(\beta y) + C_5 \sinh(\beta y)]. \quad (\text{A.46})$$

For completeness, it is shown that the fourth derivative is equal to  $\beta^4 Z(y)$ :

$$\begin{aligned} \frac{d^4 Z(y)}{dy^4} &= \beta^4 [C_2 \sin(\beta y) + C_3 \cos(\beta y) + C_4 \sinh(\beta y) + C_5 \cosh(\beta y)] \\ &= \beta^4 Z(y). \end{aligned} \quad (\text{A.47})$$

The clamped end of the cantilever is fixed in place and cannot undergo any displacement. Since it cannot undergo any displacement, it stands to reason that it also cannot have a first derivative either. Therefore

$$Z|_{y=0} = 0, \quad (\text{A.48})$$

and

$$\left. \frac{dZ}{dy} \right|_{y=0} = 0. \quad (\text{A.49})$$

Combining Eqs. (A.48) and (A.43) results in

$$C_3 = -C_5, \quad (\text{A.50})$$

and combining Eqs. (A.49) and (A.44) results in

$$C_2 = -C_4. \quad (\text{A.51})$$

At the free end of the beam, both the bending moment and the shear force must disappear:

$$\left. \frac{d^2 Z}{dy^2} \right|_{y=L} = 0, \quad (\text{A.52})$$

and

$$-EI_{11}^c \left. \frac{d^3 Z}{dy^3} \right|_{y=L} = 0. \quad (\text{A.53})$$

Combining Eqs. (A.52) and (A.45) results in

$$C_4 \sin(\beta L) + C_5 \cos(\beta L) + C_4 \sinh(\beta L) + C_5 \cosh(\beta L) = 0, \quad (\text{A.54})$$

and combining Eqs. (A.53) and (A.46) results in

$$C_4 \cos(\beta L) - C_5 \sin(\beta L) + C_4 \cosh(\beta L) + C_5 \sinh(\beta L) = 0. \quad (\text{A.55})$$

By rearranging Eq. (A.54) we find

$$C_4 = -C_5 \frac{\cos(\beta L) + \cosh(\beta L)}{\sin(\beta L) + \sinh(\beta L)}. \quad (\text{A.56})$$

Lastly, by rearranging Eq. (A.55) we obtain the following

$$C_4 = C_5 \frac{\sin(\beta L) - \sinh(\beta L)}{\cos(\beta L) + \cosh(\beta L)}. \quad (\text{A.57})$$

Substituting Eqs. (A.50), (A.51), and (A.56) into Eq. (A.43) yields

$$Z(y) = C_5 \left[ \left( \sinh(\beta y) - \sin(\beta y) \right) \left[ \frac{\sin(\beta L) - \sinh(\beta L)}{\cos(\beta L) + \cosh(\beta L)} \right] + \left( \cosh(\beta y) - \cos(\beta y) \right) \right]. \quad (\text{A.58})$$

To solve for the final unknown constant  $C_5$ , we set the static beam equation (Eq. (A.30)) equal to the dynamic beam equation (Eq. (A.58)) at  $t = 0$  and  $y = L$ . Therefore,

$$C_5 = \frac{FL^3 [\cos(\beta L) + \cosh(\beta L)]}{3EI_{11}^c [\cosh^2(\beta L) - \cos^2(\beta L) - (\sin(\beta L) - \sinh(\beta L))^2]}. \quad (\text{A.59})$$

The trigonometric portion of this equation reduces to  $1/2$  and a factor of  $\pm 1$  depending on the mode number  $n$ :

$$C_n = \frac{FL^3}{6EI_{11}^c} (-1)^n, \quad n \in \mathbb{N}. \quad (\text{A.60})$$

The natural modes of the cantilever are obtained by combining Eqs. (A.56) and (A.57),

$$-\frac{\cos(\beta L) + \cosh(\beta L)}{\sin(\beta L) + \sinh(\beta L)} = \frac{\sin(\beta L) - \sinh(\beta L)}{\cos(\beta L) + \cosh(\beta L)}. \quad (\text{A.61})$$

Multiplying by the denominators results in

$$\cos^2(\beta L) + 2\cos(\beta L)\cosh(\beta L) + \cosh^2(\beta L) = -\sin^2(\beta L) + \sinh^2(\beta L). \quad (\text{A.62})$$

Rearranging this equation yields

$$[\sinh^2(\beta L) - \cosh^2(\beta L)] = [\sin^2(\beta L) + \cos^2(\beta L)] + 2\cos(\beta L)\cosh(\beta L). \quad (\text{A.63})$$

Simplification leaves

$$\cos(\beta L)\cosh(\beta L) + 1 = 0. \quad (\text{A.64})$$

The vibrational modes can be determined by plotting Eq. (A.64) and looking for the locations where the curve crosses the x-axis. The first four vibrational modes are

$$\beta_1 L = 1.875, \quad (\text{A.65})$$

$$\beta_2 L = 4.6941, \quad (\text{A.66})$$

$$\beta_3 L = 7.8548, \quad (\text{A.67})$$

$$\beta_4 L = 10.9955. \quad (\text{A.68})$$

Substituting Eqs. (A.65)–(A.68) into Eq. (A.59) and then substituting Eq. (A.59) into Eq. (A.58) enables us to draw the shapes of the first four modes (see Fig. A.6).

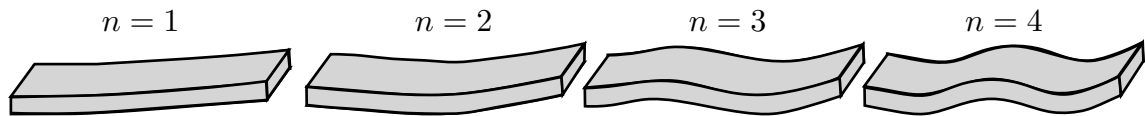


Figure A.6: Schematic of the first four vibrational modes of a clamped cantilever.

### Effective Mass Consideration

The methods of this section have been adapted from chapter 2.6 of Voigtländer's *Scanning Probe Microscopy* [88]. Until now, the entire derivation of a cantilever's motion has assumed an idealized system with a massless cantilever and a mass  $m$  located at the end. The real situation is such that the cantilever will have its mass distributed throughout its length. The concept of effective mass takes this continuous mass distribution and treats it as if it is concentrated at the end of the cantilever. For this derivation, it is assumed that the mass is distributed homogeneously along the cantilever's length. We can calculate the kinetic energy  $T(y)$  of a point along the cantilever system using the mass  $m_{cant}(y)$  and velocity  $v(y)$  of that point:

$$T(y) = \frac{1}{2}m_{cant}(y)v^2(y). \quad (\text{A.69})$$

The kinetic energy of an infinitesimal segment of mass  $dm$  can be found by taking the derivative of  $T(y)$  with respect to  $m_{cant}(y)$ :

$$dT(y) = \frac{1}{2}v^2(y)dm_{cant}. \quad (\text{A.70})$$

Because of the homogeneous distribution of mass, the infinitesimal segment of cantilever mass  $dm_{cant}$  can be related to an infinitesimal segment of cantilever length  $dy$  by the relationship

$$dm_{cant} = \frac{m_{cant}}{L}dy. \quad (\text{A.71})$$

The velocity distribution along the beam is proportional to the deflection  $\bar{u}_k(y)$ , Eq. (A.30):

$$v(y) = c\bar{u}_k(y) = c\frac{2F}{Ewt^3}(3Ly^2 - y^3). \quad (\text{A.72})$$

The constant of proportionality  $c$  is determined from the condition  $v(y = L) = v_{max}$ :

$$c = \frac{Ewt^3}{4FL^3}v_{max}. \quad (\text{A.73})$$

We can now substitute Eq. (A.73) into Eq. (A.72) and then substitute Eqs. (A.72) and (A.71) into Eq. (A.70) and integrate to obtain

$$T = \frac{1}{2} \int_0^L \frac{m_{cant}}{L} \left(\frac{v_{max}}{2L^3}\right)^2 (3Ly^2 - y^3)^2 dy = \frac{1}{2} \left(\frac{33}{140}m_{cant}\right)v_{max}^2 = \frac{1}{2}m_{eff}v_{max}^2. \quad (\text{A.74})$$

In this equation  $m_{eff}$  is the effective mass of the cantilever. This effective mass must be used in the equation of motion and all subsequently derived expressions such as the natural oscillator frequency

$$\omega_0 = \sqrt{\frac{k}{m_{eff}}}. \quad (\text{A.75})$$

It is important to note that if an additional, point-like, mass  $M$  is added to the tip of the cantilever, then the effective mass becomes  $m_{eff} = \left(\frac{33}{140}m_{cant} + M\right)$ .



# Appendix B

## Derivation of Atomic Force Microscope Equations

The most common method of detection for AFMs is the beam deflection method. This involves focusing a collimated laser beam onto the end of a cantilever and detecting the reflection with a position-sensitive detector. This type of detector contains two semicircular photodiodes separated by a small distance, as seen in Fig. B.1. By initially aligning the reflected laser beam onto the center of the detector, the difference in optical signals  $S_A - S_B$  measured by the two photodiodes,  $A$  and  $B$ , is proportional to the displacement of the center of the beam  $\Delta q$  relative to the axis splitting the photodiodes.

### Sensitivity of the Beam Deflection Method

This section follows the methods of chapter 12.3 of Bert Voigtländer's *Scanning Probe Microscopy* [89]. Prior to bending the cantilever, the position-sensitive detector is aligned such that the reflected laser beam illuminates the center of the detector, yielding an output of 0 V. Displacing the tip of the cantilever by an amount  $\Delta z$  causes the cantilever to bend by an amount  $\theta$ . Since this increases the angle of incidence of the laser beam by the amount  $\theta$ , the angle of reflection also increases by the same amount. Therefore, the angular deflection of the laser beam is twice the angular deflection of the cantilever. Due to the geometry of the optical setup, the displacement of the laser beam along the detector is

$$\Delta q = 2\theta L_{det}. \quad (\text{B.1})$$

A relationship between the cantilever displacement  $\Delta z$  and the deflection angle  $\theta$  can be arrived at by combining the solution to the static beam equation, Eq. A.30 derived in Appendix A,

$$\Delta z(y) = \bar{u}_k(y) = \frac{F}{6EI_{11}^c} (3Ly^2 - y^3), \quad (\text{B.2})$$

with its first derivative with respect to  $y$ ,

$$\theta(y) = \frac{d\bar{u}_k(y)}{dy} = \frac{F}{6EI_{11}^c} (6Ly - 3y^2), \quad (\text{B.3})$$

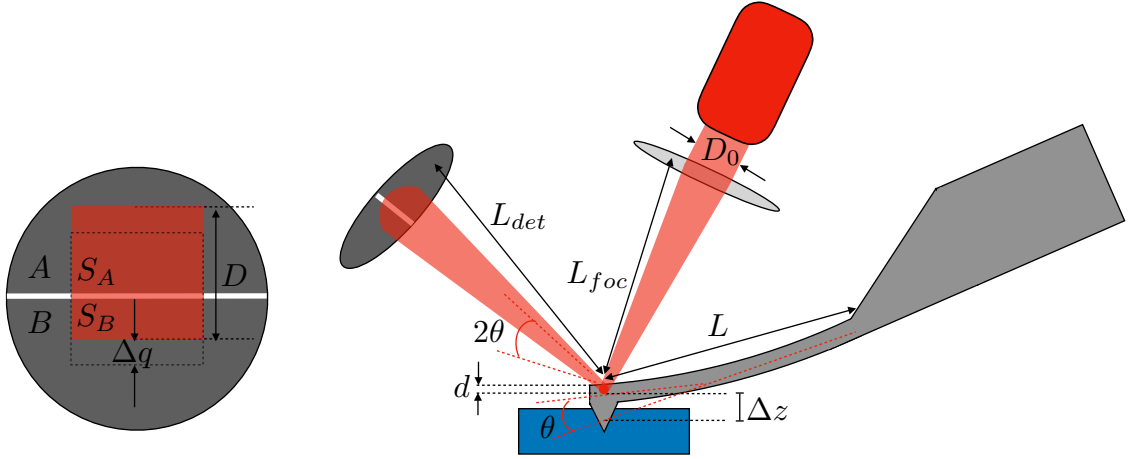


Figure B.1: Schematic of the beam deflection method. The distances shown are necessary to calculate the sensitivity of the measurement.

and setting  $y = L$ ,

$$\theta = \frac{3}{2L} \Delta z. \quad (\text{B.4})$$

The laser beam is initially collimated to a diameter  $D_0$  and is focused by a lens of focal length  $L_{foc}$  onto the end of the cantilever. The diffraction-limited spot size of the focused beam is

$$d = \frac{4\lambda L_{foc}}{\pi D_0}. \quad (\text{B.5})$$

Assuming the beam width at the focal point is just smaller than the width of the cantilever, the width of the beam at the photodiode will be diffraction-limited to

$$D = \frac{4\lambda L_{det}}{\pi d}. \quad (\text{B.6})$$

For the sake of simplicity, it is assumed that the photodiode is uniformly irradiated over the entire beam spot and also that the shape of the beam spot is a square of side  $D$ . The power per unit area illuminating the photodiode is  $S_{area}$  and it is assumed that the entire beam width is contained within the area of the photodiode such that the total laser power is  $S_0 = S_{area} D^2$ . When the laser beam is displaced by the amount  $\Delta q$ , the detector experiences a difference signal of

$$S_A - S_B = S_{area} 2\Delta q D. \quad (\text{B.7})$$

Substituting Eqs. (B.1), (B.4), and (B.6) into Eq. (B.7) yields

$$S_A - S_B = \frac{S_0}{D^2} 4\theta L_{det} D = 6 \frac{S_0 L_{det} \Delta z}{LD} = \frac{3\pi S_0 d \Delta z}{2 \lambda L}. \quad (\text{B.8})$$

Each photodiode produces a photocurrent  $I$ , in units of Amperes, proportional to the incident laser power and the responsivity  $R$  of the diode, in units of Amperes per Watt:

$$I_A - I_B = R(S_A - S_B) = \frac{3\pi S_0 R d}{2\lambda L} \Delta z. \quad (\text{B.9})$$

There are two outputs from the position-sensitive detector. The first is a voltage  $V_{diff}$  that is proportional to product of the difference in photocurrents  $I_A - I_B$  and the gain  $G$  of the transimpedance amplifier, in units of kilovolts per Ampere:

$$V_{diff} = G(I_A - I_B) = GR(S_A - S_B). \quad (\text{B.10})$$

The second is a voltage  $V_{sum}$  that is proportional to the product of the total sum of photocurrents  $I_A + I_B$  and the gain  $G$  of the transimpedance amplifier:

$$V_{sum} = G(I_A + I_B) = GR(S_A + S_B) = GR S_0. \quad (\text{B.11})$$

To remove any fluctuations due to the laser power, the difference is normalized by the sum:

$$V_{norm} = \frac{V_{diff}}{V_{sum}} = \frac{(S_A - S_B)}{S_0} = \frac{3\pi d}{2\lambda L} \Delta z = S_{sensor} \Delta z. \quad (\text{B.12})$$

It can be seen from Eq. (B.12) that the detection sensitivity  $S_{sensor}$  can be increased by using: a shorter wavelength  $\lambda$  of light, a shorter cantilever  $L$ , or by increasing the focused spot size  $d$ . It is important to note that neither the distance from the cantilever to the photodiode nor the distance from the cantilever to the lens are in this final equation.

Although we have calculated an approximate analytical form for the detection sensitivity, the numerous assumptions made and the many parameters involved suggest experimental measurement is the best approach.

### Calibration of Atomic Force Microscope

The methods described here adopt the formalism of chapter 12.5.1 of Bert Voigtländer's *Scanning Probe Microscopy* [89]. The beam deflection method is relatively straightforward and ultimately allows a force  $F$  to be measured via the deflection  $\Delta z$  of a cantilever. The relationship between the force and the deflection is Hooke's law  $F = -K\Delta z$ . There are two calibrations that must be performed to reliably use the beam deflection method. First, the deflection  $\Delta z$  of the cantilever is not directly measured with this method. A normalized difference signal  $V_{norm}$  from the position-sensitive detector is what is actually measured, although it is proportional to the displacement of the cantilever through Eq. (B.12). The sensitivity of the sensor  $S_{sensor}$ , being the constant of proportionality, is measured by plotting the equation  $V_{sensor}$  versus  $\Delta z$ , while the sample is in contact with the AFM probe, and extracting the slope. The second calibration that must be performed is of the stiffness coefficient  $k$ . AFM probes are often provided with large uncertainties in the stiffness coefficient, stemming from the fact that thickness of the cantilever carries the largest relative uncertainty and the uncertainty in the thickness has the largest effect on the uncertainty of the stiffness coefficient.

Experimentally determining the sensitivity  $S_{sensor}$  requires knowledge of the displacement  $\Delta z$  of the cantilever. This step is typically performed using piezoelectric nanopositioners with a known piezoelectric constant  $C_{piezo}$ . This constant allows for precise positioning of the sample through the application of a known voltage to the piezo,

$$\Delta z_{piezo} = C_{piezo} V_{piezo}. \quad (\text{B.13})$$

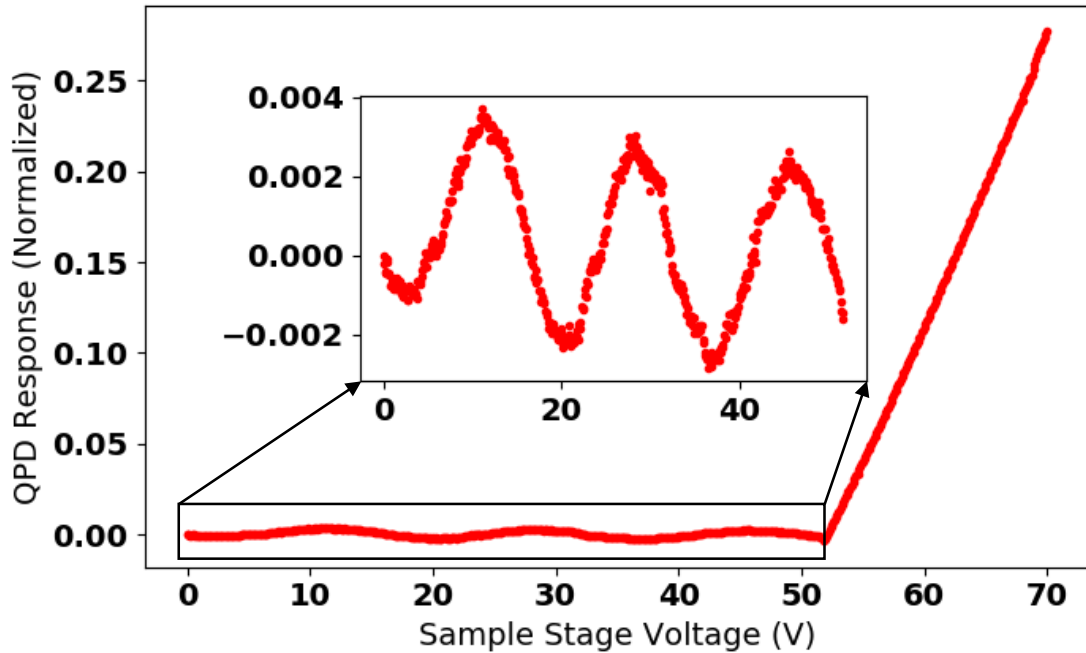


Figure B.2: Calibration curve for the sensitivity  $S_{sensor}$  of the position detector. **(Inset)** The boxed region of the main figure is blown up. In the non-contact regime an interference pattern is observed which is used to calibrate the piezoelectric constant of the nanopositioners.

In the case of my setup, the piezoelectric constant was not known and therefore required a third calibration step. To the benefit of the measurement technique, an oscillatory pattern was identified in the plots of normalized sensor voltage  $V_{norm}$  versus applied nanopositioner voltage  $V_{piezo}$  in the non-contact regime. This oscillatory pattern is attributed to the interference of light reflected from the cantilever with light reflected from the sample surface. By analyzing the data in Fig. B.2, two of the three calibrations can be accomplished from a single data set.

To utilize the interference pattern observed in the non-contact regime, a mathematical model must be created that accounts for the optical path difference of the light reflected from the two surfaces. Figure B.3 shows a schematic of the optical path of the laser beam during the beam deflection measurement. As the sample approaches the AFM probe, the path length difference  $\sqrt{2}d$  causes the interference pattern at the detector to shift. If one looks closely at Fig. B.3 b), it is seen that, in this simplified example, the pattern shifts from one where there are two bright fringes on the bottom detector and three bright fringes on the top (bottom image) to one where the number of fringes on each detector has flipped (top image).

The fringes seen in the interference pattern are a result of the superposition of two electromagnetic waves. One wave emanates from the surface of the AFM probe  $E_{tip}$ , and another from the sample surface  $E_{sample}$ . To determine the relationship between the sample displacement and the detector signal, we must examine the superposition of these two

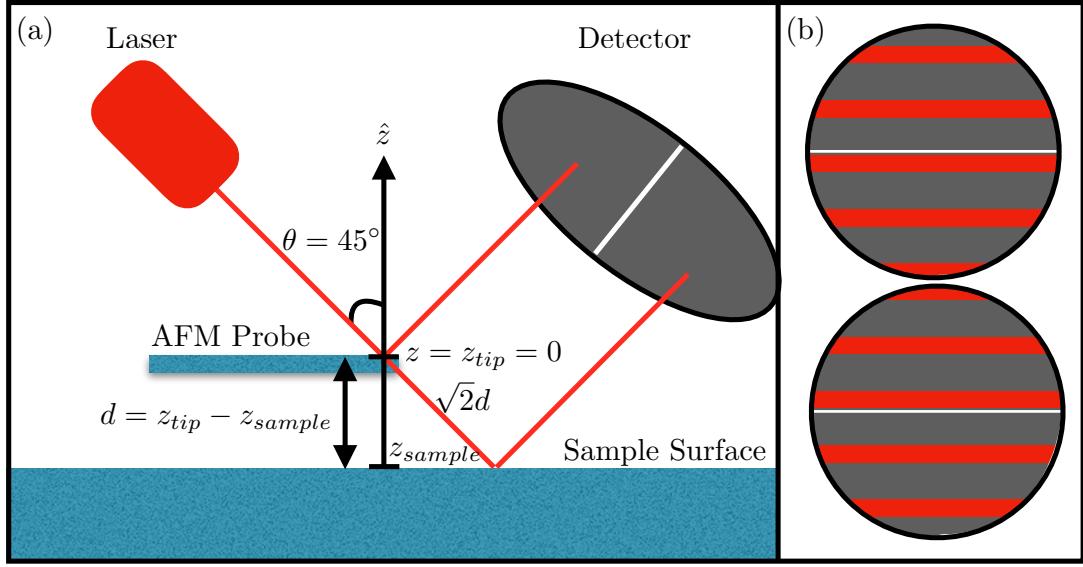


Figure B.3: (a) Schematic showing the optical path of the laser beam as it reflects off the two surfaces. The laser beam reflected from the cantilever is initially centered on the detector when the sample is far from contact. (b) As the sample approaches, the change in the path length difference  $\sqrt{2}d$  causes a shift in the interference pattern at the detector. It is important to note that the oscillations in Fig. B.2 are a result of the shifting of this interference pattern as a function of  $z_{sample}$ .

electromagnetic waves. Let us define the electric fields of these electromagnetic waves as plane waves such that

$$E_{tip} = E_0 e^{i(\omega t - kL_{tip})} \text{ and } E_{sample} = E_0 e^{i(\omega t - kL_{sample} - k\sqrt{2}d)}, \quad (\text{B.14})$$

where  $E_0$  is the magnitude of the electric field,  $\omega$  is the angular frequency of the wave,  $k$  is the wave number, and  $L_{tip}$  and  $L_{sample}$  are the path lengths from the detector to the AFM probe tip and the sample, respectively. At the detector these two electric fields are summed:

$$E = E_{tip} + E_{sample} = E_0 e^{i\omega t} \left( e^{-ikL_{tip}} + e^{-ikL_{sample} - ik\sqrt{2}d} \right). \quad (\text{B.15})$$

The electric field is not what is sensed by the detector, but rather the intensity of light:

$$I \propto |E^2| = |EE^*| = E_0^2 \left( 2 + e^{-ik(L_{tip} - (L_{sample} + \sqrt{2}d))} + e^{ik(L_{tip} - (L_{sample} + \sqrt{2}d))} \right). \quad (\text{B.16})$$

Trigonometric identities simplify this to

$$I \propto 4E_0^2 \cos^2 \left( \frac{k}{2} (L_{tip} - (L_{sample} + \sqrt{2}d)) \right). \quad (\text{B.17})$$

Due to the geometry of the setup, the two lengths  $L_{tip}$  and  $L_{sample}$  are equivalent and Eq. (B.17) simplifies to

$$I \propto 4E_0^2 \cos^2 \left( \frac{\sqrt{2}kd}{2} \right). \quad (\text{B.18})$$

As the sample approaches the tip, but prior to making contact, the intensity of light at the detector will oscillate with maxima occurring anytime the argument of the cosine in Eq. (B.18) is an integer multiple of  $\pi$ :

$$\frac{\sqrt{2}kd}{2} = n\pi, \text{ where } n \in \mathbb{N}. \quad (\text{B.19})$$

Substituting  $k = 2\pi/\lambda$  for the wave vector and solving for  $d$  yields

$$d = \frac{n\lambda}{\sqrt{2}}. \quad (\text{B.20})$$

From Fig. B.3 we see that

$$d = z_{tip} - z_{sample}, \quad (\text{B.21})$$

and we can set  $z_{tip} = 0$  because the AFM tip is stationary at this time. Therefore, Eq. (B.20) shows that  $\Delta n = 1$  indicates a movement of the sample by the amount

$$|z_{sample}| = \frac{\lambda}{\sqrt{2}}. \quad (\text{B.22})$$

Fitting the oscillatory pattern in Fig. B.4 to an equation with the form shown in Eq. (B.18) results in an accurate measure of the piezoelectric constant  $C_{piezo}$ .

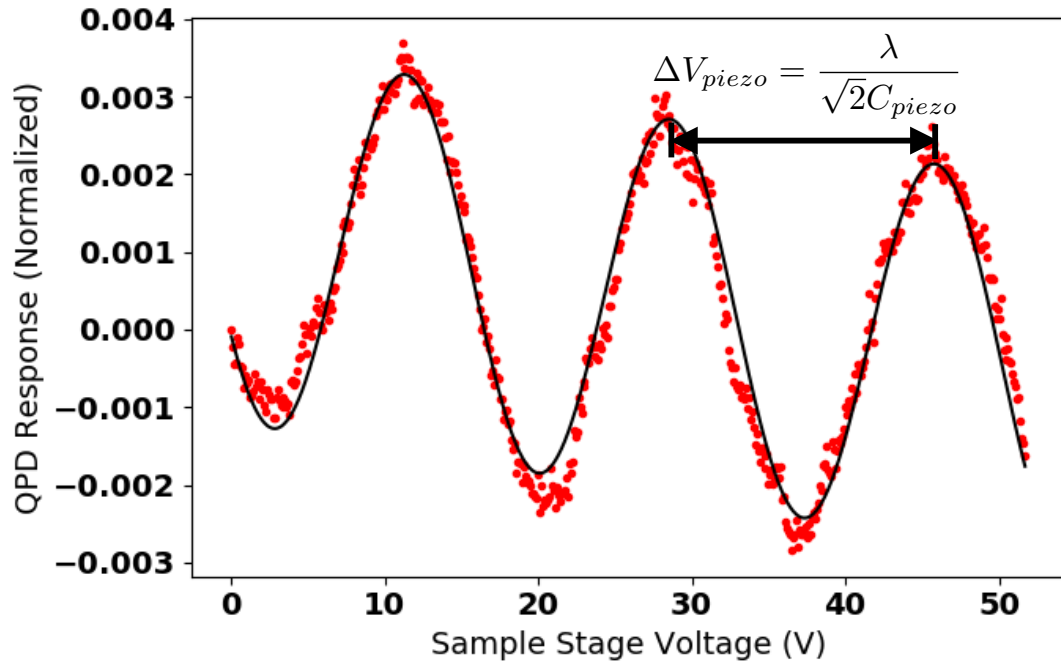


Figure B.4: The voltage difference between local maxima of the interference pattern is proportional to the wavelength of light  $\lambda$  and inversely proportional to the piezoelectric constant  $C_{piezo} = (36 \pm 1) \text{ nm/V}$ .

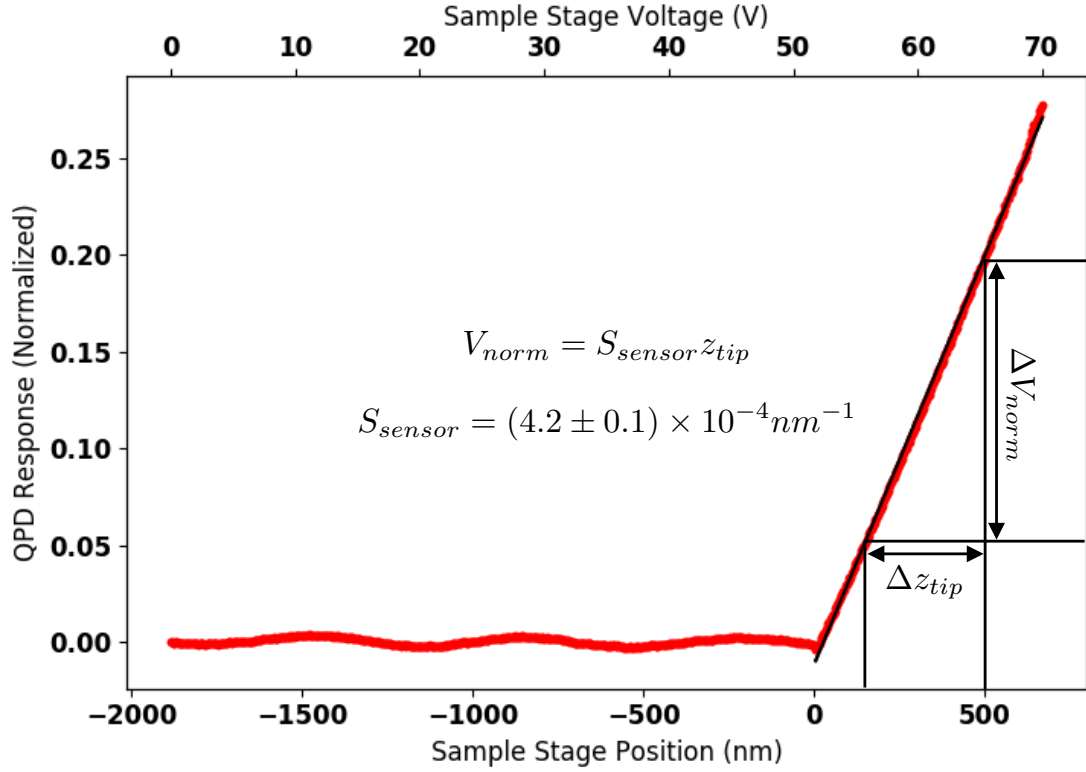


Figure B.5: With the horizontal axis now in units of distance, the position-sensitive detector can be calibrated to units of distance as well. This measurement is made against a sample with negligible elasticity, e.g. a silicon wafer, so that the position of the sample is equal to the position of the tip  $z_{sample} = z_{tip}$ .

Now the voltage applied to the piezoelectric nanopositioning stages can be converted into the  $z$ -position of the sample using Eq. (B.13). Figure B.5 shows the graph after converting the  $x$ -axis. This plot can now be used to acquire the sensitivity  $S_{sensor}$  by taking the inverse of the slope of the straight line corresponding to the contact regime. At this point the position-sensitive detector and piezoelectric nanopositioning stages have been fully calibrated. The final plot, Fig. B.6, shows the position of the tip  $z_{tip}$  as a function of the position of the sample  $z_{sample}$ .

At this point it is typical to measure the stiffness coefficient  $k$  of the AFM probe by performing one of the calibration methods described in the literature [90, 91, 92]. The most straight forward method for arriving at the stiffness coefficient of the AFM probe is by measuring the dimensions of the cantilever and its resonant frequency and then calculating its stiffness through the equation

$$k = m_{eff}\omega^2 = 0.2357Lwt\rho\omega^2. \quad (\text{B.23})$$

In this equation, 0.2357 is the effective mass constant derived at the end of Appendix A,  $L$ ,  $w$ , and  $t$  are the length, width, and thickness,  $\rho$  is the mass density, and  $\omega$  is the resonant

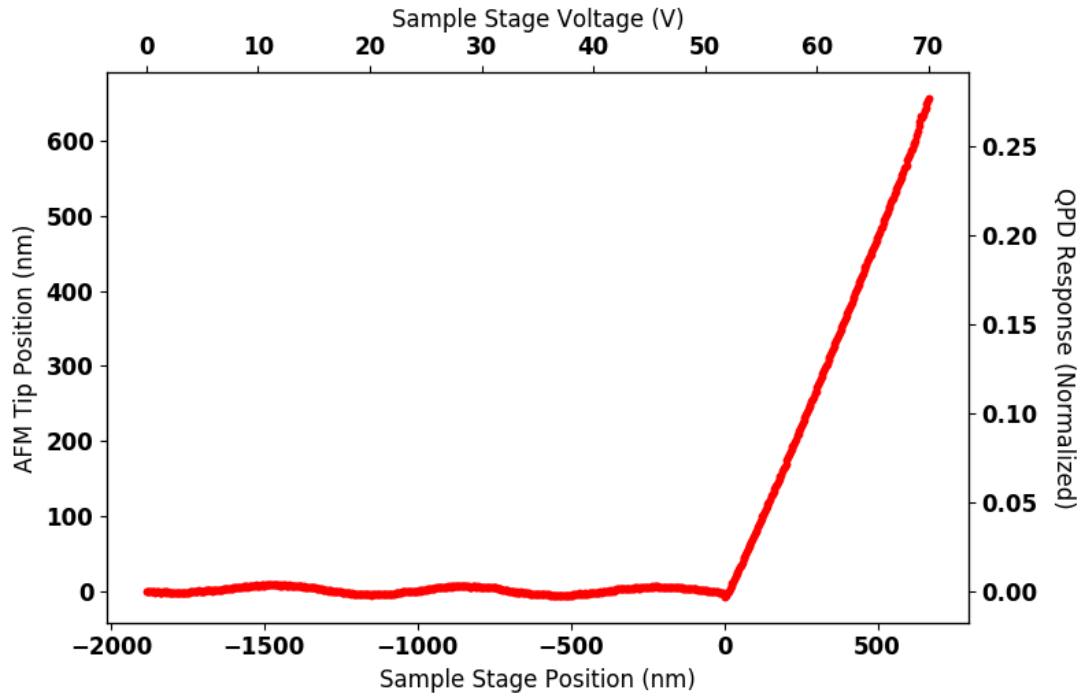


Figure B.6: Fully calibrated setup showing a plot of  $z_{tip}(z_{sample})$ .

frequency of the cantilever. The plain view dimensions,  $L$  and  $w$ , are simple enough to measure with a microscope setup; however, the thickness  $t$  of the cantilever typically requires the use of a scanning electron microscope to get accurate measurements. Furthermore, the density  $\rho$  of the cantilever may not be assumed to be a constant throughout because most AFM probes are manufactured with a highly reflective metal coating on the top surface [93]. For our studies, the AFM probes are manufactured as monolithic silicon, removing the difficulties involved with density gradients.



# Appendix C

## Derivation of Spectrometer Equations

The methods described here adopt the formalism of the TriVista System User Manual [94]. In this chapter the diffraction grating equation will be combined with the spectrometer geometry, as well as entrance and exit slit dimensions, to arrive at a spectral resolution for the instrument. As with other techniques that utilize wave interference, a diffraction grating will exhibit constructive interference when the path length difference between two waves are an integer multiple apart (see Fig. C.1). With a diffraction grating, the diffraction occurs due to small grooves etched into the surface of a reflective or transmissive optical flat with spacings on the order of the wavelength of light to be diffracted. Fig. C.1 shows that the path length difference can be calculated to be

$$m\lambda = d(\sin \alpha + \sin \beta_n), \quad (\text{C.1})$$

where  $m$  is the order number,  $\lambda$  is the wavelength of light,  $d$  is the distance between facets in the diffraction grating, and  $\alpha$  and  $\beta_n$  are the incident and diffracted angles of the rays of light. Inside of a spectrometer, blazed diffraction gratings are typically used. These blazed diffraction gratings will have a series of facets patterned onto the surface of the grating to

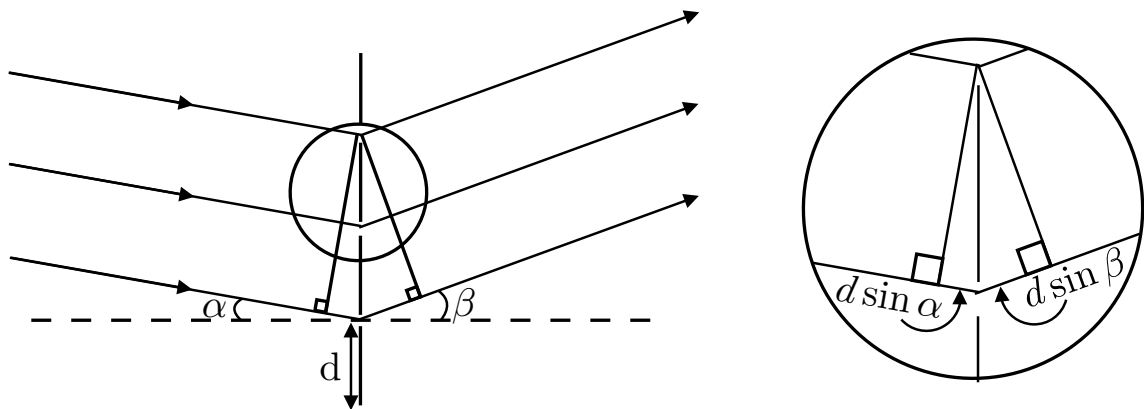


Figure C.1: Schematic showing the interference of parallel waves upon transmission through a diffraction grating.

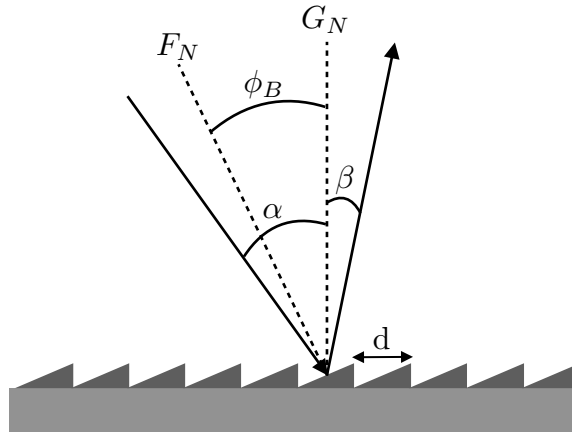


Figure C.2: Schematic of a blazed diffraction grating for use in a spectrometer system.

act as the grooves. Fig. C.2 shows a schematic of a reflective blazed diffraction grating for a spectrometer. In Fig. C.2, the blaze angle  $\phi_B$  is the angle between the grating normal  $G_N$  and the facet normal  $F_N$ . This type of grating has an optimized geometry when operated in Littrow condition ( $\alpha = \beta_n = \phi_B$ ) which will retro-reflect the  $m = 0$  order diffracted beam back along the incident beam. This geometry maximizes the amount of power diffracted in the higher order modes,  $m > 0$ .

By considering the diffraction of the grating combined with a collimating and a focusing mirror inside of a spectrometer system, we can calculate the dispersion as well as the spectral resolution of the instrument. Consider Fig. C.3, where the geometry of the spectrometer system is shown in detail. By adopting a sign convention that gives angles with a counterclockwise rotation relative to the grating normal  $G_N$  a positive value, the constant inclusion angle can be calculated as

$$\gamma = \beta_c - \alpha = \text{constant.} \tag{C.2}$$

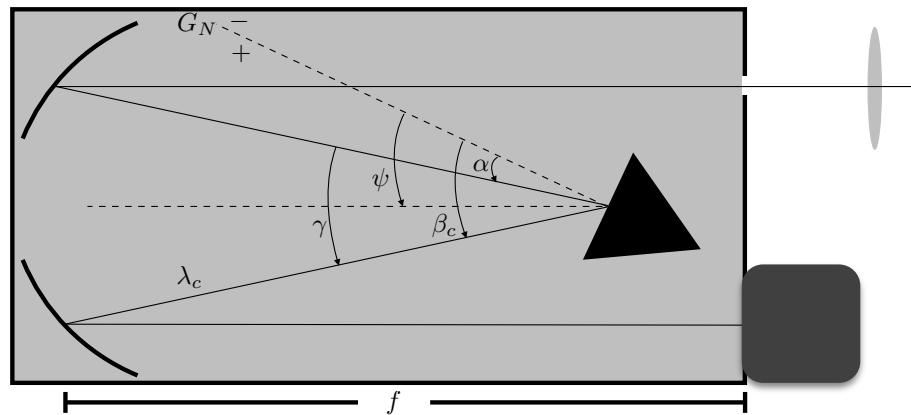


Figure C.3: Geometry of a spectrometer system of focal length  $f$ , incident angle  $\alpha$ , diffracted angle  $\beta_c$  of the center wavelength, inclusion angle  $\gamma$ , and grating angle  $\psi$ .

With this constraint, the incident angle  $\alpha$  and central diffracted angle  $\beta_c$  can be calculated as a function of the grating angle  $\psi$ :

$$\alpha = \psi - \frac{\gamma}{2}, \quad (\text{C.3})$$

and

$$\beta_c = \psi + \frac{\gamma}{2}. \quad (\text{C.4})$$

Combining Eqs. (C.1), (C.3), and (C.4) allows us to calculate the grating angle  $\psi$  at which a certain wavelength will hit the center pixel of a CCD at the exit plane of the spectrometer. First we must use a sum-to-product trigonometric identity to calculate the wavelength of the diffracted beam as a function of the grating  $\psi$  and inclusion  $\gamma$  angles,

$$\begin{aligned} m\lambda_c &= d(\sin(\psi - \frac{\gamma}{2}) + \sin(\psi + \frac{\gamma}{2})) \\ &= 2d \sin \psi \cos \frac{\gamma}{2}. \end{aligned} \quad (\text{C.5})$$

Now, we can rearrange Eq. (C.5) to solve for the grating angle  $\psi$ :

$$\psi = \arcsin \frac{m\lambda_c}{2d \cos \frac{\gamma}{2}}. \quad (\text{C.6})$$

If we consider the path of a wavelength  $\lambda_n$  which is not at the center wavelength, we can calculate the diffracted angle  $\beta_n$  for this wavelength (see Fig. C.4). The displacement of the two beams  $\Delta y$ ,  $\lambda_c$  and  $\lambda_n$ , can be expressed as the number of pixels  $n - n_c$  displaced from the center pixel multiplied by the width of a single pixel  $w_p$ ,

$$\Delta y = (n - n_c)w_p. \quad (\text{C.7})$$

Using geometry, this displacement can be calculated as

$$\tan \delta = \frac{\Delta y}{f} = \frac{(n - n_c)w_p}{f}. \quad (\text{C.8})$$

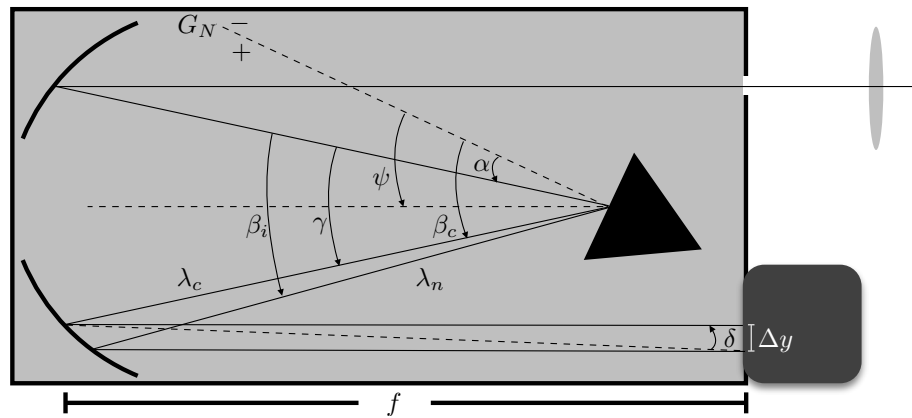


Figure C.4: Geometry of the spectrometer system used to calculate the pixel location of the  $n$ th diffracted beam.

By combining Eqs. (C.1) and (C.8), we can arrive at the wavelength of light that strikes the  $n$ th pixel of the CCD:

$$\begin{aligned}
 \lambda_n &= \frac{d}{m} [\sin \alpha + \sin \beta_n] \\
 &= \frac{d}{m} [\sin \alpha + \sin (\beta_c + \delta)] \\
 &= \frac{d}{m} \left[ \sin \left( \psi - \frac{\gamma}{2} \right) + \sin \left( \psi + \frac{\gamma}{2} + \arctan \left( \frac{(n - n_c)w_p}{f} \right) \right) \right].
 \end{aligned} \tag{C.9}$$

Eq. (C.9) can be used to calculate the linear dispersion  $D$  across the CCD chip. It is usually assumed that the dispersion across the entire CCD is approximately equal to the dispersion at the center pixel of the device, and for the purposes of our calculations we will assume this relationship is valid. Therefore, by taking the derivative of  $\lambda_n$  with respect to  $\Delta y$  and taking into account that  $\Delta y \ll f$ , we arrive at

$$D = \frac{d\lambda_n}{d\Delta y} = \frac{d}{m} \cos \beta_c \frac{f}{f^2 + (\Delta y)^2} = \frac{d}{mf} \cos \beta_c. \tag{C.10}$$

For a triple spectrometer system used in subtractive mode, as shown in Fig. C.5, the first two stages of the spectrometer are used as a high quality bandpass filter. In this case, the dispersion is the same as that of the third stage of the system because the dispersion from the first two stages will always cancel each other out.

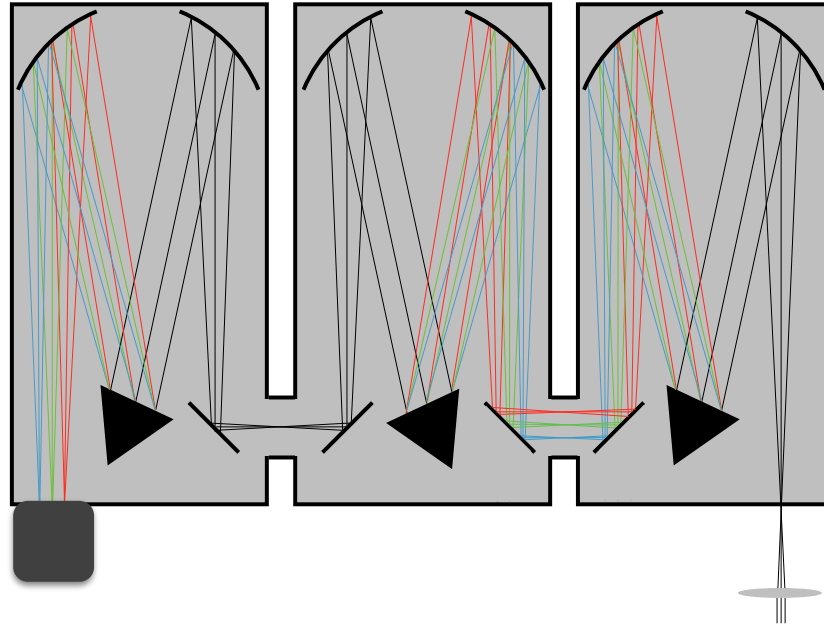


Figure C.5: Triple spectrometer in the subtractive configuration. Note that the first two stages are used as a high quality bandpass filter, with the dispersion canceling out before entering the third stage.

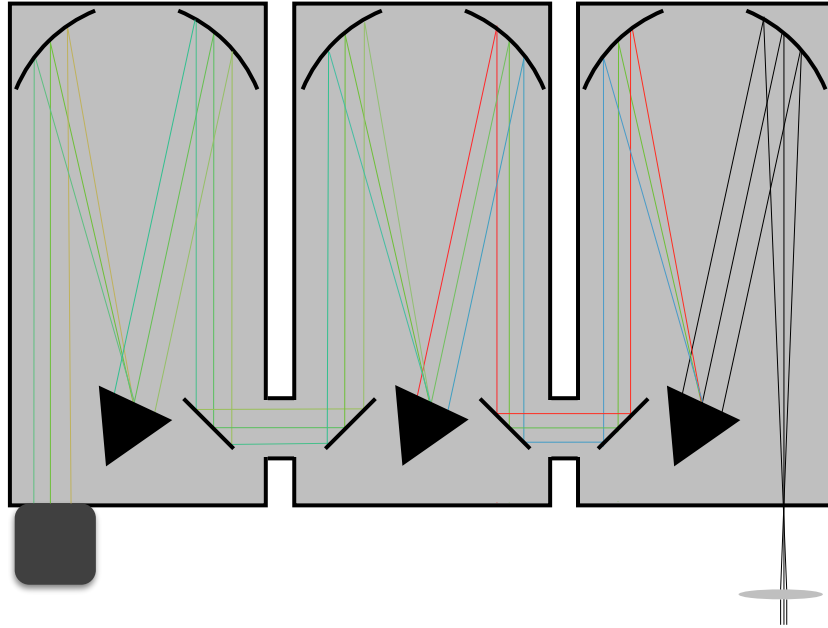


Figure C.6: Triple spectrometer in the additive configuration. The dispersion of the spectrometer in this configuration is roughly reduced by a factor of three.

For a triple spectrometer system used in the triple additive configuration, as shown in Fig. C.6, the final linear dispersion is a non-linear function of focal lengths, grating groove densities, and inclusion angles of all three stages. Typically, the linear dispersion for a triple additive spectrometer system is either found empirically or calculated using special ray-tracing software. There are a few special cases where the linear dispersion for a triple additive system can be approximately calculated. If all three stages have the same focal length and the same diffraction grating groove density, then the linear dispersion can be calculated by using an effective focal length in Eq. (C.10), which becomes the sum of the focal lengths of the individual spectrometers:

$$f_{effective} = f_1 + f_2 + f_3. \quad (C.11)$$

The resolution of the spectrometer system can be calculated by examining the bandpass of the spectrometer on the CCD camera. Fig. C.7 shows the magnification of the entrance slit at the CCD camera.

Using Fig. C.7 the width of the image of the entrance slit projected onto the exit focal plane can be compared to the width of a single pixel of the CCD camera in order to calculate the final bandpass of light to be detected. For a spectrometer whose diffraction grating is equidistant from both the entrance and exit ports, the width of the entrance slit image is calculated to be

$$w' = w \frac{\cos \alpha}{\cos \beta}. \quad (C.12)$$

The final bandpass  $B$  of light is then limited by either the width of the entrance slit image or the CCD pixel width, whichever is larger. The product of the limiting width  $w'$  ( $w_p$ ), and

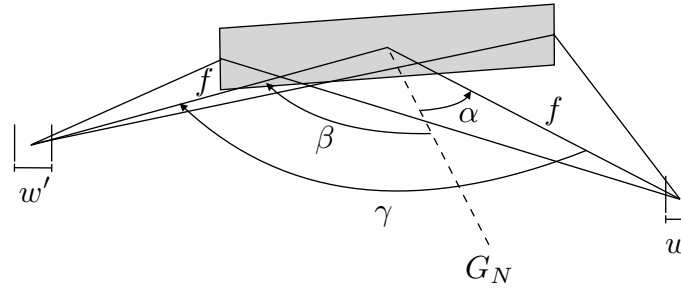


Figure C.7: Schematic showing the width of the image of the entrance slit at the CCD camera. The image is for a spectrometer whose grating is equidistant from the entrance and exit ports.

the linear dispersion  $D$  yield the final bandpass  $B$  ( $B_p$ ):

$$B = w'D = w \frac{\cos \alpha}{\cos \beta_c} \frac{d}{mf} \cos \beta_c = \frac{wd}{mf} \cos \alpha, \quad (\text{C.13})$$

or

$$B_p = w_p D = \frac{w_p d}{mf} \cos \beta_c. \quad (\text{C.14})$$

The pixel bandpass,  $B_p$ , can be viewed as the ultimate spectral resolution of a multi-channel detector, such as a CCD camera.

# Appendix D

## Derivation of Fabry-Perot Equations

In order to study the details of the integration of a Fabry-Perot cavity into our spectroscopic scheme, we use the formalism presented by Born [95] and Guenther [96]. The spectral resolution of the PL can be improved by passing it through a FP cavity. The cavity length sets up a constraint on the wavelengths permitted to transmit through the material. The permitted wavelengths are determined by resonances in the interference pattern resulting from the superposition of multiple reflections off the two constituent surfaces. Consider a FP consisting of two optically flat mirrors of thickness  $T$  spaced a distance  $d$  apart, as in Fig. D.1.

An electromagnetic wave  $E_0$  emanates from a point source in Fig. D.1 and is collimated by the first lens in the system. This collimated wave strikes the first mirror  $M_1$  at an angle  $\alpha$  and a fraction of the wave is reflected  $E'_1$  while the rest is transmitted. We can consider the incident field to follow the equation of a plane wave such that,

$$E(t) = E_0 e^{-i(\omega t - kz)}, \quad (\text{D.1})$$

where  $E_0$  is the amplitude,  $\omega$  is the angular frequency, and  $k = 2\pi n/\lambda$  is the wave vector.

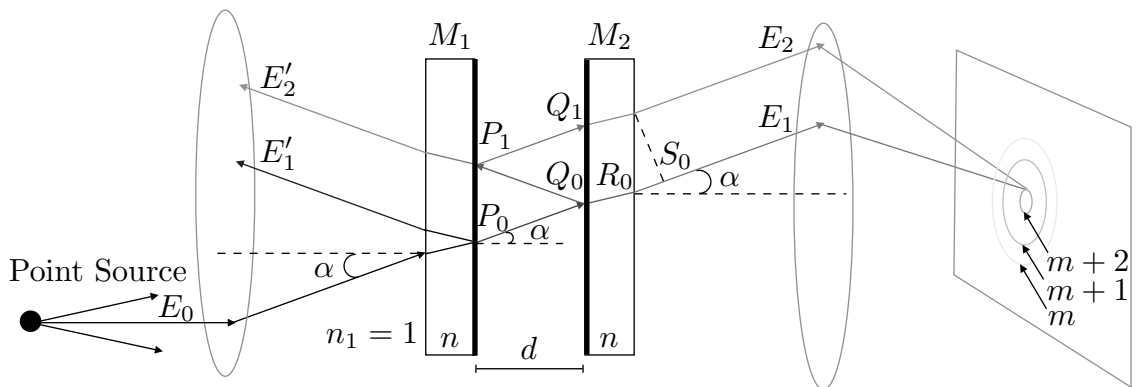


Figure D.1: A FP consists of a pair of highly reflective mirrors spaced micrometers to centimeters apart. The interference pattern shown on the screen is a result of the sum of multiple reflections off the pair of mirrors.

If we set  $z = 0$  at the point  $P_0$ , then we can calculate the path length and phase differences between the first  $E_1$  and second  $E_2$  transmitted waves.

First, let's calculate the path length difference between these waves. The path length difference is

$$\begin{aligned} \overline{Q_0P_1Q_1} - \overline{R_0S_0} &= \frac{2d}{\cos \alpha} - 2d \tan \alpha \sin \alpha \\ &= \frac{2d}{\cos \alpha} (1 - \sin^2 \alpha) \\ &= 2d \cos \alpha. \end{aligned} \quad (\text{D.2})$$

Because  $E_2$  reflects off of two surfaces of a higher index of refraction, points  $Q_0$  and  $P_1$ , the phase difference due to these reflections gives a factor of  $e^{2\pi i} = 1$  and can be ignored. The path length difference, however, leads to a phase difference of

$$\phi = \frac{2\pi}{\lambda} \times 2d \cos \alpha. \quad (\text{D.3})$$

The intensity of the fringes created at the screen can be calculated by first considering the amount of light lost to reflections. We can define the reflection coefficient  $\mathcal{R}$  as the ratio of reflected light to the incident light

$$\mathcal{R} = \frac{I_R}{I_{inc}}. \quad (\text{D.4})$$

We can translate these intensities to electric field amplitudes by remembering that the intensity is the modulus squared of the electric fields, therefore

$$\frac{E_R}{E_{inc}} = -\sqrt{\mathcal{R}}, \quad (\text{D.5})$$

where the negative sign comes from the phase being flipped by  $\pi$  upon reflection off a material of higher index of refraction. With the same treatment we can obtain the fraction of light transmitted, which becomes

$$\frac{E_T}{E_{inc}} = \sqrt{1 - \mathcal{R}}. \quad (\text{D.6})$$

Now we can calculate the transmission of the FP by considering the amount of light lost due to transmission and reflection as well as the phase changes that occur upon propagation. The transmitted wave picks up a factor of  $\sqrt{1 - \mathcal{R}}$  for each of the highly reflective surfaces it crosses. Therefore the transmitted field amplitude of the wave after traveling through both mirrors becomes

$$E_1 = (1 - \mathcal{R})E_0 e^{-i(\omega t - k_1 \overline{P_0Q_0} - 2kT)}. \quad (\text{D.7})$$

The amplitude only picks up two factors of  $\sqrt{1 - \mathcal{R}}$  because the outside surfaces of the FP mirrors are typically coated with antireflection coatings. We can write the constant phase  $k_1 \overline{P_0Q_0} + 2kT = \frac{k_1 d}{\cos \alpha} + 2kT = \phi_0$  and rewrite  $E_1$  as

$$E_1 = (1 - \mathcal{R})E_0 e^{-i(\omega t - \phi_0)}. \quad (\text{D.8})$$



The transmitted field amplitude of  $E_2$  can be written by first noting that the wave reflects off the mirrors two times before exiting the FP. This adds an additional factor of  $\mathcal{R}$  to the field amplitude and the path length contributes an additional phase offset of  $\phi$  such that

$$E_2 = (1 - \mathcal{R})\mathcal{R}E_0e^{-i(\omega t - \phi_0)}e^{-i\phi}. \quad (\text{D.9})$$

We can now extrapolate the transmitted field amplitudes of additional reflections to produce an equation for the field amplitude of the  $N$ th transmitted wave by recognizing that successive waves are modified by a factor of  $\mathcal{R}e^{-i\phi}$ . Therefore,

$$E_N = (1 - \mathcal{R})\mathcal{R}^{N-1}E_0e^{-i(\omega t - \phi_0)}e^{-i(N-1)\phi}. \quad (\text{D.10})$$

The electric field amplitude at the screen will be the sum of all of these transmitted waves. Without loss of generality we can assume that the number of waves tends toward infinity such that

$$E_T = \sum_{N=1}^{\infty} E_N. \quad (\text{D.11})$$

Evaluating this sum becomes trivial once recognizing it as the sum of an infinite geometric series

$$\begin{aligned} E_T &= (1 - \mathcal{R})E_0e^{-i(\omega t - \phi_0)}(1 + \mathcal{R}e^{-i\phi} + \mathcal{R}^2e^{-i2\phi} + \mathcal{R}^3e^{-i3\phi} + \dots) \\ &= \frac{(1 - \mathcal{R})E_0e^{-i(\omega t - \phi_0)}}{1 - \mathcal{R}e^{-i\phi}}. \end{aligned} \quad (\text{D.12})$$

We can now calculate the transmitted intensity  $I_T$  by taking the modulus squared of the transmitted field amplitudes, yielding

$$\begin{aligned} I_T &= \frac{(1 - \mathcal{R})^2 I_0}{1 + \mathcal{R}^2 - \mathcal{R}e^{-i\phi} - \mathcal{R}e^{i\phi}} \\ &= \frac{(1 - \mathcal{R})^2 I_0}{1 + \mathcal{R}^2 - 2\mathcal{R} \cos \phi} \\ &= \frac{(1 - \mathcal{R})^2 I_0}{(1 - \mathcal{R})^2 + 4\mathcal{R} \sin^2 \frac{\phi}{2}}. \end{aligned} \quad (\text{D.13})$$

Introducing the coefficient of finesse  $F$  allows us to simplify this equation to

$$I_T = \frac{I_0}{1 + F \sin^2 \frac{\phi}{2}}, \quad (\text{D.14})$$

where

$$F = \frac{4\mathcal{R}}{(1 - \mathcal{R})^2}. \quad (\text{D.15})$$

From the above two equations we can see that the intensity spectrum will have sharper lines as the coefficient of finesse increases, which in turn becomes larger due to surfaces of higher reflectance. These results are summarized in Fig. D.2.

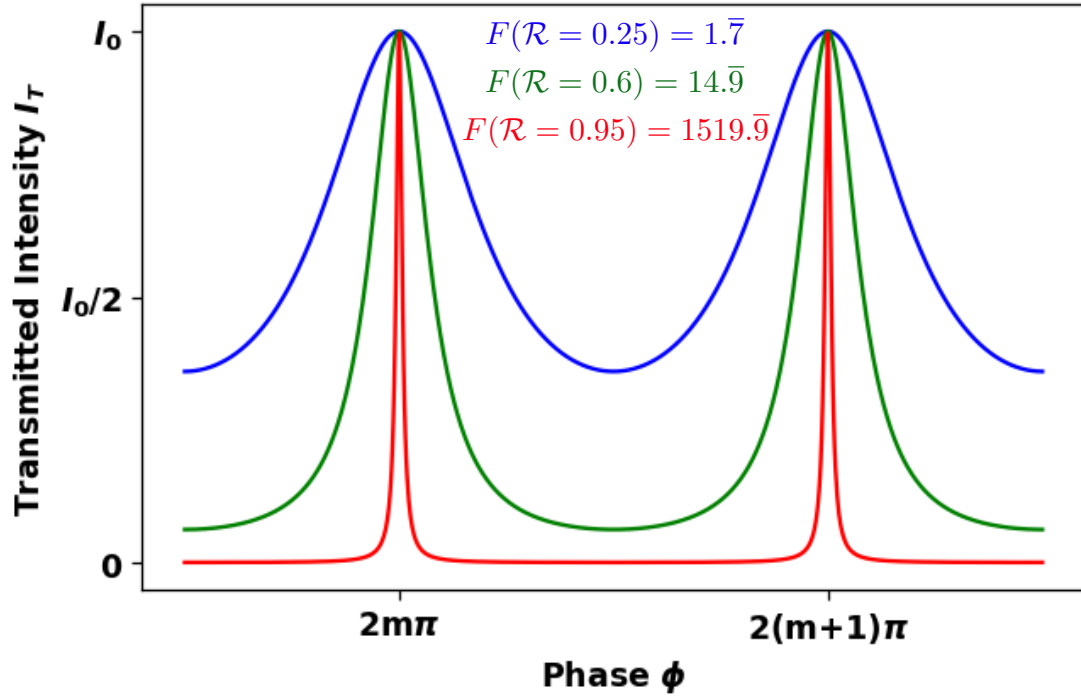


Figure D.2: Transmission intensity of a FP as a function of phase. The different colors represent varying values of the coefficient of finesse due to mirrors of different reflectivities.

We can determine where the intensity will be maximum and minimum by finding when  $\sin^2 \frac{\phi}{2}$  is equal to zero and one, respectively:

$$I_{T,max} = I_0, \quad \text{when } \phi = 2m\pi, \quad (\text{D.16})$$

and

$$I_{T,min} = \frac{I_0}{1 + F}, \quad \text{when } \phi = (2m + 1)\pi, \quad (\text{D.17})$$

where  $m$  is an integer. When the coefficient of finesse is very large, the FP acts as a high quality bandpass filter, only allowing light to transmit if it enables Eq. (D.3) to be equal to an integer multiple of  $2\pi$ .

To understand how well the FP acts as a bandpass filter, we will introduce the concept of finesse, which is defined as the number of resolvable peaks that can fit into the phase separation  $2\pi$ , which is also known as the free spectral range,

$$\mathcal{F} = \frac{2\pi}{\phi_w}. \quad (\text{D.18})$$

Here,  $\phi_w$  is the full width at half maximum of the transmission peak in phase space and can be found by setting Eq. (D.14) equal to  $I_0/2$  and solving for  $\phi_w$ :

$$\frac{1}{2}I_0 = \frac{I_0}{1 + F \sin^2 \frac{\phi_w}{4}}. \quad (\text{D.19})$$

It is easy to see that this equation will hold true only if

$$F \sin^2 \frac{\phi_w}{4} = 1. \quad (\text{D.20})$$

The small angle approximation can be used here because at high coefficients of finesse  $F$  the spectral width of the FP  $\phi_w$  will be very small compared to the free spectral range  $2\pi$ , and the transmission peak half maxima will be located at  $\phi = 2m\pi \pm \phi_w/2$ :

$$\phi_w = \frac{4}{\sqrt{F}}. \quad (\text{D.21})$$

From the definition of finesse  $\mathcal{F}$  we can see that

$$\mathcal{F} = \frac{2\pi\sqrt{F}}{4} = \frac{\pi\sqrt{F}}{2}. \quad (\text{D.22})$$

To see how well the FP acts as a high quality spectrum analyzer we can observe the shift in the transmission peak as a function of the mirror spacing, which will be set to an initial value of 1.5mm. Assuming the light source is a diode laser of wavelength 960nm, and incident normal to the FP ( $\alpha = 0$ ), the phase difference will be

$$\phi = \frac{4d\pi}{\lambda} = 6,250\pi = 2m\pi, \quad \text{where } m = 3,125. \quad (\text{D.23})$$

The transmission intensity will be at a maximum with these parameters. Subsequent maxima will occur at wavelengths of

$$\lambda = \frac{2d}{m}. \quad (\text{D.24})$$

From this equation we can see that a change in the spacing between the mirrors  $d$  that is proportional to a change in the mode number by one will result in the same wavelength having another transmission maximum through the FP. In a similar fashion, the mode number can be held constant and the same change in mirror spacing will correspond to a slightly different wavelength.

Knowing this, we can rearrange the above equation so that the mode number is on one side, take the derivative with respect to wavelength, and set the change in mode number to negative one to find the wavelength spacing between transition maxima.

$$\Delta m = -1 = -\frac{2d}{\lambda^2} \Delta \lambda, \quad \text{therefore } \Delta \lambda = \frac{\lambda^2}{2d}. \quad (\text{D.25})$$

This wavelength spacing is known as the free spectral range of the cavity and is related to the free spectral range we calculated earlier in phase space. With this in mind, the finesse of the FP cavity can be calculated by taking the wavelength spacing and dividing it by the width of the transmission peak, similar to the way it was calculated in phase space.

$$\mathcal{F} = \frac{\Delta \lambda}{\lambda_w}. \quad (\text{D.26})$$

The above equation shows that the FP will have a FWHM resolution  $\lambda_w$  equal to the free spectral range divided by the finesse.

# Bibliography

- [1] Tijana Rajh, Olga I. Micic, and Arthur J. Nozik. Synthesis and Characterization of Surface-Modified Colloidal CdTe Quantum Dots. *Journal of Physical Chemistry*, 97:11999–12003, 1993.
- [2] S. Fafard, R. Leon, D. Leonard, J. L. Merz, and P. M. Petroff. Visible photoluminescence from N-dot ensembles and the linewidth of ultrasmall  $\text{Al}_y\text{In}_{1-y}\text{As}/\text{Al}_x\text{Ga}_{1-x}\text{As}$  quantum dots. *Physical Review B*, 50(11):8086, Sep 1994.
- [3] Kohki Mukai, Nobuyuki Ohtsuka, and Mitsuru Sugawara. High photoluminescence efficiency of InGaAs/GaAs quantum dots self-formed by atomic layer epitaxy technique. *Applied Physics Letters*, 70(18):2416–2418, 1997.
- [4] Landin, L. and Miller, M. S. and Pistol, M. E. and Pryor, C. E. and Samuelson. Optical Studies of Individual InAs Quantum Dots in GaAs: Few-Particle Effects. *Science*, 280(5361):262–264, 1998.
- [5] M-E Pistol, P Castrillo, D Hessman, J A Prieto, and L Samuelson. Random telegraph noise in photoluminescence from individual self-assembled quantum dots. *Physical Review B*, 59(16):10725–10729, 1999.
- [6] D. Gammon, E. S. Snow, B. V. Shanabrook, D. S. Katzer, and D. Park. Fine Structure Splitting in the Optical Spectra of Single GaAs Quantum Dots. *Physical Review Letters*, pages 3005–3008, 1996.
- [7] Alexander Högele, Stefan Seidl, Martin Kroner, Khaled Karrai, Richard J. Warburton, Brian D. Gerardot, and Pierre M. Petroff. Voltage-controlled optics of a quantum dot. *Physical Review Letters*, 93(21):19–22, 2004.
- [8] A. Muller, E. B. Flagg, P. Bianucci, X. Y. Wang, D. G. Deppe, W. Ma, J. Zhang, G. J. Salamo, M. Xiao, and C. K. Shih. Resonance fluorescence from a coherently driven semiconductor quantum dot in a cavity. *Physical Review Letters*, 99(18):2–5, 2007.
- [9] M. Atature. Quantum-Dot Spin-State Preparation with Near-Unity Fidelity. *Science*, 312(5773):551–553, apr 2006.
- [10] D. D. Awschalom, L. C. Bassett, A. S. Dzurak, E. L. Hu, and J. R. Petta. Quantum Spintronics: Engineering and Manipulating Atom-Like Spins in Semiconductors. *Science*, 339(6124):1174–1179, mar 2013.

- [11] Gediminas Juska, Valeria Dimastrodonato, Lorenzo O. Mereni, Agnieszka Gocalinska, and Emanuele Pelucchi. Towards quantum-dot arrays of entangled photon emitters. *Nature Photonics*, 7(7):527–531, 2013.
- [12] C. L. Degen, F. Reinhard, and P. Cappellaro. Quantum sensing. *Reviews of Modern Physics*, 89(3):1–39, 2017.
- [13] Samuel G. Carter, Allan S. Bracker, Kim Mijin, Chul Soo Kim, Maxim Zalalutdinov, Brennan C. Pursley, Sophia E. Economou, Cyprian Czarnocki, Joshua Casara, Michael Scheibner, and Dan Gammon. Quantum sensing of mechanical motion with a single inas quantum dot. *GOMACTech Proceedings*, 2017.
- [14] M. D. Lahaye, J. Suh, P. M. Echternach, K. C. Schwab, and M. L. Roukes. Nanomechanical measurements of a superconducting qubit. *Nature*, 459(7249):960–965, 2009.
- [15] Steven D. Bennett, Lynda Cockins, Yoichi Miyahara, Peter Grütter, and Aashish A. Clerk. Strong electromechanical coupling of an atomic force microscope cantilever to a quantum dot. *Physical Review Letters*, 104(1):2–5, 2010.
- [16] I. Yeo, P-L. de Assis, A. Gloppe, E. Dupont-Ferrier, P. Verlot, N. S. Malik, E. Dupuy, J. Claudon, J-M. Gérard, A. Auffèves, and et al. Strain-mediated coupling in a quantum dot–mechanical oscillator hybrid system. *Nature Nanotechnology*, 9(2):106–110, Dec 2013.
- [17] Markus Aspelmeyer, Tobias J. Kippenberg, and Florian Marquardt. Cavity optomechanics. *Reviews of Modern Physics*, 86(4):1391–1452, 2014.
- [18] Patrick M. Vora, Allan S. Bracker, Samuel G. Carter, Timothy M. Sweeney, Mijin Kim, Chul Soo Kim, Lily Yang, Peter G. Brereton, Sophia E. Economou, and Daniel Gammon. Spin–cavity interactions between a quantum dot molecule and a photonic crystal cavity. *Nature Communications*, 6(May):7665, 2015.
- [19] Arka Majumdar, Michal Bajcsy, Armand Rundquist, Erik Kim, and Jelena Vučković. Phonon-mediated coupling between quantum dots through an off-resonant microcavity. *Physical Review B*, 85(19):1–6, 2012.
- [20] S. G. Carter, A. S. Bracker, M. K. Yakes, M. K. Zalalutdinov, M. Kim, C. S. Kim, C. Czarnocki, Michael Scheibner, and D. Gammon. Sensing flexural motion of a photonic crystal membrane with InGaAs quantum dots. *Applied Physics Letters*, 111(18), 2017.
- [21] Aymeric Delteil, Zhe Sun, Wei-bo Gao, Emre Togan, Stefan Faelt, and Ataç Imamoglu. Generation of heralded entanglement between distant hole spins. *Nature Physics*, 12(December):218, 2015.

- [22] F. Hargart, M. Müller, K. Roy-Choudhury, S. L. Portalupi, C. Schneider, S. Höfling, M. Kamp, S. Hughes, and P. Michler. Cavity-enhanced simultaneous dressing of quantum dot exciton and biexciton states. *Physical Review B*, 93(11):1–9, 2016.
- [23] Catherine Tonin, Richard Hostein, Valia Voliotis, Roger Grousson, Aristide Lemaitre, and Anthony Martinez. Polarization properties of excitonic qubits in single self-assembled quantum dots. *Physical Review B*, 85(15):1–9, 2012.
- [24] P. E. Kremer, A. C. Dada, P. Kumar, Y. Ma, S. Kumar, E. Clarke, and B. D. Gerardot. Strain-tunable quantum dot embedded in a nanowire antenna. *Physical Review B*, 90(20):1–6, 2014.
- [25] Xing Ding, Yu He, Z. C. Duan, Niels Gregersen, M. C. Chen, S. Unsleber, S. Maier, Christian Schneider, Martin Kamp, Sven Höfling, Chao Yang Lu, and Jian Wei Pan. On-Demand Single Photons with High Extraction Efficiency and Near-Unity Indistinguishability from a Resonantly Driven Quantum Dot in a Micropillar. *Physical Review Letters*, 116(2):1–6, 2016.
- [26] S. G. Carter, A. S. Bracker, G. W. Bryant, M. Kim, C. S. Kim, M. K. Zalalutdinov, M. K. Yakes, C. Czarnocki, J. Casara, M. Scheibner, and D. Gammon. Spin-mechanical coupling of an inas quantum dot embedded in a mechanical resonator.
- [27] Charles Kittel. *Introduction to Solid State Physics*. John Wiley & Sons, Inc., New York, 7th edition, 1996.
- [28] P. Lawaetz. Valence-band parameters in cubic semiconductors. *Physical Review B*, 4(10):3460–3467, 1971.
- [29] U. Kreibig and M. Vollmer. *Spin Physics in Semiconductors*, volume 157. Springer, 2008.
- [30] C. R. Pidgeon, S. H. Groves, and J. Feinleib. Electroreflectance study of interband magneto-optical transitions in InAs and InSb at 1.5 ° K. *Solid State Communications*, 5(8):677–680, 1967.
- [31] C. R. Pidgeon, D. L. Mitchell, and R. N. Brown. Interband magnetoabsorption in InAs and InSb. *Physical Review*, 154(3):737–742, 1967.
- [32] Calvin Yi-ping Chao and Shun Lien Chuang. *Spin-Orbit-Coupling Effects on the Valence -Band Structure of Strained Semiconductor Quantum Wells*, 1992.
- [33] I. Vurgaftman, J. R. Meyer, and L. R. Ram-Mohan. Band parameters for III-V compound semiconductors and their alloys. *Journal of Applied Physics*, 89(11 I):5815–5875, 2001.
- [34] Jonathan H. Prechtel. *The hole spin in a semiconductor quantum dot*. PhD thesis, Universität Basel, 2015.

- [35] Swati Ramanathan, Greg Petersen, Kushal C. Wijesundara, Ramana Thota, Eric A. Stinaff, Mark L. Kerfoot, Michael Scheibner, Allan S. Bracker, and Daniel Gammon. Quantum-confined Stark effects in coupled InAs/GaAs quantum dots. *Applied Physics Letters*, 102(21), 2013.
- [36] J. Seufert, M. Obert, M. Scheibner, N. A. Gippius, G. Bacher, A. Forchel, T. Passow, K. Leonardi, and D. Hommel. Stark effect and polarizability in a single CdSe/ZnSe quantum dot. *Applied Physics Letters*, 79(7):1033–1035, 2001.
- [37] Y.P. Varshni. Temperature dependence of the energy gap in semiconductors. *Physica*, 34(1):149–154, 1967.
- [38] Z. M. Fang, K. Y. Ma, R. M. Cohen, and G. B. Stringfellow. Photoluminescence of InAsBi and InAsSbBi grown by organometallic vapor phase epitaxy. *Journal of Applied Physics*, 68(3):1187–1191, 1990.
- [39] M. Levinshtein, S. Rumyantsev, and M. Shur. *Handbook Series on Semiconductor Parameters*, volume 1: Si, Ge, C (Diamond), GaAs, GaP, GaSb, InAs, InP, InSb. World Scientific, 1996.
- [40] Juha Tommila, Christian Strelow, Andreas Schramm, Teemu V Hakkarainen, Mihail Dumitrescu, Tobias Kipp, and Mircea Guina. The influence of temperature on the photoluminescence properties of single InAs quantum dots grown on patterned GaAs. *Nanoscale Research Letters*, 7(1):313, 2012.
- [41] M. Paillard, X. Marie, E. Vanelle, T. Amand, and V. K. Kalevich. Time-resolved photoluminescence in self-assembled InAs / GaAs quantum dots under strictly resonant excitation Time-resolved photoluminescence in self-assembled InAs / GaAs. *Applied Physics Letters*, 76(1):76–78 (3 pages), 2000.
- [42] Brian D. Gerardot, Daniel Brunner, Paul A. Dalgarno, Patrik Öhberg, Stefan Seidl, Martin Kroner, Khaled Karrai, Nick G. Stoltz, Pierre M. Petroff, and Richard J. Warburton. Optical pumping of a single hole spin in a quantum dot. *Nature*, 451(7177):441–444, 2008.
- [43] Ilya V. Ponomarev, Michael Scheibner, Eric A. Stinaff, Allan S. Bracker, M. F. Doty, S. C. Badescu, M. E. Ware, V. L. Korenev, T. L. Reinecke, and Daniel Gammon. Theory of spin states in coupled quantum dots. *Physica Status Solidi (B)*, 243(15):3869–3873, 2006.
- [44] Michael Scheibner, Allan S. Bracker, Danny Kim, and Daniel Gammon. Essential concepts in the optical properties of quantum dot molecules. *Solid State Communications*, 149(35-36):1427–1435, 2009.
- [45] Michael Scheibner, M. Yakes, Allan S. Bracker, Ilya V. Ponomarev, M. F. Doty, C. S. Hellberg, L. J. Whitman, T. L. Reinecke, and Daniel Gammon. Optically mapping the electronic structure of coupled quantum dots. *Nature Physics*, 4(4):291–295, 2008.

- [46] Denis V. Bulaev and Daniel Loss. Spin relaxation and decoherence of holes in quantum dots. *Physical Review Letters*, 95(7):1–4, 2005.
- [47] P. Borri, W. Langbein, U. Woggon, V. Stavarache, D. Reuter, and A. D. Wieck. Exciton dephasing via phonon interactions in InAs quantum dots: Dependence on quantum confinement. *Physical Review B - Condensed Matter and Materials Physics*, 71(11):1–8, 2005.
- [48] James Camparo. The rubidium atomic clock and basic research. *Physics Today*, 60(11):33–39, 2007.
- [49] N. W. Ashcroft. *Solid State Physics*. Holt Rinehart and Winston, 1976.
- [50] Alexander Altland and Ben D. Simons. *Condensed Matter Field Theory*. Leiden: Cambridge University Press, 2nd edition, 2010.
- [51] JT Devreese. *Moles agitat mentem: developments in the physics of the solid*. Technische Hogeschool Eindhoven, 1979.
- [52] Mark L. Kerfoot, A. O. Govorov, C. Czarnocki, D. Lu, Y. N. Gad, Allan S. Bracker, Daniel Gammon, and Michael Scheibner. Optophonics with coupled quantum dots. *Nature Communications*, 5:3299, 2014.
- [53] J. M. Moison, F. Houzay, F. Barthe, L. Leprince, E. André, and O. Vatel. Self-organized growth of regular nanometer-scale InAs dots on GaAs. *Applied Physics Letters*, 64(2):196–198, 1994.
- [54] Allan S. Bracker, Michael Scheibner, M. F. Doty, Eric A. Stinaff, Ilya V. Ponomarev, J. C. Kim, L. J. Whitman, T. L. Reinecke, and Daniel Gammon. Engineering electron and hole tunneling with asymmetric InAs quantum dot molecules. *Applied Physics Letters*, 89(23):2–4, 2006.
- [55] Michael Scheibner, M. F. Doty, Ilya V. Ponomarev, Allan S. Bracker, Eric A. Stinaff, V. L. Korenev, T. L. Reinecke, and Daniel Gammon. Spin fine structure of optically excited quantum dot molecules. *Physical Review B*, 75(24):1–9, 2007.
- [56] E. M. Purcell, H.C. Torrey, and R. V. Pound. Resonance Absorption by Nuclear Magnetic Moments in a Solid. *Physical Review*, 69:37, 1946.
- [57] Wolfgang Demtröder. *Laser spectroscopy*, volume 1. Springer, 2013.
- [58] Mark A. Roseman. *Low Temperature Magnetic Force Microscopy Studies of Superconducting Niobium Films*. PhD thesis, McGill University, 2001.
- [59] Romain-Pierre. Stomp. *Dissipative and electrostatic force spectroscopy of InAs quantum dots by non-contact atomic force microscopy*. PhD thesis, McGill University, 2005.



- [60] Lynda Patricia Cockins. *Atomic force microscopy studies on the electrostatic environment and energy levels of self-assembled quantum dots*. PhD thesis, McGill University, 2010.
- [61] Valerio Pini, Bruno Tiribilli, Cecilia Maria Cristina Gambi, and Massimo Vassalli. Dynamical characterization of vibrating AFM cantilevers forced by photothermal excitation. *Physical Review B - Condensed Matter and Materials Physics*, 81(5):2–6, 2010.
- [62] Benjamin Andreas Bircher, Hans Peter Lang, Luc Duempelmann, Christoph Gerber, and Thomas Braun. Photothermal excitation of microcantilevers in liquid: effect of the excitation laser position on temperature and vibrational amplitude. *Micro & Nano Letters*, 8(11):770–774, 2013.
- [63] Michael Wahl. Time-correlated single photon counting, 2014.
- [64] Boston Electronics Corporation. What is time correlated single photon counting?, August 2016.
- [65] Cyprian Czarnocki, Mark L. Kerfoot, Joshua Casara, Andrew R. Jacobs, Cameron Jennings, and Michael Scheibner. High Resolution Phonon-assisted Quasi-resonance Fluorescence Spectroscopy. *Journal of Visualized Experiments*, 1(112):1–10, 2016.
- [66] K. P. O. Donnell and X. Chen. Temperature dependence of semiconductor band gaps Temperature dependence of semiconductor band gaps. *Applied Physics Letters*, 2924(1991):1–4, 2011.
- [67] Eric A. Stinaff, Swati Ramanathan, Kushal C. Wijesundara, Mauricio Garrido, Michael Scheibner, Allan S. Bracker, and Daniel Gammon. Polarization dependent photoluminescence of charged quantum dot molecules. *Physica Status Solidi*, 5(7):2464–2468, 2008.
- [68] Michael Scheibner, Sophia E. Economou, Ilya V. Ponomarev, Cameron Jennings, Allan S. Bracker, and Daniel Gammon. Two-photon absorption by a quantum dot pair. *Physical Review B - Condensed Matter and Materials Physics*, 92(8):1–5, 2015.
- [69] Patrick M. Vora, Allan S. Bracker, Samuel G. Carter, Timothy M. Sweeney, Mijin Kim, Chul Soo Kim, Lily Yang, Peter G. Brereton, Sophia E. Economou, and Daniel Gammon. Spin-cavity interactions between a quantum dot molecule and a photonic crystal cavity. *Nature Communications*, 6(May):1–9, 2015.
- [70] Samuel G. Carter, Timothy M. Sweeney, Mijin Kim, Chul Soo Kim, Dmitry Solenov, Sophia E. Economou, Thomas L. Reinecke, Lily Yang, Allan S. Bracker, and Daniel Gammon. Quantum control of a spin qubit coupled to a photonic crystal cavity. *Nature Photonics*, 7(4):329–334, 2013.

- [71] Timothy M. Sweeney, Samuel G. Carter, Allan S. Bracker, Mijin Kim, Chul Soo Kim, Lily Yang, Patrick M. Vora, Peter G. Brereton, Erin R. Cleveland, and Daniel Gammon. Cavity-stimulated Raman emission from a single quantum dot spin. *Nature Photonics*, 8(6):442–447, 2014.
- [72] R. Beardmore. Loaded flat plates, <http://www.roymech.co.uk/>, February 2013.
- [73] S. M. Sze. *Semiconductor Sensors*, chapter Appendix D, page 535. John Wiley & Sons, Inc., 1994.
- [74] L. Novotny and B. Hect. *Principles of Nano-Optics*. Cambridge University Press, 2012.
- [75] Kristiaan De Greve, Peter L. McMahon, David Press, Thaddeus D. Ladd, Dirk Bisping, Christian Schneider, Martin Kamp, Lukas Worschech, Sven Höfling, Alfred Forchel, and Yoshihisa Yamamoto. Ultrafast coherent control and suppressed nuclear feedback of a single quantum dot hole qubit. *Nature Physics*, 7(11):872–878, 2011.
- [76] S. G. Carter, Sophia E. Economou, A. Greilich, Edwin Barnes, T. Sweeney, A. S. Bracker, and D. Gammon. Strong hyperfine-induced modulation of an optically driven hole spin in an InAs quantum dot. *Physical Review B - Condensed Matter and Materials Physics*, 89(7):1–9, 2014.
- [77] Jonathan H. Prechtel, Andreas V. Kuhlmann, Julien Houel, Arne Ludwig, Sascha R. Valentin, Andreas D. Wieck, and Richard J. Warburton. Decoupling a hole spin qubit from the nuclear spins. *Nature Materials*, 15(9):981–986, 2016.
- [78] Yu He, Yu-Ming He, Y. J. Wei, X. Jiang, M. C. Chen, F. L. Xiong, Y. Zhao, Christian Schneider, Martin Kamp, Sven Höfling, Chao Yang Lu, and Jian Wei Pan. Indistinguishable tunable single photons emitted by spin-flip Raman transitions in InGaAs quantum dots. *Physical Review Letters*, 111(23):1–5, 2013.
- [79] G. Fernandez, T. Volz, R. Desbuquois, A. Badolato, and A. Imamoglu. Optically tunable spontaneous Raman fluorescence from a single self-assembled InGaAs quantum dot. *Physical Review Letters*, 103(8):1–4, 2009.
- [80] Alex Greilich, Samuel G. Carter, Danny Kim, Allan S. Bracker, and Daniel Gammon. Optical control of one and two hole spins in interacting quantum dots. *Nature Photonics*, 5(11):702–708, 2011.
- [81] Danny Kim, Samuel G. Carter, Alex Greilich, Allan S. Bracker, and Daniel Gammon. Ultrafast optical control of entanglement between two quantum-dot spins. *Nature Physics*, 7(3):223–229, Dec 2010.
- [82] Kristiaan De Greve, Leo Yu, Peter L. McMahon, Jason S. Pelc, Chandra M. Natarajan, Na Young Kim, Eisuke Abe, Sebastian Maier, Christian Schneider, Martin Kamp, and et al. Quantum-dot spin–photon entanglement via frequency downconversion to telecom wavelength. *Nature*, 491(7424):421–425, Nov 2012.

- [83] Donghun Lee, Kenneth W. Lee, Jeffrey V. Cady, Preeti Ovarthaiyapong, and Ania C. Bleszynski Jayich. Topical review: Spins and mechanics in diamond. *Journal of Optics (United Kingdom)*, 19(3), 2017.
- [84] Shimon Kolkowitz, Ania C Bleszynski Jayich, Quirin P Unterreithmeier, Steven D Bennett, Peter Rabl, J G E Harris, and Mikhail D Lukin. Coherent Sensing of a Mechanical Resonator with a Single-Spin Qubit. *Science*, 510(March):1603–1607, 2012.
- [85] Sungkun Hong, Michael S. Grinolds, Patrick Maletinsky, Ronald L. Walsworth, Mikhail D. Lukin, and Amir Yacoby. Coherent, mechanical control of a single electronic spin. *Nano Letters*, 2012.
- [86] Preeti Ovarthaiyapong, Kenneth W. Lee, Bryan A. Myers, and Ania C Bleszynski Jayich. Dynamic strain-mediated coupling of a single diamond spin to a mechanical resonator. *Nature Communications*, 5:6–11, 2014.
- [87] Adapted by permission from Springer Nature: O. A. Bauchau and J.I. Craig. Euler-Bernoulli beam theory. In *Structural Analysis: With Applications to Aerospace Structures*, pages 173–221. Springer, Netherlands, Dordrecht, 2009.
- [88] Bert Voigtländer. Harmonic oscillator. In *Scanning Probe Microscopy: Atomic Force Microscopy and Scanning Tunneling Microscopy*, pages 15–29. Springer, Berlin, Heidelberg, 2015.
- [89] Adapted by permission from Springer Nature: Bert Voigtländer. Technical Aspects of Atomic Force Microscopy (AFM). In *Scanning Probe Microscopy: Atomic Force Microscopy and Scanning Tunneling Microscopy*, pages 157–175. Springer, Berlin, Heidelberg, 2015.
- [90] Jeffrey L. Hutter and John Bechhoefer. Calibration of atomic-force microscope tips. *Review of Scientific Instruments*, 64(7):1868–1873, 1993.
- [91] J. E. Sader, I. Larson, P. Mulvaney, and L. R. White. Method for the Calibration of Atomic-Force Microscope Cantilevers. *Review of Scientific Instruments*, 66(7):3789–3798, 1995.
- [92] John D Parkin and Georg Hähner. Calibration of the torsional and lateral spring constants of cantilever sensors. *Nanotechnology*, 25(22):225701, 2014.
- [93] John E. Sader, James W.M. Chon, and Paul Mulvaney. Calibration of rectangular atomic force microscope cantilevers. *Review of Scientific Instruments*, 70(10):3967–3969, 1999.
- [94] Princeton Instruments. *TriVista System: User Manual*, 1.b edition, August 2007.
- [95] Max Born and Emil Wolf. The fabry-perot interferometer. In *Principles of optics: Electromagnetic Theory of Propagation, Interference and Diffraction of Light*, pages 366 – 369. Cambridge University Press, 7th edition, 1983.

- [96] Robert D. Guenther. Fabry-perot interferometer. In *Modern Optics*, pages 111–114. John Wiley & Sons, Inc., 1990.